

Modelling and Simulation in Engineering

Modeling and Simulation of Mobile Radio Channels

Guest Editors: Matthias Pätzold, Neji Youssef,
and Carlos A. Gutierrez





Modeling and Simulation of Mobile Radio Channels

Modelling and Simulation in Engineering

Modeling and Simulation of Mobile Radio Channels

Guest Editors: Matthias Pätzold, Neji Youssef,
and Carlos A. Gutierrez



Copyright © 2012 Hindawi Publishing Corporation. All rights reserved.

This is a special issue published in "Modelling and Simulation in Engineering." All articles are open access articles distributed under the Creative Commons Attribution License, which permits unrestricted use, distribution, and reproduction in any medium, provided the original work is properly cited.

Editorial Board

Driss Aboutajdine, Morocco
K. Al-Begain, UK
Adel M. Alimi, Tunisia
Zeki Ayag, Turkey
Sergio Baragetti, Italy
Andrzej Bargiela, UK
Joaquim Barros, Portugal
Salim Belouettar, Luxembourg
Jean-Michel Bergheau, France
Tianshu Bi, China
Philippe Boisse, France
Agostino Bruzzone, Italy
Hing Kai Chan, UK
Jinn Kuen Chen, USA
Min-Chie Chiu, Taiwan
Weizhong Dai, USA
Mingcong Deng, Japan
Lei Ding, China
Tadashi Dohi, Japan
Dimitris Drikakis, UK
Andrzej Dzielinski, Poland
Abdelali El Aroudi, Spain
Enmin Feng, China
Huijun Gao, China
F. Gao, UK
Xiaosheng Gao, USA

Huijun Gao, China
Dariusz J. Gawin, Poland
Ratan K. Guha, USA
Chung-Souk Han, USA
Shinsuke Hara, Japan
Joanna Hartley, UK
Tasawar Hayat, Pakistan
Jing-song Hong, China
Qinglei Hu, China
Bassam A. Izzuddin, UK
MuDer Jeng, Taiwan
Chia-Feng Juang, Taiwan
Iisakki Kosonen, Finland
Stavros Kotsopoulos, Greece
Nikos D. Lagaros, Greece
Hak-Keung Lam, UK
Hongyi Li, China
Dimitrios E. Manolakos, Greece
Shengwei Mei, China
Laurent Mevel, France
Azah Mohamed, Malaysia
Carlos A. Mota Soares, Portugal
Antonio Munjiza, UK
Javier Murillo, Spain
Petr Musilek, Canada
Tomoharu Nakashima, Japan

Gaby Neumann, Germany
Alessandra Orsoni, UK
Javier Otamendi, Spain
Anna Pandolfi, Italy
Bei Peng, China
Ricardo Perera, Spain
Evtim Peytchev, UK
Zhiping Qiu, China
Luis Carlos Rabelo, USA
Ahmed Rachid, France
Franco Ramírez, Spain
Rubens Sampaio, Brazil
Aiguo Song, China
Rajan Srinivasan, India
S. Taib, Malaysia
Mohamed B. Trabia, USA
Joseph Virgone, France
Bauke Vries, The Netherlands
Guowei Wei, USA
Ligang Wu, China
Feng Xiao, China
Farouk Yalaoui, France
Shigeru Yamada, Japan
Guang-Hong Yang, China
ShengKai Yu, Singapore
Qingling Zhang, China

Contents

Modeling and Simulation of Mobile Radio Channels, Matthias Pätzold, Neji Youssef,
and Carlos A. Gutierrez
Volume 2012, Article ID 160297, 2 pages

Design of Wideband MIMO Car-to-Car Channel Models Based on the Geometrical Street Scattering Model, Nurilla Avazov and Matthias Pätzold
Volume 2012, Article ID 264213, 11 pages

A Three-Dimensional Geometry-Based Statistical Model of 2×2 Dual-Polarized MIMO Mobile-to-Mobile Wideband Channels, Jun Chen and Thomas G. Pratt
Volume 2012, Article ID 756508, 16 pages

An Accurate Hardware Sum-of-Cisoids Fading Channel Simulator for Isotropic and Non-Isotropic Mobile Radio Environments, L. Vela-Garcia, J. Vázquez Castillo, R. Parra-Michel, and Matthias Pätzold
Volume 2012, Article ID 542198, 12 pages

Filter-Based Fading Channel Modeling, Amirhossein Alimohammad, Saeed Fouladi Fard,
and Bruce F. Cockburn
Volume 2012, Article ID 705078, 10 pages

Wideband and Ultrawideband Channel Models in Working Machine Environment,
Attaphongse Taparugssanagorn, Matti Hämäläinen, and Jari Iinatti
Volume 2012, Article ID 702917, 10 pages

Editorial

Modeling and Simulation of Mobile Radio Channels

Matthias Pätzold,¹ Neji Youssef,² and Carlos A. Gutierrez³

¹ Department of Information and Communication Technology, University of Agder, 4604 Kristiansand, Norway

² Département EPP (Electronique, Physique et Propagation), Ecole Supérieure des Communications de Tunis, 2083 Ghazala, Tunisia

³ Faculty of Science, Universidad Autonoma de San Luis Potosi, 78290 San Luis Potosi, SLP, Mexico

Correspondence should be addressed to Matthias Pätzold, matthias.paetzold@uia.no

Received 2 December 2012; Accepted 2 December 2012

Copyright © 2012 Matthias Pätzold et al. This is an open access article distributed under the Creative Commons Attribution License, which permits unrestricted use, distribution, and reproduction in any medium, provided the original work is properly cited.

The aggregate demand for multimedia services, high mobility, and global connectivity has resulted in recent years in an explosion of new technologies for wireless communication systems. All components of a wireless communication system ranging from digital modulation schemes over channel coding techniques up to higher layer protocols are more or less influenced by the characteristics of the mobile radio channel. A thorough understanding of the mobile radio channel is therefore crucial for the development, performance optimization, and testing of present as well as next-generation mobile radio systems. This is one of the reasons why exploring the mobile radio channel has always been a key research topic from the very beginning of mobile communications to the present. Currently, the research on mobile radio channels involves a variety of challenging topics such as the modeling of car-to-car channels, multiple-input multiple-output (MIMO) channels, cooperative channels, satellite channels, and ultrawideband channels, only to name a few. The objective of this special issue is to give an overview of the state-of-the-art research in the fascinating area of modeling and simulation of mobile radio channels. This special issue is composed of five papers.

The paper entitled “A Three-Dimensional Geometry-Based Statistical Model of 2×2 Dual-Polarized MIMO Mobile-to-Mobile Wideband Channels” uses a geometric scattering approach to derive a three-dimensional (3D) parametric reference model for wideband dual-polarized MIMO mobile-to-mobile (M2M) channels. The authors assume nonisotropic scattering, where the distribution of the scatterers is characterized in the azimuth direction through the von Mises distribution and in the elevation direction by the cosine distribution. The statistical properties of the

reference channel model are controlled by a large number of physical model parameters, including the velocities of the transmitter and the receiver, the distance between the transmitter and the receiver, the 3D antenna pattern gains, the azimuth and elevation angles of arrival (departure), the geometrical distribution of the scatterers, the Rician K-factor, the maximum Doppler frequency, the scattering loss factor, the cross-polar power discrimination ratio, and the copolarization power ratio. The spotlight here is on the derivation and analysis of the time-frequency correlation function of the proposed reference model for 3D nonisotropic scattering environments. With the knowledge of the time-frequency correlation function, an essential prerequisite is provided for the performance analysis and optimization of mobile-to-mobile communication systems employing 2×2 dual-polarized architectures.

The paper “An Accurate Hardware Sum-of-Cisoids Fading Channel Simulator for Isotropic and NonIsotropic Mobile Radio Environments” presents a hardware simulator for mobile fading channels characterized by Doppler power spectral densities with arbitrary symmetrical and asymmetrical shapes. The hardware simulator’s architecture described in this paper is based on an efficient implementation of the sum-of-cisoids principle. According to this principle, a finite number of complex sinusoids (cisoids) are combined to generate complex-valued waveforms with statistical properties resembling those of a given reference channel model. Each of the cisoids that constitute the sum-of-cisoids model is synthesized in hardware using a piecewise polynomial approximation technique, which offers a high-performance alternative to traditional solutions using look-up tables. The architecture of the hardware simulator is capable

of handling any configuration of the cisoids' amplitudes, frequencies, and phases. The flexibility and accuracy of the authors' implementation scheme are demonstrated through a variety of numerical results of the first- and second-order statistics of emulated Rayleigh fading channels assuming different isotropic and nonisotropic scattering conditions. The authors analyze the computational complexity of the hardware simulator in an FPGA implementation with 32 cisoids and different data path bit-widths. To better assess the complexity of their proposal, they provide a comparison with two alternative hardware fading channel simulators, which are also built on the sum-of-sinusoids principle. Aside from its efficiency and accuracy, the main feature of the hardware fading channel simulator presented in this paper is the capability of simulating mobile fading channels under a wide range of scattering conditions.

The paper "Filter-Based Fading Channel Modeling" outlines a filter-based approach for the design of fading channel simulators. As distinct from the sum-of-sinusoids concept, which has been studied extensively in the last two decades for the modeling and simulation of multipath fading channels, the filter concept has attracted only little attention in the past. This is mainly due to the design complexity of digital filters and its restriction to channel models described by rational Doppler power spectral densities. This third paper addresses the design of Rayleigh fading channel simulator using infinite impulse response (IIR) filters for shaping the Doppler spectrum. Specifically, the authors proposed an iterative technique for the IIR filter design with fixed-point arithmetic by considering both isotropic and nonisotropic scattering scenarios. The proposed iterative algorithm for the determination of the filter coefficients is described in a systematic manner. The authors also provide an overview of alternative methods for the design of digital filters and they discuss their respective advantages and disadvantages.

The authors of the paper, "Wideband and Ultrawideband Channel Models in Working Machine Environment," focus on a rather new topic in the area of mobile radio channel modeling. This paper presents statistical models for wideband and ultrawideband (UWB) radio channels in specific working environments, such as working machine cabins. From the analysis of measurement data collected in such kinds of rather small and confined propagation environments, it turned out that the channel impulse response is mainly composed of a sum of diffuse multipath components rather than of specular components. In wideband channels, the path gains associated with the various delay bins are generally Rayleigh distributed, whereas only a few path gains exhibit a Rician distribution. This is in contrast to UWB channels, in which the path gains associated with the delay bins show a tendency to follow the log-normal distribution. The results of the measurements were used to estimate the key channel parameters for the development of stochastic channel simulators. The developed mobile radio channel models provide important information to the designers of wireless communication systems dedicated to operate in working machine cabins.

In the paper "Design of Wideband MIMO Car-to-Car Channel Models Based on the Geometrical Street Scattering

Model," the authors deal with the modeling and simulation of channel models for car-to-car (C2C) communication systems. The starting point is an environment-specific geometrical street scattering model, which assumes that the local scatterers are uniformly distributed over two separated rectangular scattering areas located on opposite sides of the street. From the geometrical scattering model, the authors derive a reference model for a wideband MIMO C2C channel model by assuming that the number of scatterers is infinite. The statistical properties of the reference model are analyzed, where the emphasis lies on the space-time-frequency cross-correlation function from which many other important system functions and characteristic quantities can be easily derived. To validate the proposed channel model, the mean Doppler shift and the Doppler spread of the reference model have been matched to measurement data. In a further step, an efficient sum-of-cisoids channel simulator has been derived from the reference model. It is demonstrated that the statistical properties of the sum-of-cisoids channel simulator match very well those of the reference model. The proposed geometry-based channel simulator is useful for studying the effect of local scatterers along the street on the performance of C2C communication systems.

*Matthias Pätzold
Neji Youssef
Carlos A. Gutierrez*

Research Article

Design of Wideband MIMO Car-to-Car Channel Models Based on the Geometrical Street Scattering Model

Nurilla Avazov and Matthias Pätzold

Faculty of Engineering and Science, University of Agder, P.O. Box 509, 4898 Grimstad, Norway

Correspondence should be addressed to Nurilla Avazov, nurilla.k.avazov@uia.no

Received 2 May 2012; Revised 28 August 2012; Accepted 5 September 2012

Academic Editor: Neji Youssef

Copyright © 2012 N. Avazov and M. Pätzold. This is an open access article distributed under the Creative Commons Attribution License, which permits unrestricted use, distribution, and reproduction in any medium, provided the original work is properly cited.

We propose a wideband multiple-input multiple-output (MIMO) car-to-car (C2C) channel model based on the geometrical street scattering model. Starting from the geometrical model, a MIMO reference channel model is derived under the assumption of single-bounce scattering in line-of-sight (LOS) and non-LOS (NLOS) propagation environments. The proposed channel model assumes an infinite number of scatterers, which are uniformly distributed in two rectangular areas located on both sides of the street. Analytical solutions are presented for the space-time-frequency cross-correlation function (STF-CCF), the two-dimensional (2D) space CCF, the time-frequency CCF (TF-CCF), the temporal autocorrelation function (ACF), and the frequency correlation function (FCF). An efficient sum-of-cisoids (SOCs) channel simulator is derived from the reference model. It is shown that the temporal ACF and the FCF of the SOC channel simulator fit very well to the corresponding correlation functions of the reference model. To validate the proposed channel model, the mean Doppler shift and the Doppler spread of the reference model have been matched to real-world measurement data. The comparison results demonstrate an excellent agreement between theory and measurements, which confirms the validity of the derived reference model. The proposed geometry-based channel simulator allows us to study the effect of nearby street scatterers on the performance of C2C communication systems.

1. Introduction

C2C communications is an emerging technology, which receives considerable attention due to new traffic telematic applications that improve the efficiency of traffic flow and reduce the number of road accidents [1]. The development of C2C communication technologies is supported in Europe by respected organizations, such as the European Road Transport Telematics Implementation Coordinating Organization (ERTICO) [2] and the C2C Communication Consortium (C2C-CC) [3]. In this context, a large number of research projects focussing on C2C communications are currently being carried out throughout the world.

In C2C communication systems, the underlying radio channel differs from traditional fixed-to-mobile and mobile-to-fixed channels in the way that both the transmitter and the receiver are in motion. In this connection, robust and reliable traffic telematic systems have to be developed and tested, which calls for new channel models for C2C communication systems. Furthermore, MIMO communication systems can

also be of great interest for C2C communications due to their higher throughput [4]. In this regard, several MIMO mobile-to-mobile (M2M) channel models have been developed and analyzed under different scattering conditions induced by, for example, the two-ring model [5], the elliptical model [6], the T-junction model [7], and the geometrical street model [8, 9]. A 2D reference model for narrowband single-input single-output (SISO) M2M Rayleigh fading channels has been proposed by Akki and Haber in [10, 11]. Simulation models for SISO M2M channels have been reported in [12, 13]. In [5, 14, 15], the 2D reference and simulation models have been presented for narrowband MIMO M2M channels. The proposed model in [15] combines the two-ring model and the elliptical model, where a combination of single- and double-bounce scattering in LOS propagation environments is assumed.

All aforementioned channel models are narrowband M2M channel models. In contrast with narrowband channels, a channel is called a wideband channel or frequency-selective channel if the signal bandwidth significantly exceeds

the coherence bandwidth of the channel. Owing to increasing demands for high data rate wideband communication systems employing MIMO technologies, such as MIMO orthogonal frequency division multiplexing (OFDM) systems, it is of crucial importance to have accurate and realistic wideband MIMO M2M channel models. According to IEEE 802.11p [16], the dedicated frequency bands for short-range communications [17] will be between 5770 MHz and 5925 MHz depending on the region. The range 5795–5815 MHz will be devoted to Europe, while 5850–5925 MHz and 5770–5850 MHz will be assigned to North America and Japan, respectively. Consequently, a large number of C2C channel measurements have been carried out at different frequency bands, for example, at 2.4 GHz [18], 3.5 GHz [19], 5 GHz [20, 21], 5.2 GHz [22], and 5.9 GHz [23]. Real-world measurement campaigns for wideband C2C channels can be found in [24–27]. In the literature, there exist several papers [28–30] with the focus on the modeling of wideband MIMO M2M channels. A reference model derived from the geometrical T-junction scattering model has been proposed in [7] for wideband MIMO vehicle-to-vehicle (V2V) fading channels. In [29], a three-dimensional (3D) model for a wideband MIMO M2M channel has been studied. Its corresponding first- and second-order statistics have been investigated and validated on the basis of real-world measurement data. In the same paper, it has been shown that 3D scattering scenarios are more realistic than 2D scattering scenarios. However, 2D scattering models are more complexity efficient, and they provide a good approximation to 3D scattering models [31]. For those reasons, we propose in our paper a 2D street scattering model.

In the literature, numerous fundamental channel models with different scatterer distributions, such as the uniform, Gaussian, Laplacian, and von Mises distribution, have been proposed to characterize the angle-of-departure (AOD) and the angle-of-arrival (AOA) statistics. In [32], the author studied the effect of Gaussian distributed scatterers on the channel characteristics in a circular scattering region around a mobile station. The spatial and temporal properties of the first arrival path in multipath environments have also been analyzed in [32]. The authors of [9] assume rectangular scattering areas on both sides of the street, in which an infinite number of scatterers are uniformly distributed. It has been observed that the shape of the Doppler power spectral density (PSD) resembles a Gaussian function if the width of the scattering area is very large.

In contrast to our previous work in [9], where the focus was on the derivation of a reference channel model for narrowband SISO C2C channels, we design in this paper a wideband MIMO C2C channel model by starting from the same geometrical street scattering model. We focus on the statistical characterization of a wideband reference channel model assuming that an infinite number of scatterers are uniformly distributed within two rectangular areas. The radio propagation phenomena in street environments are modelled by a wide-sense stationary uncorrelated scattering process, where in addition a LOS component is taken into account. The reference model has been derived from the geometrical street scattering model assuming that the AOD

and the AOA are dependent due to single-bounce scattering. To account for the nature of C2C channels, we take the mobility of both the transmitter and the receiver for granted.

In our model, we consider a 2D street scattering environment to reduce the computational cost by still guaranteeing a good match between the reference model and measured channels. A typical propagation scenario for the proposed model is illustrated in Figure 1, where the buildings and the trees are considered as scattering objects. Such a typical dense urban environment scenario allows us to assume that the local scatterers are uniformly distributed in a specific area. An analytical expression will be derived for the STF-CCF from which the 2D space CCF, the TF-CCF, the temporal ACF, and the FCF can be obtained directly. To validate the proposed reference model, the mean Doppler shift and the Doppler spread of the reference model have been matched to the corresponding quantities of the measured channel described in [25] for different propagation environments, such as urban, rural, and highway areas. Furthermore, we have derived an SOC channel simulator from the reference model. It is shown that the designed channel simulator matches the underlying reference model with respect to the temporal ACF and the FCF.

The rest of this paper is organized as follows. Section 2 describes the geometrical street scattering model. In Section 3, the reference channel model is derived from the geometrical street model. Section 4 analyzes the correlation properties of the reference model, such as the STF-CCF, the 2D space CCF, the TF-CCF, the temporal ACF, and the FCF. The computation of the measurement-based model parameters and the characteristic quantities describing the Doppler effect are discussed in Section 5. Section 6 describes briefly the simulation model derived from the reference model. The illustration of some numerical results found for the correlation functions of the reference model and the corresponding simulation model is the topic of Section 7. Finally, Section 8 draws the conclusion of the paper.

2. The Geometrical Street Scattering Model

This section briefly describes the geometrical street scattering model for wideband MIMO C2C channels. The proposed geometrical model describes the scattering environment in an urban area, where the scatterers are located in two rectangular areas on both sides of the street as illustrated in Figure 2. We consider rectangular grids formed by rows and columns, where the length and the width of the rectangular grids are denoted by $L_A = A_1 + A_2$ and B_i ($i = 1, 2$), respectively. The scatterer located in the m th column of the n th row is denoted by $S^{(mn)}$ ($m = 1, 2, \dots, M$, $n = 1, 2, \dots, N$). It is assumed that the local scatterers $S^{(mn)}$ are uniformly distributed in the rectangles. The symbols MS_T and MS_R in Figure 2 stand for the mobile transmitter and the mobile receiver, respectively. The symbol D represents the scalar projection of the distance between the transmitter and the receiver onto the x -axis. The transmitter (receiver) is located at a distance y_{T_1} (y_{R_1}) from the left-hand side of the street and at a distance y_{T_2} (y_{R_2}) from the right-hand side of the street. Both the transmitter and the receiver are in motion

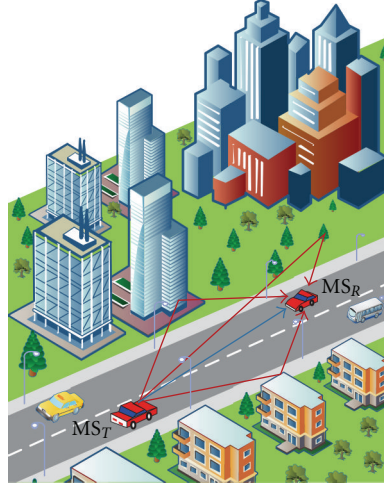


FIGURE 1: A typical propagation scenario along a straight street in urban areas.

and equipped with M_T transmitter antenna elements and M_R receiver antenna elements, respectively. The antenna element spacings at the transmitter and the receiver are denoted by δ_T and δ_R , respectively. The symbols $\alpha_T^{(mn)}$ and $\alpha_R^{(mn)}$ denote the AOD and the AOA, respectively. The angle γ_T (γ_R) describes the tilt angle of the transmitter (receiver) antenna array. Moreover, it is assumed that the transmitter (receiver) moves with speed v_T (v_R) in the direction determined by the angle of motion φ_v^T (φ_v^R).

3. The Reference Model

3.1. Derivation of the Reference Model. In this section, we derive the reference model for the MIMO C2C channel under the assumption of LOS and NLOS propagation conditions. From Figure 2, we realize that the (mn) th homogeneous plane wave emitted from the l th antenna element $A_T^{(l)}$ ($l = 1, 2, \dots, M_T$) of the transmitter travels over the local scatterer $S^{(mn)}$ before impinging on the k th antenna element $A_R^{(k)}$ ($k = 1, 2, \dots, M_R$) of the receiver. The reference model is based on the assumption that the number of local scatterers within both rectangular areas is infinite, that is, $M, N \rightarrow \infty$. The temporal, spatial, and frequency characteristics of the reference model are determined by the $M_R \times M_T$ channel matrix $\mathbf{H}(f', t) = [H_{kl}(f', t)]_{M_R \times M_T}$, where $H_{kl}(f', t)$ denotes the time-variant transfer function (TVTF) of the channel for the link between the l th transmitter antenna element $A_T^{(l)}$ and the k th receiver antenna element $A_R^{(k)}$. The TVTF $H_{kl}(f', t)$ can be expressed as a superposition of the diffuse component and the LOS component as follows:

$$H_{kl}(f', t) = H_{kl}^{\text{DIF}}(f', t) + H_{kl}^{\text{LOS}}(f', t), \quad (1)$$

where $H_{kl}^{\text{DIF}}(f', t)$ and $H_{kl}^{\text{LOS}}(f', t)$ represent the diffuse and the LOS components of the channel, respectively.

Note that the single-bounce scattering components bear more energy than the double-bounce scattering components. Hence, in our analysis, we model the diffuse component $H_{kl}^{\text{DIF}}(f', t)$ by only taking into account the single-bounce

scattering effects, which is in accordance with the assumptions made in [28, 33]. From the geometrical street scattering model shown in Figure 2, we can derive the TVTF of the diffuse component, which results in the following expression:

$$H_{kl}^{\text{DIF}}(f', t) = \lim_{M, N \rightarrow \infty} \frac{1}{\sqrt{(c_R + 1)MN}} \sum_{m, n=1}^{M, N} a_{l, mn} b_{k, mn} c_{mn} \cdot e^{j[\theta_{mn} + 2\pi(f_T^{(mn)} + f_R^{(mn)})t - 2\pi f' \tau'_{kl}{}^{(mn)}]}, \quad (2)$$

where

$$a_{l, mn} = e^{j\pi(\delta_T/\lambda)(M_T - 2l + 1) \cos(\alpha_T^{(mn)} - \gamma_T)}, \quad (3)$$

$$b_{k, mn} = e^{j\pi(\delta_R/\lambda)(M_R - 2k + 1) \cos(\alpha_R^{(mn)} - \gamma_R)}, \quad (4)$$

$$c_{mn} = e^{-j(2\pi/\lambda)(\gamma_{T1}/\sin(\alpha_T^{(mn)}) + \gamma_{R1}/\sin(\alpha_R^{(mn)}))}, \quad (5)$$

$$f_T^{(mn)} = f_{T_{\max}} \cos(\alpha_T^{(mn)} - \varphi_v^T), \quad (6)$$

$$f_R^{(mn)} = f_{R_{\max}} \cos(\alpha_R^{(mn)} - \varphi_v^R), \quad (7)$$

$$\tau'_{kl}{}^{(mn)} = \frac{1}{c_0} [D_T^{(l, mn)} + D_R^{(mn, k)}]. \quad (8)$$

In (6) and (7), the symbols $f_{T_{\max}} = v_T/\lambda$ and $f_{R_{\max}} = v_R/\lambda$ denote the maximum Doppler frequencies associated with the movement of the transmitter and the receiver, respectively, and λ is the wavelength. The symbol c_R in (2) represents the Rice factor, which is defined as the ratio of the power of the LOS component to the power of the diffuse component, that is, $c_R = E\{|H_{kl}^{\text{LOS}}(f', t)|^2\}/E\{|H_{kl}^{\text{DIF}}(f', t)|^2\}$. The phases θ_{mn} in (2) denote the phase shift introduced by the scatterer $S^{(mn)}$. It is assumed that the phases θ_{mn} are independent, identically distributed (i.i.d.) random variables, which are uniformly distributed over the interval $[0, 2\pi)$. The symbols $\tau'_{kl}{}^{(mn)}$ and c_0 represent the propagation delays of the diffuse component and the speed of light, respectively. In (8), the quantity $D_T^{(l, mn)}$

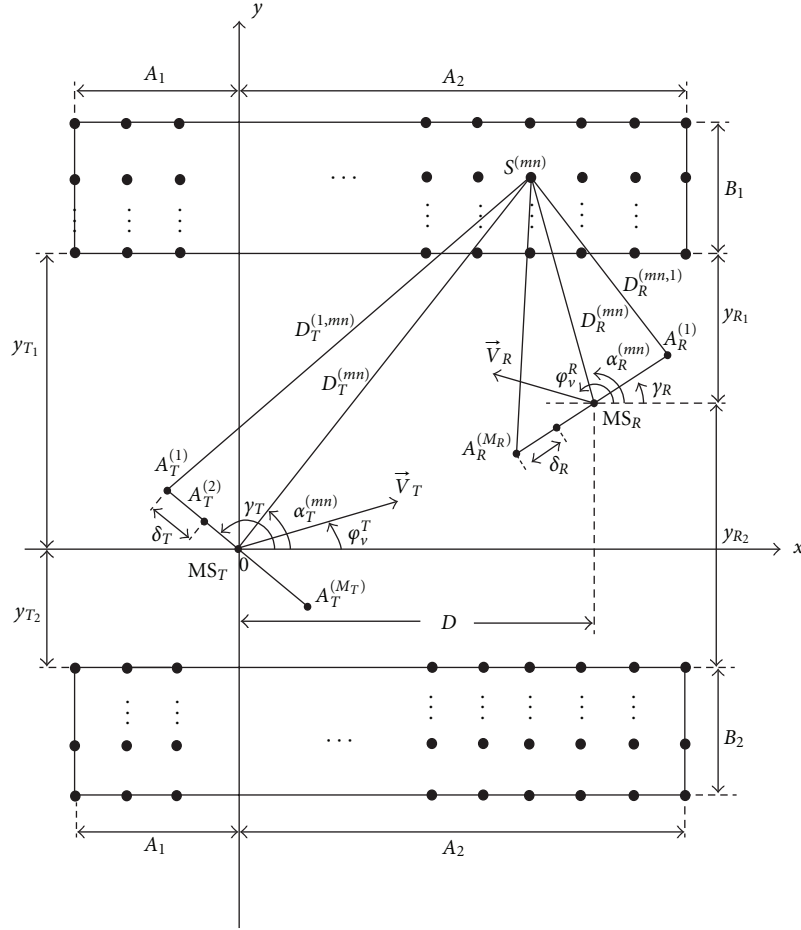


FIGURE 2: The geometrical street scattering model with local scatterers uniformly distributed in two rectangular areas on both sides of the street.

stands for the distance from the l th transmitter antenna element $A_T^{(l)}$ to the scatterer $S^{(mn)}$, whereas $D_R^{(mn,k)}$ is the distance between the scatterer $S^{(mn)}$ and the k th receiver antenna element $A_R^{(k)}$. It is assumed that $(M_T - 1)\delta_T \ll \min\{y_{T1}, y_{T2}\}$ and $(M_R - 1)\delta_R \ll \min\{y_{R1}, y_{R2}\}$. These assumptions, together with the approximation $\sqrt{1+x} \approx 1 + x/2$ ($x \ll 1$), allow us to approximate the two distances $D_T^{(l,mn)}$ and $D_R^{(mn,k)}$ as follows:

$$D_T^{(l,mn)} \approx D_T^{(mn)} - (M_T - 2l + 1) \left(\frac{\delta_T}{2} \right) \cos(\alpha_T^{(mn)} - \gamma_T), \quad (9)$$

$$D_R^{(mn,k)} \approx D_R^{(mn)} - (M_R - 2k + 1) \left(\frac{\delta_R}{2} \right) \cos(\alpha_R^{(mn)} - \gamma_R), \quad (10)$$

where $D_T^{(mn)}$ and $D_R^{(mn)}$ are given by $D_T^{(mn)} = y_{T1} / \sin(\alpha_T^{(mn)})$ and $D_R^{(mn)} = y_{R1} / \sin(\alpha_R^{(mn)})$, respectively.

It is noteworthy that one can also find articles [11, 34], in which only double-bounce scattering is assumed for M2M communications. However, by following a similar approach as in [15], one can easily extend our analysis on the basis of single-bounce scattering to the case of double-bounce

scattering, and thus also to a combination of single- and double-bounce scattering.

The TVTF of the LOS component is given by

$$H_{kl}^{\text{LOS}}(f', t) = \sqrt{\frac{cR}{(cR + 1)}} e^{j[2\pi(f_T^{(0)} + f_R^{(0)})t - (2\pi/\lambda)D_{kl} - 2\pi f' \tau_{kl}^{(0)}]}, \quad (11)$$

where

$$f_T^{(0)} = f_{T_{\max}} \cos(\alpha_T^{(0)} - \varphi_V^T), \quad (12)$$

$$f_R^{(0)} = f_{R_{\max}} \cos(\alpha_R^{(0)} - \varphi_V^R), \quad (13)$$

$$D_{kl} = D_0 - (M_T - 2l + 1) \frac{\delta_T}{2} \cos(\gamma_T) + (M_R - 2k + 1) \frac{\delta_R}{2} \cos(\gamma_R), \quad (14)$$

$$D_0 = \sqrt{D^2 + (y_{T1} - y_{R1})^2}. \quad (15)$$

In (11), $f_T^{(0)}$ and $f_R^{(0)}$ denote the Doppler shifts of the LOS component caused by the movement of the transmitter and the receiver, respectively. The symbols $\alpha_T^{(0)}$ and $\alpha_R^{(0)}$

in (12) and (13) represent the AOD and the AOA of the LOS component, respectively. Finally, $\tau'_{kl}{}^{(0)}$ denotes the propagation delay of the LOS component. The delay of the LOS component is defined by $\tau'_{kl}{}^{(0)} = D_{kl}/c_0$ with D_{kl} being the length of the direct path from the l th transmitter antenna element $A_T^{(l)}$ to the k th receiver antenna element $A_R^{(k)}$. The symbol D_0 in (14) denotes the Euclidean distance between the transmitter and the receiver. According to [35], the LOS component $H_{kl}^{\text{LOS}}(f', t)$ is assumed to be a deterministic process, while the diffuse component $H_{kl}^{\text{DIF}}(f', t)$ is a stochastic process.

3.2. Derivation of the AOD and the AOA. The position of all local scatterers $S^{(mn)}$ is described by the Cartesian coordinates (x_m, y_n) . In the reference model, the coordinates x_m and y_n are independent random variables, which are determined by the distribution of the local scatterers. With reference to Figure 2, we take into account that due to single-bounce scattering, the AOD $\alpha_T^{(mn)}$ and the AOA $\alpha_R^{(mn)}$ are dependent. By using the trigonometric identities, we can express the AOD $\alpha_T^{(mn)}$ and the AOA $\alpha_R^{(mn)}$ in terms of the coordinates (x_m, y_n) of the local scatterers $S^{(mn)}$ as follows:

$$\alpha_T^{(mn)}(x_m, y_n) = \begin{cases} g(x_m, y_n), & \text{if } y_n \in J_i, x_m \in [0, A_2] \\ (-1)^{i+1}\pi + g(x_m, y_n), & \text{if } y_n \in J_i, x_m \in [-A_1, 0] \end{cases} \quad (16)$$

$$\alpha_R^{(mn)}(x_m, y_n) = \begin{cases} f(x_m, y_n), & \text{if } y_n \in J_i, x_m \in [D, A_2] \\ (-1)^{i+1}\pi + f(x_m, y_n), & \text{if } y_n \in J_i, x_m \in [-A_1, D] \end{cases} \quad (17)$$

for $i = 1, 2$, where $J_1 = [y_{T_1}, y_{T_1} + B_1]$, $J_2 = [-y_{T_2} - B_2, -y_{T_2}]$, and

$$\begin{aligned} g(x_m, y_n) &= \arctan \frac{y_n}{x_m} \\ f(x_m, y_n) &= \arctan \frac{y_n - y_{T_1} + y_{R_1}}{x_m - D}. \end{aligned} \quad (18)$$

4. Correlation Properties of the Reference Model

In this section, we derive a general analytical solution for the STF-CCF, from which other correlation functions, such as the 2D space CCF, the TF-CCF, the temporal ACF, and the FCF can easily be derived.

4.1. Derivation of the STF-CCF. According to [10], the STF-CCF of the links $A_T^{(l)} - A_R^{(k)}$ and $A_T^{(l')} - A_R^{(k')}$ is defined as the

correlation between the channel transfer functions $H_{kl}(f', t)$ and $H_{k'l'}(f', t)$, that is,

$$\begin{aligned} \rho_{kl,k'l'}(\delta_T, \delta_R, \nu', \tau) &= E\left\{H_{kl}^*(f', t)H_{k'l'}(f' + \nu', t + \tau)\right\} \\ &= \rho_{kl,k'l'}^{\text{DIF}}(\delta_T, \delta_R, \nu', \tau) \\ &\quad + \rho_{kl,k'l'}^{\text{LOS}}(\delta_T, \delta_R, \nu', \tau), \end{aligned} \quad (19)$$

where $(*)$ denotes the complex conjugate operator and $E\{\cdot\}$ stands for the expectation operator that applies to all random variables: the phases $\{\theta_{mn}\}$ and the coordinates (x_m, y_n) of the scatterers $S^{(mn)}$. The first term $\rho_{kl,k'l'}^{\text{DIF}}(\delta_T, \delta_R, \nu', \tau)$ represents the STF-CCF of the diffuse component. This correlation function can be expressed, after substituting (2) in (19), by

$$\begin{aligned} \rho_{kl,k'l'}^{\text{DIF}}(\delta_T, \delta_R, \nu', \tau) &= \lim_{M,N \rightarrow \infty} \frac{1}{(C_R + 1)MN} \\ &\quad \times \sum_{m,n=1}^{M,N} E\left\{c_{ll'}^{(mn)} d_{kk'}^{(mn)} e^{j2\pi[(f_T^{(mn)} + f_R^{(mn)})\tau - \nu' \tau'_{kl}{}^{(mn)}]}\right\}, \end{aligned} \quad (20)$$

where

$$\begin{aligned} c_{ll'}^{(mn)} &= e^{j2\pi(\delta_T/\lambda)(l-l')\cos(\alpha_T^{(mn)} - \gamma_T)}, \\ d_{kk'}^{(mn)} &= e^{j2\pi(\delta_R/\lambda)(k-k')\cos(\alpha_R^{(mn)} - \gamma_R)}. \end{aligned} \quad (21)$$

The quantities $f_T^{(mn)}$, $f_R^{(mn)}$, and $\tau'_{kl}{}^{(mn)}$ are given by (6), (7), and (8), respectively. We recall that the AOD $\alpha_T^{(mn)}$ and the AOA $\alpha_R^{(mn)}$ can be expressed in terms of the random variables x_m and y_n according to (16) and (17), respectively.

In Section 2, it has been mentioned that all scatterers are uniformly distributed in the two rectangular areas on both sides of the street, as illustrated in Figure 2. Hence, the random variables x_m and y_n are also uniformly distributed over the rectangular areas. If the number of scatterers tends to infinity, that is, $M, N \rightarrow \infty$, then the discrete random variables x_m and y_n become continuous random variables denoted by x and y , respectively. Thus, the probability density functions (PDFs) $p_x(x)$ and $p_y(y)$ of x and y , respectively, are given by

$$\begin{aligned} p_x(x) &= \frac{1}{L_A}, \quad \text{if } x \in [-A_1, A_2], \\ p_y(y) &= \begin{cases} \frac{1}{2B_1}, & \text{if } y \in [y_{T_1}, B_1 + y_{T_1}] \\ \frac{1}{2B_2}, & \text{if } y \in [-B_2 - y_{T_2}, -y_{T_2}], \end{cases} \end{aligned} \quad (22)$$

where $L_A = A_1 + A_2$. Assuming that the random variables x and y are independent, the joint PDF $p_{xy}(x, y)$ of the

random variables x and y can be expressed as a product of the marginal PDFs $p_x(x)$ and $p_y(y)$, that is,

$$\begin{aligned} p_{xy}(x, y) &= p_x(x) \cdot p_y(y) \\ &= \begin{cases} \frac{1}{2L_A B_1}, & \text{if } x \in [-A_1, A_2], y \in [y_{T_1}, B_1 + y_{T_1}] \\ \frac{1}{2L_A B_2}, & \text{if } x \in [-A_1, A_2], y \in [-B_2 - y_{T_2}, -y_{T_2}]. \end{cases} \end{aligned} \quad (23)$$

The infinitesimal power of the diffuse component corresponding to the differential axes dx and dy is proportional to $p_{xy}(x, y)dx dy$. As $M, N \rightarrow \infty$, this infinitesimal contribution must be equal to $1/MN = p_{xy}(x, y)dx dy$. Consequently, it follows from (20) that the STF-CCF of the diffuse component can be expressed as

$$\begin{aligned} \rho_{kl, k'l'}^{\text{DIF}}(\delta_T, \delta_R, \nu', \tau) &= \frac{1}{2L_A B_1 (c_R + 1)} \int_{y_{T_1}}^{y_{T_1} + B_1} \int_{-A_1}^{A_2} c_{ll'}^{\text{DIF}}(\delta_T, x, y) d_{kk'}^{\text{DIF}}(\delta_R, x, y) \\ &\quad \times e^{j2\pi[(f_T(x, y) + f_R(x, y))\tau - \nu' \tau'_{kl}(x, y)]} dx dy \\ &\quad + \frac{1}{2L_A B_2 (c_R + 1)} \\ &\quad \times \int_{-B_2 - y_{T_2}}^{-y_{T_2}} \int_{-A_1}^{A_2} c_{ll'}^{\text{DIF}}(\delta_T, x, y) d_{kk'}^{\text{DIF}}(\delta_R, x, y) \\ &\quad \times e^{j2\pi[(f_T(x, y) + f_R(x, y))\tau - \nu' \tau'_{kl}(x, y)]} dx dy, \end{aligned} \quad (24)$$

where

$$\begin{aligned} c_{ll'}^{\text{DIF}}(\delta_T, x, y) &= e^{j2\pi(\delta_T/\lambda)(l-l') \cos(\alpha_T(x, y) - \gamma_T)}, \\ d_{kk'}^{\text{DIF}}(\delta_R, x, y) &= e^{j2\pi(\delta_R/\lambda)(k-k') \cos(\alpha_R(x, y) - \gamma_R)}, \\ f_T(x, y) &= f_{T_{\max}} \cos(\alpha_T(x, y) - \phi_v^T), \\ f_R(x, y) &= f_{R_{\max}} \cos(\alpha_R(x, y) - \phi_v^R), \\ \tau'_{kl}(x, y) &= \frac{1}{c_0} [D_T^{(l)}(x, y) + D_R^{(k)}(x, y)]. \end{aligned} \quad (25)$$

Using the functions in (9) and (10), the distances $D_T^{(l)}(x, y)$ and $D_R^{(k)}(x, y)$ can be expressed as

$$\begin{aligned} D_T^{(l)}(x, y) &\approx \frac{y_{T_1}}{\sin(\alpha_T(x, y))} \\ &\quad - (M_T - 2l + 1) \left(\frac{\delta_T}{2} \right) \cos(\alpha_T(x, y) - \gamma_T), \\ D_R^{(k)}(x, y) &\approx \frac{y_{R_1}}{\sin(\alpha_R(x, y))} \\ &\quad - (M_R - 2k + 1) \left(\frac{\delta_R}{2} \right) \cos(\alpha_R(x, y) - \gamma_R). \end{aligned} \quad (26)$$

In (19), the quantity $\rho_{kl, k'l'}^{\text{LOS}}(\delta_T, \delta_R, \nu', \tau)$, which represents the STF-CCF of the LOS component, can be written as

$$\begin{aligned} \rho_{kl, k'l'}^{\text{LOS}}(\delta_T, \delta_R, \nu', \tau) &= \frac{c_R}{(c_R + 1)} c_{ll'}^{(0)}(\delta_T) \\ &\quad \times d_{kk'}^{(0)}(\delta_R) e^{j2\pi[(f_T^{(0)} + f_R^{(0)})\tau - \nu' \tau'_{kl}^{(0)}]}, \end{aligned} \quad (27)$$

where

$$c_{ll'}^{(0)}(\delta_T) = e^{j2\pi(\delta_T/\lambda)(l-l') \cos(\gamma_T)}, \quad (28)$$

$$d_{kk'}^{(0)}(\delta_R) = e^{-j2\pi(\delta_R/\lambda)(k-k') \cos(\gamma_R)}. \quad (29)$$

The Doppler shifts $f_T^{(0)}$ and $f_R^{(0)}$ are given by (12) and (13), respectively.

4.2. Derivation of the 2D Space CCF. The 2D space CCF $\rho_{kl, k'l'}(\delta_T, \delta_R)$ is defined as $\rho_{kl, k'l'}(\delta_T, \delta_R) = E\{H_{kl}^*(f', t)H_{k'l'}(f', t)\}$, which is equal to the STF-CCF $\rho_{kl, k'l'}(\delta_T, \delta_R, \nu', \tau)$ in (19) by setting ν' and τ to zero, that is,

$$\begin{aligned} \rho_{kl, k'l'}(\delta_T, \delta_R) &= \rho_{kl, k'l'}(\delta_T, \delta_R, 0, 0) \\ &= \frac{1}{2L_A B_1 (c_R + 1)} \int_{y_{T_1}}^{y_{T_1} + B_1} \\ &\quad \times \int_{-A_1}^{A_2} c_{ll'}^{\text{DIF}}(\delta_T, x, y) d_{kk'}^{\text{DIF}}(\delta_R, x, y) dx dy \\ &\quad + \frac{1}{2L_A B_2 (c_R + 1)} \int_{-B_2 - y_{T_2}}^{-y_{T_2}} \\ &\quad \times \int_{-A_1}^{A_2} c_{ll'}^{\text{DIF}}(\delta_T, x, y) d_{kk'}^{\text{DIF}}(\delta_R, x, y) dx dy \\ &\quad + \frac{c_R}{(c_R + 1)} c_{ll'}^{(0)}(\delta_T) d_{kk'}^{(0)}(\delta_R). \end{aligned} \quad (30)$$

4.3. Derivation of the TF-CCF. The TF-CCF of the transmission link from $A_T^{(l)}$ ($l = 1, 2, \dots, M_T$) to $A_R^{(k)}$ ($k = 1, 2, \dots, M_R$) is defined by $r_{kl}(\nu', \tau) := E\{H_{kl}^*(f', t)H_{kl}(f' + \nu', t + \tau)\}$ [36]. The TF-CCF can be obtained directly from the STF-CCF [see (19)] by setting the antenna element spacings δ_T and δ_R to zero, that is,

$$\begin{aligned} r_{kl}(\nu', \tau) &= \rho_{kl, k'l'}^{\text{DIF}}(0, 0, \nu', \tau) + \rho_{kl, k'l'}^{\text{LOS}}(0, 0, \nu', \tau) \\ &= \frac{1}{2L_A B_1 (c_R + 1)} \int_{y_{T_1}}^{y_{T_1} + B_1} \\ &\quad \times \int_{-A_1}^{A_2} e^{j2\pi[(f_T(x, y) + f_R(x, y))\tau - \nu' \tau'_{kl}(x, y)]} dx dy \\ &\quad + \frac{1}{2L_A B_2 (c_R + 1)} \int_{-B_2 - y_{T_2}}^{-y_{T_2}} \\ &\quad \times \int_{-A_1}^{A_2} e^{j2\pi[(f_T(x, y) + f_R(x, y))\tau - \nu' \tau'_{kl}(x, y)]} dx dy \\ &\quad + \frac{c_R}{(c_R + 1)} e^{j2\pi(f_T^{(0)} + f_R^{(0)})\tau} e^{-j2\pi\nu' \tau'_{kl}^{(0)}}. \end{aligned} \quad (31)$$

4.4. *Derivation of the Temporal ACF and the Doppler PSD.* The temporal ACF of the transmission link from $A_T^{(l)}$ ($l = 1, 2, \dots, M_T$) to $A_R^{(k)}$ ($k = 1, 2, \dots, M_R$) is defined by $r_{kl}(\tau) := E\{H_{kl}^*(f', t)H_{kl}(f', t + \tau)\}$ [36, Page 376]. The temporal ACF can be obtained directly from the TF-CCF (see (31)) by setting at ν' to zero, that is, $r_{kl}(\tau) = r_{kl}(\tau, 0)$, which gives

$$\begin{aligned} r_{kl}(\tau) &= \frac{1}{2L_A B_1 (c_R + 1)} \int_{y_{T_1}}^{y_{T_1} + B_1} \\ &\quad \times \int_{-A_1}^{A_2} e^{j2\pi[f_T(x,y) + f_R(x,y)]\tau} dx dy \\ &+ \frac{1}{2L_A B_2 (c_R + 1)} \int_{-B_2 - y_{T_2}}^{-y_{T_2}} \\ &\quad \times \int_{-A_1}^{A_2} e^{j2\pi[f_T(x,y) + f_R(x,y)]\tau} dx dy \\ &+ \frac{c_R}{(c_R + 1)} e^{j2\pi(f_T^{(0)} + f_R^{(0)})\tau}. \end{aligned} \quad (32)$$

Notice that the expression in (32) reveals that the ACF $r_{kl}(\tau)$ is independent of k and l .

Computing the Fourier transform of the temporal ACF $r_{kl}(\tau)$ results in the Doppler PSD $S_{kl}(f)$, that is,

$$S_{kl}(f) = \int_{-\infty}^{\infty} r_{kl}(\tau) e^{-j2\pi f \tau} d\tau. \quad (33)$$

The two most important statistical quantities characterizing the Doppler PSD $S_{kl}(f)$ are the average Doppler shift $B_{kl}^{(1)}$ and the Doppler spread $B_{kl}^{(2)}$ [35]. The average Doppler shift $B_{kl}^{(1)}$ is defined as the first moment of $S_{kl}(f)$, which can be expressed as follows:

$$B_{kl}^{(1)} = \frac{\int_{-\infty}^{\infty} f S_{kl}(f) df}{\int_{-\infty}^{\infty} S_{kl}(f) df}. \quad (34)$$

The Doppler spread $B_{kl}^{(2)}$ is defined as the square root of the second central moment of $S_{kl}(f)$, which can be written as

$$B_{kl}^{(2)} = \sqrt{\frac{\int_{-\infty}^{\infty} (f - B_{kl}^{(1)})^2 S_{kl}(f) df}{\int_{-\infty}^{\infty} S_{kl}(f) df}}. \quad (35)$$

4.5. *Derivation of the FCF.* The frequency characteristics of the reference model are described by the FCF $r_{kl}(\nu')$. The FCF $r_{kl}(\nu')$ of the transmission link from $A_T^{(l)}$ to $A_R^{(k)}$ is defined by $r_{kl}(\nu') := E\{H_{kl}^*(f', t)H_{kl}(f' + \nu', t)\}$ for all $l = 1, 2, \dots, M_T$ and $k = 1, 2, \dots, M_R$. This function can be obtained directly

from the TF-CCF [see (31)] by setting τ to zero, that is, $r_{kl}(\nu') = r_{kl}(0, \nu')$, which results in

$$\begin{aligned} r_{kl}(\nu') &= \frac{1}{2L_A B_1 (c_R + 1)} \int_{y_{T_1}}^{y_{T_1} + B_1} \int_{-A_1}^{A_2} e^{-j2\pi\nu' \tau_{kl}^{(0)}(x,y)} dx dy \\ &+ \frac{1}{2L_A B_2 (c_R + 1)} \int_{-B_2 - y_{T_2}}^{-y_{T_2}} \int_{-A_1}^{A_2} e^{-j2\pi\nu' \tau_{kl}^{(0)}(x,y)} dx dy \\ &+ \frac{c_R}{(c_R + 1)} e^{-j2\pi\nu' \tau_{kl}^{(0)}}. \end{aligned} \quad (36)$$

In contrast to the temporal ACF $r_{kl}(\tau)$, the FCF $r_{kl}(\nu')$ depends on k and l .

5. Measurement-Based Computation of the Model Parameters

The objective of this section is to determine the set of model parameters $\mathcal{P} = \{A_1, A_2, B_1, B_2, y_{T_1}, y_{T_2}, y_{R_1}, y_{R_2}, D, f_{T_{\max}}, f_{R_{\max}}, c_R\}$ describing the reference model in such a way that the average Doppler shift $B_{kl}^{(1)}$ and the Doppler spread $B_{kl}^{(2)}$ of the reference model match the corresponding quantities ($B_{kl}^{*(1)}$ and $B_{kl}^{*(2)}$) of the measured channel reported in [25]. To determine the set of model parameters \mathcal{P} , we minimize the following error:

$$E_{\min} = W_1 E_{B_{kl}^{(1)}} + W_2 E_{B_{kl}^{(2)}}, \quad (37)$$

where W_1 and W_2 denote the weighting factors. The symbols $E_{B_{kl}^{(1)}}$ and $E_{B_{kl}^{(2)}}$ in (37) stand for the absolute errors of the average Doppler shift and Doppler spread, respectively, which are defined as

$$E_{B_{kl}^{(1)}} = \arg \min_{\mathcal{P}} |B_{kl}^{*(1)} - B_{kl}^{(1)}|, \quad (38)$$

$$E_{B_{kl}^{(2)}} = \arg \min_{\mathcal{P}} |B_{kl}^{*(2)} - B_{kl}^{(2)}|. \quad (39)$$

In (38) and (39), the notation $\arg \min_x f(x)$ stands for the argument of the minimum, which is the set of points of the given argument for which $f(x)$ reaches its minimum value. At the beginning of the optimization procedure, the weighting factors W_1 and W_2 are selected arbitrarily, but such that they satisfy the equality $W_1 + W_2 = 1$. If the error $E_{B_{kl}^{(i)}}$ ($i = 1, 2$) in (37) is large, then we reduce the corresponding weighting factor W_i and vice versa. We continue the optimization procedure until the result in (37) reaches an error floor, meaning that the average Doppler shift and the Doppler spread of the reference model best match the measured average Doppler shift and the measured Doppler spread, respectively.

For the measured channels in [25], the resulting optimized model parameters and the corresponding average Doppler shift and Doppler spread are listed in Table 1. The results found for the reference model demonstrate an excellent fitting to real-world measured channels for rural, urban, and highway propagation areas, which validates the usefulness of the proposed reference model. It is worth

TABLE 1: Measurement-based parameters of the geometrical street scattering model and the resulting average Doppler shift and the Doppler spread.

Model parameters	Propagation environment				
	Urban LOS	Urban NLOS	Rural LOS	Highway LOS	Highway NLOS
$A_1(A_2)$ (m)	546.28 (1249)	537.03 (908.3)	546.52 (1236)	547.69 (1207)	546.88 (1193)
$B_1(B_2)$ (m)	198.96 (198.77)	76.46 (1.1113)	20.89 (18.25)	199.8 (200)	0.01 (0.01)
$f_{T_{\max}}(f_{R_{\max}})$ (Hz)	223.55 (219.77)	262.1 (209.97)	463.72 (491.65)	511.68 (442.62)	491.67 (481.97)
$y_{T1}(y_{T2})$ (m)	10.42 (7)	2.12 (1.18)	15.28 (4.63)	17.62 (19.78)	1.3 (1.3)
$y_{R1}(y_{R2})$ (m)	19.82 (6.6)	20 (7.06)	14.57 (9.4)	19.63 (25)	20 (9.4)
D (m)	238.6	236.7	186.77	896.7	749.6
c_R	0.485	0	0.27	0.4	0
Measured					
average Doppler shift $B_{kl}^{*(1)}$ (Hz) [25]	-20	103	201	209	-176
Theoretical					
average Doppler shift $B_{kl}^{(1)}$ (Hz)	-20	102.67	200.55	208.8	-110
Measured					
Doppler spread $B_{kl}^{*(2)}$ (Hz) [25]	341	298	782	761	978
Theoretical					
Doppler spread $B_{kl}^{(2)}$ (Hz)	341	298	782.03	760.88	941

mentioning that the computed average Doppler shift $B_{kl}^{(1)} = -110$ Hz and the Doppler spread $B_{kl}^{(2)} = 941$ Hz do not closely agree with the measured channel ($B_{kl}^{*(1)} = -176$ Hz and $B_{kl}^{*(2)} = 978$ Hz) in case of the highway NLOS scenario. For this scenario, a close agreement can be found for sufficiently small values of $c_R \neq 0$.

6. The Simulation Model

The reference model described above is a theoretical model, which is based on the assumption that the number of scatterers (M, N) is infinite. Owing to an infinite realization complexity, the reference model is non-realizable. However, the reference model can serve as a ground for the derivation of stochastic and deterministic simulation models. According to the generalized principle of deterministic channel modeling [35, Sec. 8.1], a stochastic simulation model can be derived from the reference model introduced in (1) by using only a finite number of scatterers. In the literature, several different models exist that allow for a proper simulation of mobile channels. The SOC model is an appropriate simulation model for mobile radio channels under non-isotropic scattering conditions. A detailed description and the design of SOC models can be found in [37, 38], respectively. In [38], several parametrization techniques for SOC models have been discussed and analyzed. Here, we use the L_p -norm method (LPNM), which is a high-performance parameter computation method for the design of SOC channel simulators.

7. Numerical Results

This section illustrates the analytical results given by (30), (31), (32), and (36). The correctness of the analytical results will be verified by simulations. The performance of the channel simulator has been assessed by comparing its temporal ACF and the FCF to the corresponding system functions of the reference model (see (32) and (36)).

As an example for our geometrical street scattering model, we consider rectangular scattering areas on both sides of the street with a length of $L_A = A_1 + A_2$, where $A_1 = 50$ m and $A_2 = 450$ m, and a width of $B_1 = B_2 = 100$ m. With reference to Figure 2, the position of the transmitter and the receiver are defined by the distances $D = 400$ m, $y_{T1} = y_{R2} = 20$ m, and $y_{T2} = y_{R1} = 10$ m. For the reference model, all theoretical results have been obtained by choosing the following parameters: $\gamma_T = 90^\circ$, $\gamma_R = 90^\circ$, $\varphi_v^T = 0^\circ$, $\varphi_v^R = 180^\circ$, and $f_{T_{\max}} = f_{R_{\max}} = 91$ Hz. The Rice factor c_R was chosen from the set $\{0, 0.5, 1\}$. The scatterers are uniformly distributed over the considered rectangular areas. The L_p -norm method has been applied to optimize the simulation model parameters by using a finite number of scatterers (cisoids). For the simulation model, we use $M \times N = 50 \times 25$ scatterers (cisoids) within the rectangle on the left-hand side as well as on the right-hand side.

In Figure 3, the absolute value of the 2D space CCF $|\rho_{11,22}(\delta_T, \delta_R)|$ of the reference model is presented for the NLOS propagation scenario ($c_R = 0$). The results have been obtained by using (30). From Figure 3, we can observe that the 2D space CCF decreases as the antenna element spacings

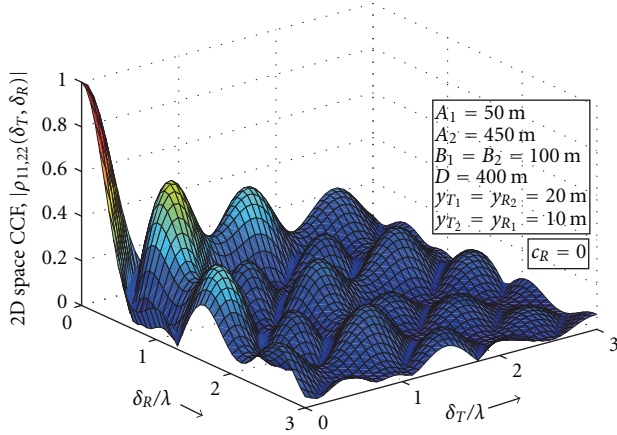


FIGURE 3: Absolute value of the 2D space CCF $|\rho_{11,22}(\delta_T, \delta_R)|$ of the reference model for a NLOS propagation scenario ($c_R = 0$).

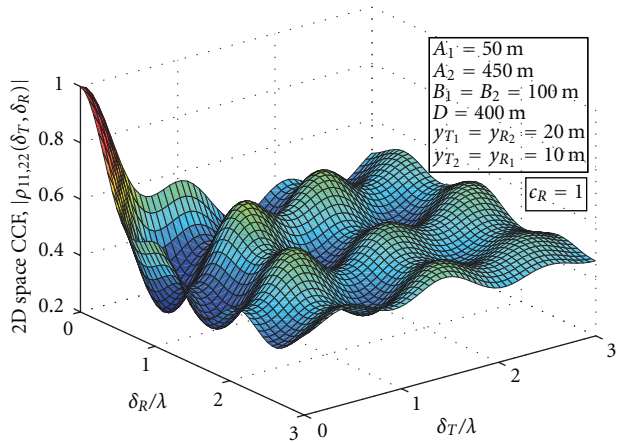


FIGURE 4: Absolute value of the 2D space CCF $|\rho_{11,22}(\delta_T, \delta_R)|$ of the reference model for a LOS propagation scenario ($c_R = 1$).

increase. For comparison reasons, the absolute value of the 2D space CCF $|\rho_{11,22}(\delta_T, \delta_R)|$ is depicted in Figure 4 for a LOS propagation scenario ($c_R = 1$). From Figure 4, one can see that the channel transfer functions $H_{ki}(f', t)$ and $H_{k'T'}(f', t)$ are highly correlated over a large range of antenna element spacings δ_T and δ_R . This can be concluded from the fact that even for large antenna element spacings, for example, $\delta_T = \delta_R = 3\lambda$, the absolute value of the 2D space CCF $|\rho_{11,22}(\delta_T, \delta_R)|$ equals approximately one half of its maximum value. Comparing Figures 3 and 4 shows that by increasing the Rice factor c_R , the 2D space CCF also increases.

Figures 5 and 6 illustrate the TF-CCFs of the reference model under NLOS and LOS propagation conditions, respectively. From Figure 5, we can observe that the TF-CCF decreases as the time and frequency lags increase in NLOS propagation environments. A comparison of Figures 5 and 6 shows that the absolute value of the TF-CCF under LOS conditions is in general higher than under NLOS.

Figure 7 depicts the absolute value of the temporal ACF $|r_{kl}(\tau)|$ according to (32) if both the transmitter and the receiver are moving towards each other. A good match

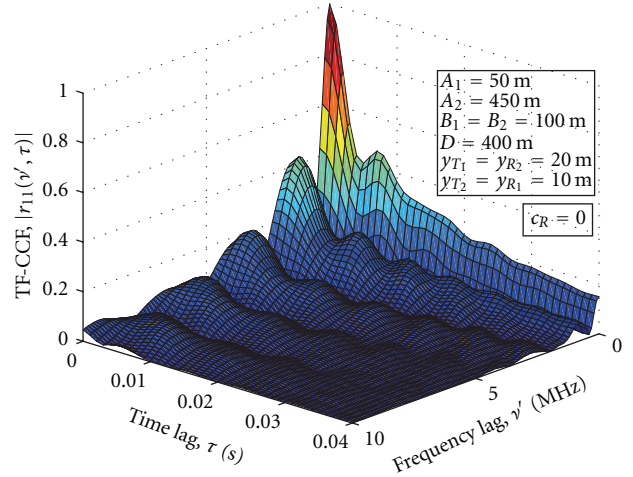


FIGURE 5: Absolute value of the TF-CCF $|r_{11}(\nu', \tau)|$ of the reference model for a NLOS propagation scenario ($c_R = 0$).

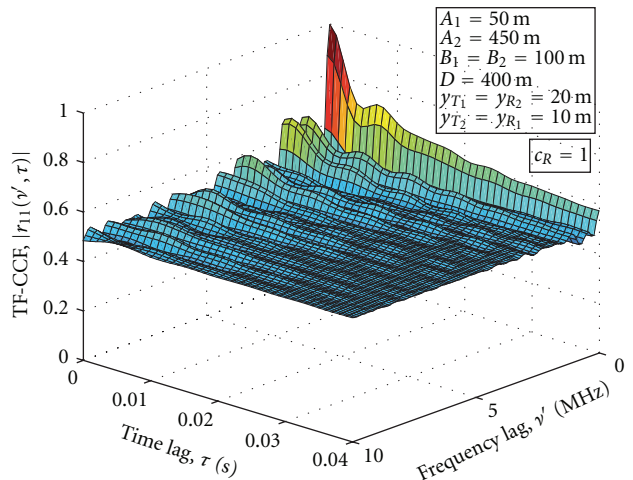


FIGURE 6: Absolute value of the TF-CCF $|r_{11}(\nu', \tau)|$ of the reference model for a LOS propagation scenario ($c_R = 1$).

between the temporal ACF of the reference model and that of the simulation model can be observed in Figure 7. This figure demonstrates also that the experimental simulation results of the temporal ACF match very well with the theoretical results.

Finally, Figure 8 illustrates the absolute value of the FCF $|r_{kl}(\nu')|$ for different Rice factors $c_R = \{0, 0.5, 1\}$ if both the transmitter and the receiver are moving towards each other. A close agreement between the reference model and the simulation model can be seen in Figure 8 for all chosen Rice factors. One can realize that the experimental simulation results of the FCF match very well with the theoretical results.

8. Conclusion

In this paper, a reference model for a wideband MIMO C2C channel has been derived by starting from the geometrical street scattering model. Taking both LOS and NLOS

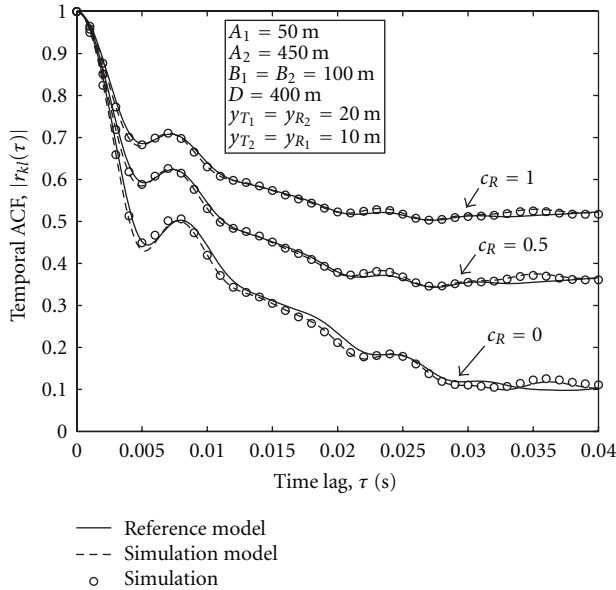


FIGURE 7: Absolute values of the ACFs $|r_{kl}(\tau)|$ (reference model) and $|\hat{r}_{kl}(\tau)|$ (simulation model) for different values of the Rice factor $c_R \in \{0, 0.5, 1\}$.

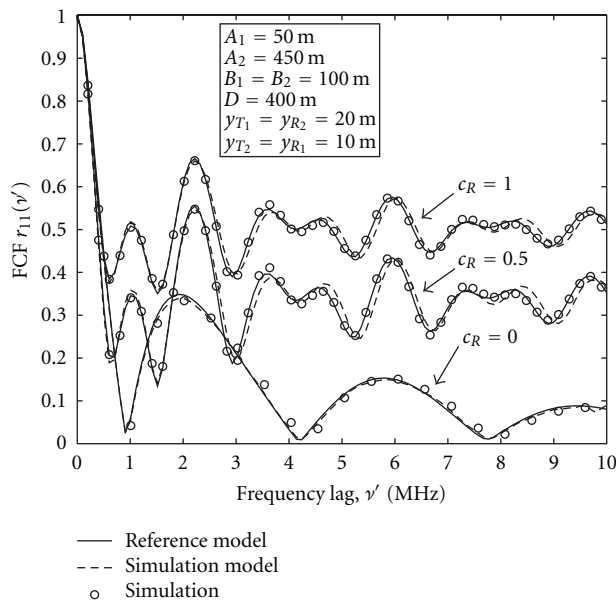


FIGURE 8: Absolute values of the FCFs $|r_{11}(\nu')|$ (reference model) and $|\hat{r}_{11}(\nu')|$ (simulation model) for different values of the Rice factor $c_R \in \{0, 0.5, 1\}$.

propagation conditions into account, we have analyzed the 2D space CCF and the TF-CCF of the reference model. To find a proper simulation model, the SOC principle has been applied. It has been shown that the SOC channel simulator approximates the reference model with high accuracy with respect to the temporal ACF and the FCF. An excellent fitting of the average Doppler shift and the Doppler spread of the reference model to the corresponding quantities of measured channels has validated the usefulness of the

proposed reference model. Further extensions of the proposed wideband MIMO C2C channel model incorporating the nonstationarity properties of real-world C2C channels are planned for future work.

References

- [1] F. Qu, F. Y. Wang, and L. Yang, "Intelligent transportation spaces: vehicles, traffic, communications, and beyond," *IEEE Communications Magazine*, vol. 48, no. 11, pp. 136–142, 2010.
- [2] <http://www.ertico.com/>.
- [3] <http://www.car-to-car.org/>.
- [4] E. Telatar, "Capacity of multi-antenna Gaussian channels," *European Transactions on Telecommunications*, vol. 10, no. 6, pp. 585–595, 1999.
- [5] M. Pätzold, B. O. Hogstad, and N. Youssef, "Modeling, analysis, and simulation of MIMO mobile-to-mobile fading channels," *IEEE Transactions on Wireless Communications*, vol. 7, no. 2, pp. 510–520, 2008.
- [6] M. Pätzold and B. O. Hogstad, "A wideband MIMO channel model derived from the geometric elliptical scattering model," *Wireless Communications and Mobile Computing*, vol. 8, no. 5, pp. 597–605, 2008.
- [7] H. Zhiyi, C. Wei, Z. Wei, M. Pätzold, and A. Chelli, "Modelling of MIMO vehicle-to-vehicle fading channels in T-junction scattering environments," in *Proceedings of the 3rd European Conference on Antennas and Propagation (EuCAP '09)*, pp. 652–656, Berlin, Germany, March 2009.
- [8] A. Chelli and M. Pätzold, "A MIMO mobile-to-mobile channel model derived from a geometric street scattering model," in *Proceedings of the 4th IEEE International Symposium on Wireless Communication Systems (ISWCS '07)*, pp. 792–797, Trondheim, Norway, October 2007.
- [9] N. Avazov and M. Pätzold, "A geometric street scattering channel model for car-to-car communication systems," in *Proceedings of the International Conference on Advanced Technologies for Communications (ATC '11)*, pp. 224–230, Da Nang City, Vietnam, August 2011.
- [10] A. S. Akki and F. Haber, "A statistical model of mobile-to-mobile land communication channel," *IEEE Transactions on Vehicular Technology*, vol. VT-35, no. 1, pp. 2–7, 1986.
- [11] A. S. Akki, "Statistical properties of mobile-to-mobile land communication channels," *IEEE Transactions on Vehicular Technology*, vol. 43, no. 4, pp. 826–831, 1994.
- [12] R. Wang and D. Cox, "Channel modeling for ad hoc mobile wireless networks," in *Proceedings of the 55th IEEE Vehicular Technology Conference (VTC '02)*, vol. 1, pp. 21–25, Birmingham, AL, USA, May 2002.
- [13] C. S. Patel, G. L. Stüber, and T. G. Pratt, "Simulation of Rayleigh-faded mobile-to-mobile communication channels," *IEEE Transactions on Communications*, vol. 53, no. 11, pp. 1876–1884, 2005.
- [14] A. G. Zajić and G. L. Stüber, "Space-time correlated mobile-to-mobile channels: modelling and simulation," *IEEE Transactions on Vehicular Technology*, vol. 57, no. 2, pp. 715–726, 2008.
- [15] X. Cheng, C. X. Wang, D. I. Laurenson, H. H. Ghent, and A. V. Vasilakos, "A generic geometrical-based MIMO mobile-to-mobile channel model," in *Proceedings of the International Wireless Communications and Mobile Computing Conference (IWCMC '08)*, pp. 1000–1005, August 2008.

- [16] "IEEE 802.11p, Part 11: wireless LAN medium access control (MAC) and physical layer (PHY) specifications amendment 6: wireless access in vehicular environments, IEEE standards association," June 2010.
- [17] "Standard specification for telecommunications and information exchange between roadside and vehicle systems—5 GHz band dedicated short range communications (DSRC) medium access control (MAC) and physical layer (PHY) specifications," ASTM E2213-03, September 2003.
- [18] G. Acosta, K. Tokuda, and M. A. Ingram, "Measured joint Doppler-delay power profiles for vehicle-to-vehicle communications at 2.4 GHz," in *Proceedings of IEEE Global Telecommunications Conference (GLOBECOM '04)*, pp. 3813–3817, Dallas, Tex, USA, December 2004.
- [19] P. C. F. Eggers, T. W. C. Brown, K. Olesen, and G. F. Pedersen, "Assessment of capacity support and scattering in experimental high speed vehicle-to-vehicle MIMO links," in *Proceedings of the IEEE 65th Vehicular Technology Conference (VTC '07)*, pp. 466–470, April 2007.
- [20] I. Sen and D. W. Matolak, "Vehicle-to-vehicle channel models for the 5-GHz band," *IEEE Transactions on Intelligent Transportation Systems*, vol. 9, no. 2, pp. 235–245, 2008.
- [21] Q. Wu, D. W. Matolak, and I. Sen, "5-GHz-band vehicle-to-vehicle channels: models for multiple values of channel bandwidth," *IEEE Transactions on Vehicular Technology*, vol. 59, no. 5, pp. 2620–2625, 2010.
- [22] J. Maurer, T. Fügen, and W. Wiesbeck, "Narrow-band measurement and analysis of the inter-vehicle transmission channel at 5.2 GHz," in *Proceedings of the 55th Vehicular Technology Conference (VTC '02)*, vol. 3, pp. 1274–1278, May 2002.
- [23] L. Cheng, B. E. Henty, D. D. Stancil, F. Bai, and P. Mudalige, "Mobile vehicle-to-vehicle narrow-band channel measurement and characterization of the 5.9 GHz dedicated short range communication (DSRC) frequency band," *IEEE Journal on Selected Areas in Communications*, vol. 25, no. 8, pp. 1501–1516, 2007.
- [24] A. Paier, J. Karedal, N. Czink, H. Hofstetter, and C. Dumard, "Car-to-car radio channel measurements at 5 GHz: pathloss, power-delay profile, and delay-Doppler spectrum," in *Proceedings of the 4th IEEE International Symposium on Wireless Communication Systems (ISWCS '07)*, pp. 224–228, Trondheim, Norway, October 2007.
- [25] I. Tan, W. Tang, K. Laberteaux, and A. Bahai, "Measurement and analysis of wireless channel impairments in DSRC vehicular communications," in *Proceedings of IEEE International Conference on Communications (ICC '08)*, pp. 4882–4888, May 2008.
- [26] J. Kunisch and J. Pamp, "Wideband car-to-car radio channel measurements and model at 5.9 GHz," in *Proceedings of the 68th IEEE Vehicular Technology (VTC '08)*, pp. 1–5, September 2008.
- [27] O. Renaudin, V. M. Kolmonen, P. Vainikainen, and C. Oestges, "Wideband measurement-based modeling of inter-vehicle channels in the 5 GHz band," in *Proceedings of the 5th European Conference on Antennas and Propagation (EUCAP '11)*, pp. 2881–2885, April 2011.
- [28] A. Chelli and M. Pätzold, "A wideband multiple-cluster MIMO mobile-to-mobile channel model based on the geometrical street model," in *Proceedings of IEEE 19th International Symposium on Personal, Indoor and Mobile Radio Communications (PIMRC '08)*, pp. 1–6, Cannes, France, September 2008.
- [29] A. G. Zajić, G. L. Stüber, T. G. Pratt, and S. T. Nguyen, "Wideband MIMO mobile-to-mobile channels: geometry-based statistical modeling with experimental verification," *IEEE Transactions on Vehicular Technology*, vol. 58, no. 2, pp. 517–534, 2009.
- [30] X. Cheng, C. X. Wang, D. I. Laurenson, S. Salous, and A. V. Vasilakos, "An adaptive geometry-based stochastic model for non-isotropic MIMO mobile-to-mobile channels," *IEEE Transactions on Wireless Communications*, vol. 8, no. 9, pp. 4824–4835, 2009.
- [31] G. D. Durgin, *Space-Time Wireless Channels*, Prentice Hall, 2002.
- [32] S. H. Kong, "TOA and AOD statistics for down link Gaussian scatterer distribution model," *IEEE Transactions on Wireless Communications*, vol. 8, no. 5, pp. 2609–2617, 2009.
- [33] Y. Ma and M. Pätzold, "A wideband one-ring MIMO channel model under non-isotropic scattering conditions," in *Proceedings of IEEE 67th Vehicular Technology Conference (VTC '08)*, pp. 424–429, Singapore, May 2008.
- [34] F. Vatalaro, "Doppler spectrum in mobile-to-mobile communications in the presence of three-dimensional multipath scattering," *IEEE Transactions on Vehicular Technology*, vol. 46, no. 1, pp. 213–219, 1997.
- [35] M. Pätzold, *Mobile Radio Channels*, John Wiley & Sons, Chichester, UK, 2nd edition, 2011.
- [36] A. Papoulis and S. U. Pillai, *Probability, Random Variables and Stochastic Processes*, McGraw-Hill, New York, NY, USA, 4th edition, 2002.
- [37] M. Pätzold and B. Talha, "On the statistical properties of sum-of-cisoids-based mobile radio channel simulators," in *Proceedings of the 10th International Symposium on Wireless Personal Multimedia Communications (WPMC '07)*, pp. 394–400, Jaipur, India, December 2007.
- [38] C. A. Gutiérrez and M. Pätzold, "The design of sum-of-cisoids Rayleigh fading channel simulators assuming non-isotropic scattering conditions," *IEEE Transactions on Wireless Communications*, vol. 9, no. 4, pp. 1308–1314, 2010.

Research Article

A Three-Dimensional Geometry-Based Statistical Model of 2×2 Dual-Polarized MIMO Mobile-to-Mobile Wideband Channels

Jun Chen and Thomas G. Pratt

Department of Electrical Engineering, University of Notre Dame, Notre Dame, IN 46556, USA

Correspondence should be addressed to Thomas G. Pratt, tpratt@nd.edu

Received 27 April 2012; Accepted 27 July 2012

Academic Editor: Carlos A. Gutierrez

Copyright © 2012 J. Chen and T. G. Pratt. This is an open access article distributed under the Creative Commons Attribution License, which permits unrestricted use, distribution, and reproduction in any medium, provided the original work is properly cited.

A three-dimensional (3D) model for wide-band dual-polarized (DP) multiple-input-multiple-output (MIMO) mobile-to-mobile (M2M) channels is proposed. Using geometrical scattering based on concentric spheres at the transmitter (Tx) and at the receiver (Rx), a 3D parametric reference model for 2×2 M2M DP multipath fading channels is developed. The channel model assumes the use of colocated half-wavelength dipole antennas for vertical and horizontal polarizations at both transmit and receive stations. Model parameters include the velocities of the Tx and Rx nodes, the distance between the nodes, the 3D antenna pattern gains, the azimuth and elevation angles of arrival and departure, the geometrical distribution of the scatterers, the Rician K-factors defining the fading envelope distributions, the maximum Doppler frequency, the scattering loss factors, the cross-polar power discrimination ratio (XPD), and the copolarization power ratio (CPR). Using the proposed model, expressions for joint time-frequency correlation functions (TFCFs) are derived which are used to investigate system behavior over different wide sense stationary uncorrelated scattering (WSSUS) channel realizations. The numerical results illustrate the sensitivities of the TFCF to simultaneous time and frequency offsets for the 2×2 DP-MIMO architectures.

1. Introduction

For nearly two decades, multiple-input-multiple-output (MIMO) communications systems [1–3] have been rigorously studied, leading to the adoption of MIMO in a number of wireless communications standards such as Long Term Evolution (LTE) and 802.11n. The LTE provides high-speed wireless communications for mobile phones and data terminals, while 802.11n supports MIMO, frame aggregation, and security improvements for wireless local area networks (WLAN). In these systems, multiple antennas can be used at both the transmitter (Tx) and receiver (Rx) to exploit the diversity and channel capacity afforded by MIMO architectures. In array-based MIMO systems, CP antennas at mobile stations and access points are ideally separated by at least one-half wavelength and at cellular base stations by at least ten wavelengths to achieve significant diversity or multiplexing gains [4]. In space-constrained implementations such as with handheld devices, use of antenna spacings less than one-half wavelength can lead to

antenna correlations that lend themselves to beamforming gains, but ohmic coupling effects can deplete any gains that would otherwise be achieved with these strategies [5]. An alternative architecture for space-constrained deployments involves the use of dual-polarized (DP) antennas. This strategy has the advantage of offering colocated antennas that provide largely uncorrelated fading responses, although usually with asymmetrical average powers among the MIMO channel matrix entries. Hence, the channel behaviors for DP systems are substantively different from conventional copolarized (CP) channels, the latter which exhibit similar average powers. The relative performance of DP-MIMO in comparison to traditional MIMO with CP arrays will be dictated by the disparities in these responses. While DP architectures are receiving increasing attention, they have thus far been studied with much less rigor than CP systems.

To characterize DP systems, especially in wideband signaling applications, modeling of dispersive input-to-output polarimetric channel behavior is important. Many

theoretical models [6–11] provide statistical representations of polarimetric channels based on cross-polarization coupling (XPC), but do not characterize polarization-frequency behavior that is needed to represent wideband, frequency-selective channels for the analysis of DP communications systems. For example, XPC is most often analyzed in the narrowband sense and yet it has been shown that the XPC can vary with frequency. It also exhibits correlation in the frequency dimension in a manner that depends on the channel's temporal dispersion properties and polarization coupling [12]. Statistical channel models in literature that address time-selective and frequency-selective behavior often assume that the time dispersion (due to time delays) and the frequency dispersion (due to Doppler spread) are statistically independent, where the time delays depend on the relative locations of the random scatterers and the Doppler spreads depend on the motion of the Tx and Rx antennas [13, 14]. However, this assumption is broken if both the time delays and the Doppler spreads depend on the relative location of the random scatterers (e.g., the angles of departure and the angles of arrivals). Because these phenomena would not be expected to be statistically independent, it is of interest to examine joint correlation functions in time and frequency, which is an application of the model that we consider in our paper.

Analytical approaches such as Kronecker or eigenbeam models have also been used for model simulations, and these have dealt with narrowband channels. An analytical framework based on a Kronecker model is presented in [15] to model narrowband DP Rayleigh and Rician fading channels for arbitrary array sizes. The framework uses a relatively small number of physical parameters to analyze the benefits of multiple polarization architectures. In other work, a 3D polarized narrowband spatial channel model is presented in [7], and the impact of elevation angle on capacity is reported in [16]. These models assume ideal dipole antennas and unity cross-polar discrimination ratios.

Another approach to characterize channels for DP systems involves the use of geometric scattering models. Geometrical scattering models [17–19] have the advantage that they are able to represent important channel behaviors, including mutual effects that arise from polarization coupling, time-dispersion, angle-dispersion, and frequency-dispersion. However, they also are more complex. Early two-dimensional (2D) geometric scattering models were developed for narrowband CP single-input single-output (SISO) mobile-to-mobile (M2M) Rayleigh fading channels [20–22]. In [23], the polarisation-sensitive geometric modelling is developed with a direction-of-arrival (DOA) distribution that depends on the polarisation states of the transmitting antennas, the receiving antennas and the polarisation properties of the scatterers. These models were 2D in the sense that the models treated electromagnetic propagation only in a fixed-elevation plane and did not model elevation antenna pattern dependencies or distributions of scatterers in the elevation dimension.

Some three-dimensional (3D) models have been proposed to overcome shortcomings of 2D M2M channel models, particularly in environments where deployed antenna

heights are lower than surrounding buildings and obstacles. In [18], a 3D wideband M2M mathematical reference model was proposed based on a concentric-cylinders geometry using a superposition of line-of-sight (LOS), single bounce at the transmit side (SBT), single bounce at the receive side (SBR), and double-bounce (DB) rays in a variety of urban environments. The analysis approach proved useful to characterize M2M correlations, but to date has only been applied to the analysis of CP MIMO channels with unity-gain idealized dipole antennas. Recently, a 3D polarized channel model has been proposed to treat spatially-separated orthogonally polarized elements [19]. The model deals exclusively with the double-bounce ray and narrowband channels.

In this paper, we develop a 3D geometric scattering model for 2×2 M2M DP wideband channels based on concentric spheres to evaluate joint time frequency correlation functions associated with the subchannel fading envelopes. The use of concentric spheres is motivated by the ease with which scatterer locations may be identified for a given radius, azimuth AOD, and elevation AOD, and by its capability to support the modeling of overhead reflectors. The DP-MIMO channel is constructed assuming a DP antenna at both the Tx and the Rx, where the polarization basis at the Rx is matched to the polarization basis used at the Tx. The received signals can be translated to an arbitrary orthogonally-polarized basis by applying a unitary transformation to the received signal vectors [24] without impacting theoretical performance measures such as capacity and diversity.

We assume a channel with wide sense stationary uncorrelated scattering (WSSUS) where the channel correlation function is invariant over time, and the scatterers with different path delays are uncorrelated [25, 26]. Channel transfer functions for each transmit antenna/receive antenna pair are derived as a superposition of LOS, SBT, SBR, and DB component rays. The transfer functions are used to form time-frequency correlation functions (TFCF) for the assumed 3D nonisotropic scattering environment, where scattering distributions are characterized in the azimuth dimension through the von Mises distribution and in the elevation dimension by a cosine distribution. The 3D scattering propagation model used to evaluate the TFCFs simulates the effects of the antenna pattern gains, the geometrical distribution of scatterers and the associated azimuth/elevation angles of arrival and departure, the K-factor of the fading distributions, the maximum Doppler frequency, the scattering loss factors, the cross-polar discrimination (XPD), and the copolarization ratio (CPR).

The remainder of the paper is organized as follows. The 3D DP 2×2 MIMO M2M model is presented in Section 2. In Section 3, we derive transfer functions and TFCFs for each subchannel of the DP-MIMO channel and for each ray path type for 3D nonisotropic scattering environments. Numerical results of the joint correlation functions associated with the 2×2 DP channel models are presented in Section 4. We conclude with a summary of our findings in Section 5.

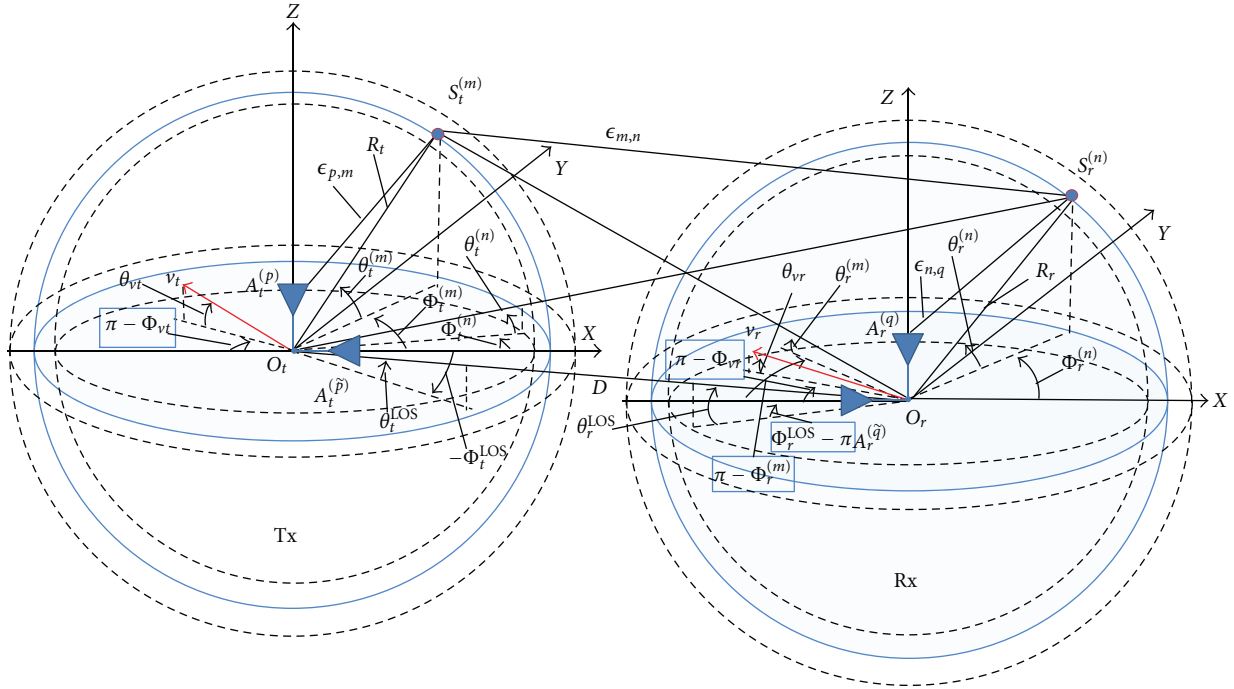


FIGURE 1: Concentric-spheres for 3D collocated DP channel model. The signals from the Tx antennas arrive in parallel at the Rx antenna array.

2. 2×2 DP-MIMO Channel Model Based on Concentric Spheres

The concentric sphere geometry-based scattering model assumes a mobile Tx and a mobile Rx, both equipped with DP antennas using a matched polarization basis. Radio propagation between the Tx and the Rx is characterized by 3D WSSUS under channels that can include line-of-sight (LOS) and non-line-of-sight (NLOS) components, where scattering centers in the latter case reside on concentric spheres about either the Tx, the Rx, or both. The linearly time-variant MIMO channel can be represented by a 2×2 impulse response matrix in terms of time t and delay τ

$$\mathbf{H}(t, \tau) = \begin{bmatrix} h_{qp}(t, \tau) & h_{q\bar{p}}(t, \tau) \\ h_{\bar{q}p}(t, \tau) & h_{\bar{q}\bar{p}}(t, \tau) \end{bmatrix}. \quad (1)$$

Figure 1 illustrates the concentric sphere model for a MIMO M2M channel with DP antennas. One DP antenna with vertically-polarized and horizontally-polarized components denoted by $A_t^{(p)}$ and $A_t^{(\bar{p})}$, respectively, is located at the center of the Tx sphere (O_t). A second DP antenna with corresponding components denoted by $A_r^{(q)}$ and $A_r^{(\bar{q})}$ is located at the center of the Rx sphere (O_r). At the Tx, M fixed scatterers reside within the volume of a sphere defined by a radius R_t . The m th transmit scatterer is denoted by $S_t^{(m)}$, where $1 \leq m \leq M$ and resides on the surface of a sphere with radius R_m , where $R_m < R_t$. Similarly at the Rx, N scatterers occupy the spherical volume with a radius R_r . The n th receive scatterer is denoted by $S_r^{(n)}$, where $1 \leq n \leq N$ and resides on the surface of a sphere with radius R_n , where $R_n < R_r$.

The set of scatterers is comprised of H scatterers (reflecting horizontally polarized waves) and V scatterers (reflecting vertical polarized waves). We assume that the distribution of the H scatterers and the V scatterers are identical and that the number of scatterers for each are the same, although this may not be true in general.

The center of the Tx sphere serves as the global origin of a rectangular coordinate system. At time $t = 0$, the Rx is a distance D from the Tx with XYZ coordinates denoted by $(\Delta_x, \Delta_y, \Delta_z)$. The height difference between the Tx and the Rx antennas is included in the offset Δ_z . The symbols $\epsilon_{p,m}$, $\epsilon_{m,q}$, $\epsilon_{p,n}$, $\epsilon_{n,q}$, $\epsilon_{m,n}$ and $\epsilon_{p,q}$ denote distances $d(A_t^{(p)}, S_t^{(m)})$, $d(S_t^{(m)}, A_r^{(q)})$, $d(A_t^{(p)}, S_r^{(n)})$, $d(S_r^{(n)}, A_r^{(q)})$, $d(S_t^{(m)}, S_r^{(n)})$, and $d(A_t^{(p)}, A_r^{(q)})$, respectively, where $d(\cdot)$ denotes the distance between the two coordinates. The symbols $\theta_t^{(m)}$, $\theta_t^{(n)}$ are the elevation angles of departure (EAoD, relative to the XY plane) to the scatterers $S_t^{(m)}$ and $S_r^{(n)}$, respectively, whereas $\phi_t^{(m)}$, $\phi_t^{(n)}$ are the azimuth angles of departure (AAoD, in the XY plane relative to the Z -axis) to the scatterers $S_t^{(m)}$ and $S_r^{(n)}$ respectively. Similarly, the symbols $\theta_r^{(m)}$, $\theta_r^{(n)}$ denote the elevation angles of arrival (EAoA, relative to the x - y plane) reflected from the scatterers $S_t^{(m)}$ and $S_r^{(n)}$, respectively, whereas $\phi_r^{(m)}$, $\phi_r^{(n)}$ denote the azimuth angles of arrival (AAoA, in the XY plane relative to the z -axis) reflected from the scatterers $S_t^{(m)}$ and $S_r^{(n)}$ respectively. For the LOS component between the Tx and the Rx, the symbols θ_r^{LOS} and ϕ_r^{LOS} are the elevation angle of departure (relative to the XY plane) and the azimuth angle of departure in the XY plane relative to the Z -axis, respectively. Similarly, the symbols θ_r^{LOS}

and ϕ_r^{LOS} are the elevation angle of arrival and the azimuth angle of arrival, respectively. The Tx and Rx are moving with speeds v_t and v_r in directions described by the elevation angles θ_{vt} and θ_{vr} relative to the XY plane, respectively, and by the azimuth angles ϕ_{vt} and ϕ_{vr} in the XY plane, respectively.

2.1. Scatterer Distributions. The directions of scatterers are described by azimuth and elevation angle distributions. Several different distributions, such as uniform, Gaussian, Laplacian, and von Mises, have been used in the literature to characterize the azimuth angles of departure and arrival. von Mises Fisher (VMF) distributions are effective to model both AAoD and AAoA for spatial fading correlation models [27] and have the advantage that the probability density function approximates many of distributions and admits closed-form solutions [18]. To simplify the modeling, it is assumed that the azimuth and elevation angles are independent, enabling the use of a product of distribution functions instead of a joint distribution. The scatterer distributions are synthesized using different angle distributions for the azimuth and the elevation dimensions. The Von Mises Fisher probability density function (pdf) distribution is used for azimuth dimensions, including for angles of departure ($\phi_t^{(m)}$ and $\phi_r^{(n)}$) and angles of arrival ($\phi_t^{(n)}$ and $\phi_r^{(m)}$). The von Mises pdf is defined as [28]

$$f(\phi) = \frac{\exp[\kappa \cos(\phi - \mu)]}{2\pi I_0(\kappa)}, \quad \phi \in [-\pi, \pi), \quad (2)$$

where $\mu \in [-\pi, \pi)$ is the mean value of the scatterer directions in the azimuth plane, κ controls the spread of scatterers around the mean μ , and $I_0(\cdot)$ is the zero-order modified Bessel function of the first kind. When $\kappa = 0$, $f(\phi) = 1/2\pi$ is a uniform distribution, corresponding to isotropic scattering in azimuth. As κ increases, the scatterers become more clustered about the mean angle μ , and scattering is nonisotropic.

The random elevation angles of departure and arrival can be characterized by a uniform, cosine or Gaussian distribution. In [18, 29], a cosine pdf is used as it may fit with the typical propagation in M2M communications, where the Tx and Rx are in motion and equipped with low elevation antennas. A cosine distribution employed for the elevation angles of departure and arrival is given by [29]:

$$f(\theta) = \begin{cases} \frac{\pi}{4|\theta_{\max}|} \cos\left(\frac{\pi}{2} \frac{\theta}{\theta_{\max}}\right), & |\theta| \leq |\theta_{\max}| \leq \frac{\pi}{2}, \\ 0, & \text{otherwise.} \end{cases} \quad (3)$$

where θ_{\max} is the maximum elevation angle which we assume to have a value near 20° . This maximum elevation angle is typical of M2M wireless communications where both the Tx and Rx are equipped with low elevation antennas.

The above-mentioned distributions are used to represent the response from a cluster, which describes a group of scatterers located within an isolated solid angle, and the response from multiple clusters compose the aggregate response from

the channel. In [27], a mixture of Von Mises distributions is proposed for modeling the 3D direction of scatterers in the presence of multiple clusters of scatterers over the propagation channel. Mathematically, each distribution in the mixture of M VMFs at the Tx or N VMFs at the Rx can be described as $f(\phi_t^{(m)} | \bar{\phi}_t^{(m)}, \kappa_m)$ ($1 \leq m \leq M$) or $f(\phi_r^{(n)} | \bar{\phi}_r^{(n)}, \kappa_n)$ ($1 \leq n \leq N$). Note that $\bar{\phi}_t^{(m)}$ or $\bar{\phi}_r^{(n)}$ is the mean azimuth angle of the m th or n th cluster; κ_m or κ_n is the concentration of the m th or n th cluster. Hence, the overall density functions of the mixture model consisting of M VMF distributions for the cluster azimuth angles $\phi_t^{(m)}$ at the transmitter and N VMF distributions for the cluster azimuth angles $\phi_r^{(n)}$ at the Rx can be described as [27]

$$\bar{f}(\phi_t) = \sum_{m=1}^M \nu_m \left(f(\phi_t^{(m)} | \bar{\phi}_t^{(m)}, \kappa_m) \right), \quad (4)$$

$$\bar{f}(\phi_r) = \sum_{n=1}^N \nu_n \left(f(\phi_r^{(n)} | \bar{\phi}_r^{(n)}, \kappa_n) \right),$$

where M and N the number of clusters at the Tx and Rx, respectively; ν_m or ν_n is defined as the *a priori* probability that m th or n th cluster was generated. Similarly, the overall density functions of the mixture model consisting of the cosine distributions for the elevation angles $\theta_t^{(m)}$ at the Tx and $\theta_r^{(n)}$ at the Rx can be expressed as

$$\bar{f}(\theta_t) = \sum_{m=1}^M \nu_m \left(\theta_t^{(m)} | \bar{\theta}_t^{(m)} \right), \quad (5)$$

$$\bar{f}(\theta_r) = \sum_{n=1}^N \nu_n \left(\theta_r^{(n)} | \bar{\theta}_r^{(n)} \right),$$

where $\bar{\theta}_t^{(m)}$ and $\bar{\theta}_r^{(n)}$ are the mean elevation angle of the m th or n th cluster at the Tx and Rx, respectively.

Signals from the Tx antenna elements that propagate directly to the Rx antenna elements form the LOS component. Signals reflected exclusively from the scatterers located around the Tx before arriving at the Rx antenna elements are collectively called the SBT component. Similarly, transmit signals reflected only by scatterers located around the Rx before arriving at the Rx antenna elements form the SBR component. The DB component is formed from the signals that are reflected from scatterers about both the Tx and the Rx before arriving at the Rx antenna elements. For each realization of the WSSUS channel, the channel impulse responses and TFCFs can be written as superpositions of the LOS, SBT, SBR, and DB signal components.

The channel impulse responses for the subchannels $A_t^{(p)} \rightarrow A_r^{(q)}$, $A_t^{(\hat{p})} \rightarrow A_r^{(q)}$, $A_t^{(p)} \rightarrow A_r^{(\hat{q})}$ and $A_t^{(\hat{p})} \rightarrow A_r^{(\hat{q})}$ can be written as a superposition of the LOS, SBT, SBR and DB signals,

$$h_{ab}(t, \tau) = h_{ab}^{\text{SBR}}(t, \tau) + h_{ab}^{\text{SBR}}(t, \tau) + h_{ab}^{\text{DB}}(t, \tau) + h_{ab}^{\text{LOS}}(t, \tau), \quad (6)$$

where the $h_{ab}^l(t, \tau)$ ($a \in \{p, \tilde{p}\}, b \in \{q, \tilde{q}\}, l \in \{\text{LOS}, \text{SBT}, \text{SBR}, \text{DB}\}$) represent the impulse response functions between antenna elements a and b along the l path respectively, and $h_{ab}(t, \tau)$ represents the total response between antenna elements a and b .

2.2. Single Bounce Channel Impulse Response. The time varying impulse responses of the single-bounce components are given by

$$\begin{aligned}
 h_{ab}^{\text{SBT}}(t, \tau) &= \sqrt{\frac{\eta_{t,pq}}{K+1}} \frac{1}{\sqrt{N}} \sum_{n=1}^M \xi_{a,n,b} g_{a,n,b}(t) \\
 &\times \delta(\tau - \tau_{a,m,b}) \\
 &\times \left[\sqrt{G_a^{(v)}(\phi_t^{(m)}, \theta_t^{(m)})} \sqrt{G_a^{(h)}(\phi_t^{(m)}, \theta_t^{(m)})} \right] \\
 &\times \begin{bmatrix} 1 & \sqrt{r_{p\tilde{q}}^{(m)}} \\ \sqrt{r_{\tilde{p}q}^{(m)}} & 1 \end{bmatrix} \begin{bmatrix} \sqrt{G_b^{(v)}(\phi_r^{(m)}, \theta_r^{(m)})} \\ \sqrt{G_b^{(h)}(\phi_r^{(m)}, \theta_r^{(m)})} \end{bmatrix} \\
 &\times \exp(j\phi_{ab}^{(m)}) \rho_m^{\text{SBT}}, \\
 h_{ab}^{\text{SBR}}(t, \tau) &= \sqrt{\frac{\eta_{t,pq}}{K+1}} \frac{1}{\sqrt{N}} \sum_{n=1}^M \xi_{a,n,b} g_{a,n,b}(t) \\
 &\times \delta(\tau - \tau_{a,n,b}) \\
 &\times \left[\sqrt{G_a^{(v)}(\phi_t^{(n)}, \theta_t^{(n)})} \sqrt{G_a^{(h)}(\phi_t^{(n)}, \theta_t^{(n)})} \right] \\
 &\times \begin{bmatrix} 1 & \sqrt{r_{p\tilde{q}}^{(n)}} \\ \sqrt{r_{\tilde{p}q}^{(n)}} & 1 \end{bmatrix} \begin{bmatrix} \sqrt{G_b^{(v)}(\phi_r^{(n)}, \theta_r^{(n)})} \\ \sqrt{G_b^{(h)}(\phi_r^{(n)}, \theta_r^{(n)})} \end{bmatrix} \\
 &\times \exp(j\phi_{ab}^{(n)}) \rho_n^{\text{SBR}},
 \end{aligned} \tag{7}$$

where the parameter K is the Rician K factor which is a ratio of the power through the LOS path relative to the power through the scattered paths. The power ratio coefficients $\eta_{t,ab}$ and $\eta_{r,ab}$ ($a \in \{p, \tilde{p}\}, b \in \{q, \tilde{q}\}$) in (7) specify the fraction of the power of the single-bounce components along the subchannels $A_t^{(a)} \rightarrow A_r^{(b)}$ with respect to the average transmit power P_{ab} between the Tx antenna element a and the Rx antenna element b . The relationships among these, and related power ratio coefficients are shown in (29). $\xi_{a,m,b}$ and $\xi_{a,n,b}$ denote the signal amplitudes and $\tau_{a,m,b}$ and $\tau_{a,n,b}$ denote time delays of the multipath components propagating from antenna element a to antenna element b via transmit scatterer m and from antenna element a to antenna element b via receive scatterer n ($a \in \{p, \tilde{p}\}, b \in \{q, \tilde{q}\}$), respectively.

$G_a^{(v)}(\cdot, \cdot)$, $G_a^{(h)}(\cdot, \cdot)$, $G_b^{(v)}(\cdot, \cdot)$, and $G_b^{(h)}(\cdot, \cdot)$ ($a \in \{p, \tilde{p}\}, b \in \{q, \tilde{q}\}$) denote the antenna patterns of the p th, \tilde{p} th, q th, and \tilde{q} th antenna element with vertical(v) or horizontal(h) polarizations, respectively. We assume that a half-wavelength dipole is used for each element where the spherical coordinate system defining antenna orientations are illustrated in Figure 2. The antenna feed is situated at

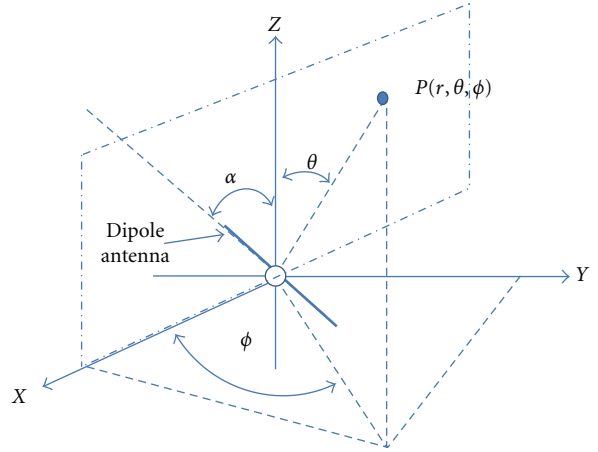


FIGURE 2: Half-wavelength dipole antenna and its coordinate system.

the origin of the coordinate system and the antenna elements are inclined at the angle α from the Z axis in the vertical ZX plane. A thin dipole is assumed and the element radius is ignored. The radiation power gain patterns of the half-wavelength dipole for vertical and horizontal polarizations are given by [30]

$$\begin{aligned}
 G^{(v)}(\theta, \phi) &= 1.641 (\cos \theta \cos \phi \sin \alpha - \sin \theta \cos \alpha)^2 \frac{\cos^2(\pi\zeta/2)}{(1 - \zeta^2)^2}, \\
 G^{(h)}(\theta, \phi) &= 1.641 \sin^2 \phi \sin^2 \alpha \frac{\cos^2(\pi\zeta/2)}{(1 - \zeta^2)^2},
 \end{aligned} \tag{8}$$

where

$$\zeta = \sin \theta \cos \phi \sin \alpha + \cos \theta \cos \alpha. \tag{9}$$

For illustration, antenna gain patterns of the half-wavelength dipole with inclination angles of 0 and $\pi/2$ are shown in Figures 3 and 4 respectively.

$\tau_{a,m,b}$ and $\tau_{a,n,b}$ denote time delays of the multipath components propagating from antenna element $A_t^{(a)}$ to antenna element $A_r^{(b)}$ via the scatterer $S_t^{(m)}$ and from antenna element $A_t^{(a)}$ to antenna element $A_r^{(b)}$ via the scatterer $S_r^{(n)}$, respectively. $g_{a,m,b}(t)$ and $g_{a,n,b}(t)$ are the time-varying phase functions along the path $A_t^{(a)} \rightarrow S_t^{(m)} \rightarrow A_r^{(b)}$ and $a \rightarrow S_r^{(n)} \rightarrow b$, respectively. Since the antenna elements are collocated and share a common phase center, the time delays $\tau_{a,m,b}$ or $\tau_{a,n,b}$ are equivalent between antennas elements $A_t^{(a)}$ and $A_r^{(b)}$, that is,

$$\begin{aligned}
 \tau_{p,m,q} &= \tau_{p,m,\tilde{q}} = \tau_{\tilde{p},m,q} = \tau_{\tilde{p},m,\tilde{q}}, \\
 \tau_{p,n,q} &= \tau_{p,n,\tilde{q}} = \tau_{\tilde{p},n,q} = \tau_{\tilde{p},n,\tilde{q}}.
 \end{aligned} \tag{10}$$

Similarly, $g_{a,m,b}(t)$ and $g_{a,n,b}(t)$ satisfy

$$\begin{aligned}
 g_{p,m,q}(t) &= g_{p,m,\tilde{q}}(t) = g_{\tilde{p},m,q}(t) = g_{\tilde{p},m,\tilde{q}}(t), \\
 g_{p,n,q}(t) &= g_{p,n,\tilde{q}}(t) = g_{\tilde{p},n,q}(t) = g_{\tilde{p},n,\tilde{q}}(t).
 \end{aligned} \tag{11}$$

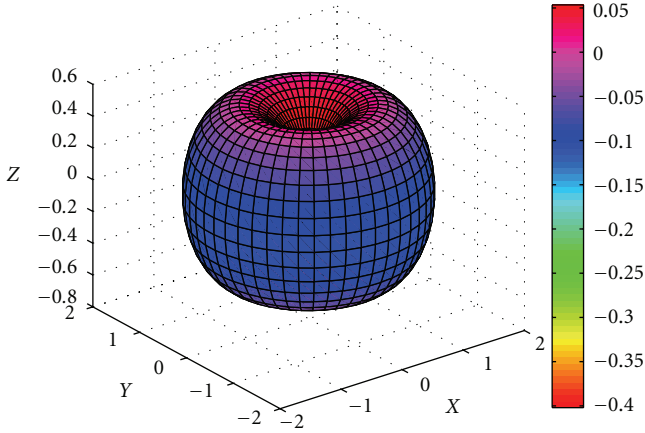


FIGURE 3: Gain patterns of half-wavelength dipole antenna with inclination angle of 0: $G^{(v)}(\theta, \phi)$. The horizontal component $G^{(h)}(\theta, \phi)$ is zero.

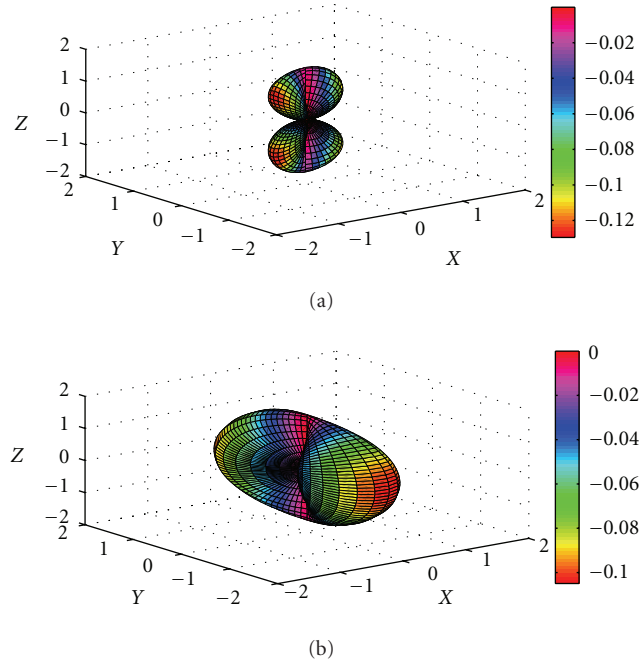


FIGURE 4: Gain patterns of half-wavelength dipole antenna with inclination angle of $\pi/2$: (a) $G^{(v)}(\theta, \phi)$, and (b) $G^{(h)}(\theta, \phi)$.

The random variable $\phi_{ab}^{(m)}$ represents the uniformly-distributed random phase offset associated with the path to each scatterer $S_t^{(m)}$ between the V or H component of the Tx antenna elements and the V or H component of the Rx antenna elements. Similarly, the random variable $\phi_{ab}^{(n)}$ is the uniformly-distributed phase offset associated with the path to each scatterer $S_r^{(n)}$ between the V or H component of the Tx antenna elements and the V or H component of the Rx antenna elements.

$r_{\tilde{p}q}^{(m)}$, $r_{p\tilde{q}}^{(n)}$, $r_{\tilde{p}q}^{(n)}$, and $r_{p\tilde{q}}^{(m)}$ represent the inverse of the channel cross-polar discrimination ratios along the single bounce path to scatterer m or scatterer n , and have statistical means that follow

$$\begin{aligned} E\{r_{p\tilde{q}}^{(m)}\} &= E\{r_{p\tilde{q}}^{(n)}\} = \frac{1}{\text{XPD}_p}, \\ E\{r_{\tilde{p}q}^{(m)}\} &= E\{r_{\tilde{p}q}^{(n)}\} = \frac{1}{\text{XPD}_{\tilde{p}}}. \end{aligned} \quad (12)$$

Here, the channel cross-polar discrimination for each transmit polarization is defined as

$$\begin{aligned} \text{XPD}_p &= \frac{E\{|h_{qp}|^2\}}{E\{|h_{\tilde{q}p}|^2\}}, \\ \text{XPD}_{\tilde{p}} &= \frac{E\{|h_{\tilde{q}\tilde{p}}|^2\}}{E\{|h_{q\tilde{p}}|^2\}}, \end{aligned} \quad (13)$$

where $E\{\cdot\}$ denotes the expectation operator.

The XPD depends on channel parameters and the environment, such as the distance between the Tx and the Rx, the angles of arrival and departure (both azimuth and elevation), the delay spread of the multipath components, and the transmit and receive antenna polarization basis.

We define a parameter $\text{CPR}_{qp,\tilde{q}\tilde{p}}$ as the copolar power ratio between the average powers transmitted through the vertical-vertical subchannel and the average powers transmitted through the horizontal-horizontal subchannel:

$$\text{CPR}_{qp,\tilde{q}\tilde{p}} = \frac{E\{|h_{\tilde{q}\tilde{p}}|^2\}}{E\{|h_{q\tilde{p}}|^2\}}. \quad (14)$$

The CPR depends on the Brewster angle phenomenon [31].

The XPD and CPR, when expressed in decibel (dB), are often observed as having the normal distribution with $N(\mu, \sigma)$. In [7], the mean of XPD varies from 0 to 18 dB, with the standard deviation in order of 3 ~ 8 dB. Normally, the received power in the vertical-to-vertical transmission is reported to be greater than that in the horizontal-to-horizontal transmission ($\text{CPR} > 0$ dB). For example, the mean of the CPR is reported to vary between 0 and 6 dB [15]. Depending on the propagation environment and transmission configuration, the CPR may be less than 0 dB when the amplitude of vertically polarized waves is degraded more than that of horizontally polarized waves or the transmission power of horizontally polarized waves is greater than that of vertically polarized waves. When the XPD or

CPR in dB is denoted as X , the expectations in (12) can be computed as

$$\begin{aligned} E\left\{\sqrt{r_{p\tilde{q}}^{(m)}}\right\} &= E\left\{\sqrt{r_{\tilde{p}q}^{(m)}}\right\} = E\left\{10^{-(X/20)}\right\}, \\ E\left\{\sqrt{\frac{1}{\text{CPR}_{q\tilde{p},\tilde{q}\tilde{p}}}}\right\} &= E\left\{10^{-(X/20)}\right\}. \end{aligned} \quad (15)$$

When X has the normal distribution with $N(\mu, \sigma)$, then the expectation $E\{10^{-X/20}\}$ over an interval $[x_1, x_2]$ can be expressed as

$$E\left\{10^{-(X/20)}\right\} = \int_{x_1}^{x_2} 10^{-(x/20)} \frac{1}{\sqrt{2\pi\sigma^2}} \exp\left(-\frac{(x-\mu)^2}{2\sigma^2}\right) dx. \quad (16)$$

For simplicity, we adopt the normal XPD model to characterize cross-polarized components in the 3D modeling of 2×2 DP-MIMO M2M channels.

When the elevation angles of arrival/departure are small, the distances $d(A_t^{(p)}, S_t^{(m)})$, $d(S_t^{(m)}, A_r^{(q)})$, $d(A_t^{(p)}, S_r^{(n)})$, $d(S_r^{(n)}, A_r^{(q)})$, $d(S_t^{(m)}, S_r^{(n)})$ and $d(A_t^{(p)}, A_r^{(q)})$ can be approximated as below

$$\begin{aligned} |d(A_t^{(p)}, S_t^{(m)})| &= \epsilon_{p,m} \approx R_t, \\ |d(S_t^{(m)}, A_r^{(q)})| &= \epsilon_{m,q} \approx D, \\ |d(A_t^{(p)}, S_r^{(n)})| &= \epsilon_{p,n} \approx D, \\ |d(S_r^{(n)}, A_r^{(q)})| &= \epsilon_{n,q} \approx R_r, \\ |d(A_t^{(p)}, A_r^{(q)})| &= \epsilon_{pq} \approx D, \\ |d(S_t^{(m)}, S_r^{(n)})| &= \epsilon_{m,n} \approx \sqrt{(R_t - R_r)^2 + D^2}. \end{aligned} \quad (17)$$

Furthermore, using the Taylor series expansion, the amplitudes of the multipath components, $\xi_{p,m,q}$ or $\xi_{p,m,\tilde{q}}$ are approximately given by

$$\begin{aligned} \xi_{p,m,q} &= \xi_{p,m,\tilde{q}} \\ &= \left[|d(A_t^{(p)}, S_t^{(m)})| + |d(S_t^{(m)}, A_r^{(q)})| \right]^{-\gamma/2} \\ &\approx A_m \left(1 - \frac{\gamma R_t}{2D}\right), \end{aligned} \quad (18)$$

where γ is the path loss exponent, whose value is normally in the range of 2 to 4, depending upon the propagation environment. $\xi_{\tilde{p},m,\tilde{q}}$ or $\xi_{\tilde{p},m,q}$ is approximated as

$$\begin{aligned} \xi_{\tilde{p},m,\tilde{q}} &= \xi_{\tilde{p},m,q} \\ &= \sqrt{\frac{1}{\text{CPR}_{q\tilde{p},\tilde{q}\tilde{p}}}} \left[|d(A_t^{(p)}, S_t^{(m)})| + |d(S_t^{(m)}, A_r^{(q)})| \right]^{-\gamma/2} \\ &\approx A_m \sqrt{\frac{1}{\text{CPR}_{q\tilde{p},\tilde{q}\tilde{p}}}} \left(1 - \frac{\gamma R_t}{2D}\right), \end{aligned} \quad (19)$$

where A_m is defined as

$$A_m = D^{-\gamma/2}. \quad (20)$$

Similarly, $\xi_{p,n,q}$ or $\xi_{p,n,\tilde{q}}$ is approximated as

$$\begin{aligned} \xi_{p,n,q} &= \xi_{p,n,\tilde{q}} \\ &= \left[|d(A_r^{(p)}, S_r^{(n)})| + |d(S_r^{(n)}, A_r^{(q)})| \right]^{-\gamma/2} \\ &\approx A_m \left(1 - \frac{\gamma R_r}{2D}\right), \end{aligned} \quad (21)$$

$\xi_{\tilde{p},n,\tilde{q}}$ or $\xi_{\tilde{p},n,q}$ is approximated as

$$\begin{aligned} \xi_{\tilde{p},n,\tilde{q}} &= \xi_{\tilde{p},n,q} \\ &= \sqrt{\frac{1}{\text{CPR}_{q\tilde{p},\tilde{q}\tilde{p}}}} \left[|d(A_r^{(p)}, S_r^{(n)})| + |d(S_r^{(n)}, A_r^{(q)})| \right]^{-\gamma/2} \\ &\approx A_m \sqrt{\frac{1}{\text{CPR}_{q\tilde{p},\tilde{q}\tilde{p}}}} \left(1 - \frac{\gamma R_r}{2D}\right). \end{aligned} \quad (22)$$

The time delays $\tau_{p,m,q}$ and $\tau_{p,n,q}$ are the travel times of the signals scattered from the Tx scatterer $S_t^{(m)}$, and from the Rx scatterer $S_r^{(n)}$, respectively

$$\tau_{p,m,q} = \frac{\epsilon_{p,m} + \epsilon_{m,q}}{c}, \quad (23)$$

$$\tau_{p,n,q} = \frac{\epsilon_{p,n} + \epsilon_{n,q}}{c}, \quad (24)$$

where c is the speed of the light.

The time-varying phase function $g_{a,m,b}(t)$ along the path $A_t^{(p)} \rightarrow S_t^{(m)} \rightarrow A_r^{(q)}$ is given by

$$\begin{aligned} g_{p,m,q}(t) &= \exp\left[-j\frac{2\pi}{\lambda_c}(\epsilon_{p,m} + \epsilon_{m,q})\right] \\ &\times \exp\left[j2\pi t f_{t\max} \cos(\phi_t^{(m)} - \phi_{vt}) \cos\theta_t^{(m)} \cos\theta_{vt}\right] \\ &\times \exp\left(j2\pi t f_{t\max} \sin\theta_t^{(m)} \sin\theta_{vt}\right) \\ &\times \exp\left[j2\pi t f_{r\max} \cos(\phi_r^{(m)} - \phi_{vr}) \cos\theta_r^{(m)} \cos\theta_{vr}\right] \\ &\times \exp\left(j2\pi t f_{r\max} \sin\theta_r^{(m)} \sin\theta_{vr}\right), \end{aligned} \quad (25)$$

where $f_{t\max} = vt/\lambda_c$ and $f_{r\max} = vr/\lambda_c$ are the maximum.

Doppler frequencies associated with the Tx and Rx respectively and λ_c denotes the carrier wavelength.

The time-varying phase function $g_{p,m,b}(t)$ along the path $A_t^{(p)} \rightarrow S_r^{(n)} \rightarrow A_r^{(q)}$ is given by

$$\begin{aligned} g_{p,n,q}(t) = & \exp\left[-j\frac{2\pi}{\lambda_c}(\epsilon_{p,n} + \epsilon_{n,q})\right] \\ & \times \exp\left[j2\pi t f_{t\max} \cos(\phi_t^{(n)} - \phi_{vt}) \cos\theta_t^{(n)} \cos\theta_{vt}\right] \\ & \times \exp\left(j2\pi t f_{t\max} \sin\theta_t^{(n)} \sin\theta_{vt}\right) \\ & \times \exp\left[j2\pi t f_{r\max} \cos(\phi_r^{(n)} - \phi_{vr}) \cos\theta_r^{(n)} \cos\theta_{vr}\right] \\ & \times \exp\left(j2\pi t f_{r\max} \sin\theta_r^{(n)} \sin\theta_{vr}\right). \end{aligned} \quad (26)$$

The parameters ρ_m^{SBT} and ρ_n^{SBR} represent scattering loss factors, and are governed by [32]

$$\rho = \exp\left[-8\left(\frac{\pi\sigma_h \sin\theta_i}{\lambda_c}\right)^2\right] I_0\left[8\left(\frac{\pi\sigma_h \sin\theta_i}{\lambda_c}\right)^2\right], \quad (27)$$

where σ_h is the standard deviation of the surface height of the scatterer, θ_i is a given angle of incidence, and $I_0(\cdot)$ is the zero-order modified Bessel function of the first kind.

2.3. Double-Bounce Channel Impulse Response. The double-bounce components of the channel impulse responses are

$$\begin{aligned} h_{pq}^{\text{DB}}(t, \tau) &= \sqrt{\frac{\eta_{tr,pq}}{K+1}} \frac{1}{\sqrt{MN}} \sum_{m=1}^M \sum_{n=1}^N \xi_{a,m,n,b} g_{a,m,n,b}(t) \\ & \times \delta(\tau - \tau_{a,m,n,b}) \\ & \times \left[\sqrt{G_a^{(v)}(\phi_t^{(m)}, \theta_t^{(m)})} \sqrt{G_a^{(h)}(\phi_t^{(m)}, \theta_t^{(m)})} \right] \\ & \times \begin{bmatrix} 1 & \sqrt{r_{p\tilde{q}}^{(m)}} \\ \sqrt{r_{\tilde{p}q}^{(m)}} & 1 \end{bmatrix} \begin{bmatrix} 1 & \sqrt{r_{\tilde{p}\tilde{q}}^{(n)}} \\ \sqrt{r_{\tilde{p}q}^{(n)}} & 1 \end{bmatrix} \\ & \times \begin{bmatrix} \sqrt{G_b^{(v)}(\phi_r^{(n)}, \theta_r^{(n)})} \\ \sqrt{G_b^{(h)}(\phi_r^{(n)}, \theta_r^{(n)})} \end{bmatrix} \\ & \times \exp\left(j\phi_{ab}^{(m,n)}\right) \rho_m^{\text{SBT}} \rho_n^{\text{SBR}}, \end{aligned} \quad (28)$$

where the power ratio coefficients $\eta_{tr,ab}$ ($a \in \{p, \tilde{p}\}, b \in \{q, \tilde{q}\}$) in (28), specify the ratio of the power of the double-bounce ray along the subchannels $A_t^{(a)} \rightarrow A_r^{(b)}$ with respect to the averaged transmit power P_{ab} between the Tx antenna element a and the Rx antenna element b . The power ratio coefficients of the single-bounce and the double-bounce rays satisfy

$$\eta_{t,ab} + \eta_{r,ab} + \eta_{tr,ab} = 1, \quad (a \in \{p, \tilde{p}\}, b \in \{q, \tilde{q}\}). \quad (29)$$

$\xi_{a,m,n,b}$ denotes the amplitude and $\tau_{a,m,n,b}$ denotes the time delay of the multipath components along the path $A_t^{(a)} \rightarrow S_t^{(m)} \rightarrow S_r^{(n)} \rightarrow A_r^{(b)}$ ($a \in \{p, \tilde{p}\}, b \in \{q, \tilde{q}\}$). The amplitudes of the multipath components $\xi_{p,m,n,q}$ and $\xi_{\tilde{p},m,n,\tilde{q}}$ are given by

$$\begin{aligned} \xi_{p,m,n,q} &= \xi_{\tilde{p},m,n,\tilde{q}} \\ & \times \left[\left| d(A_t^{(p)}, S_t^{(m)}) \right| + \left| d(S_t^{(m)}, S_r^{(n)}) \right| \right. \\ & \quad \left. + \left| d(S_r^{(n)}, A_r^{(q)}) \right| \right]^{-\gamma/2} \\ & \approx A_m \left(1 - \frac{\gamma}{2} \frac{R_t + R_r}{D} \right). \end{aligned} \quad (30)$$

The amplitudes of the multipath components $\xi_{\tilde{p},m,n,\tilde{q}}$ and $\xi_{\tilde{p},m,n,q}$ are given by

$$\begin{aligned} \xi_{\tilde{p},m,n,\tilde{q}} &= \xi_{\tilde{p},m,n,q} = \sqrt{\frac{1}{\text{CPR}_{qp,\tilde{q}\tilde{p}}}} \\ & \times \left[\left| d(A_t^{(p)}, S_t^{(m)}) \right| + \left| d(S_t^{(m)}, S_r^{(n)}) \right| \right. \\ & \quad \left. + \left| d(S_r^{(n)}, A_r^{(q)}) \right| \right]^{-\gamma/2} \\ & \approx A_m \sqrt{\frac{1}{\text{CPR}_{qp,\tilde{q}\tilde{p}}}} \left(1 - \frac{\gamma}{2} \frac{R_t + R_r}{D} \right). \end{aligned} \quad (31)$$

As DP antenna pair are collocated at the center of Tx and the center of Rx without considering the size of antennas, the time delays $\tau_{a,m,n,b}$ are equivalent between antennas $A_t^{(a)}$ and $A_r^{(b)}$

$$\tau_{p,m,n,q} = \tau_{p,m,n,\tilde{q}} = \tau_{\tilde{p},m,n,q} = \tau_{\tilde{p},m,n,\tilde{q}}. \quad (32)$$

The time delay $\tau_{p,m,n,q}$ is the travel time of the signals scattered from both the Tx scatterer $S_t^{(m)}$ and the Rx scatterer $S_r^{(n)}$

$$\tau_{p,m,n,q} = \frac{\epsilon_{p,m} + \epsilon_{m,n} + \epsilon_{n,q}}{c}. \quad (33)$$

Similarly, $g_{a,m,n,b}(t)$ satisfy

$$g_{p,m,n,q}(t) = g_{p,m,n,\tilde{q}}(t) = g_{\tilde{p},m,n,q}(t) = g_{\tilde{p},m,n,\tilde{q}}(t). \quad (34)$$

The time-varying function $g_{p,m,n,q}(t)$ is given by

$$\begin{aligned} g_{p,m,n,q}(t) = & \exp\left[-j\frac{2\pi}{\lambda_c}(\epsilon_{p,m} + \epsilon_{m,n} + \epsilon_{n,q})\right] \\ & \times \exp\left[j2\pi t f_{t\max} \cos(\phi_t^{(m)} - \phi_{vt}) \cos\theta_t^{(m)} \cos\theta_{vt}\right] \\ & \times \exp\left(j2\pi t f_{t\max} \sin\theta_t^{(m)} \sin\theta_{vt}\right) \\ & \times \exp\left[j2\pi t f_{r\max} \cos(\phi_r^{(n)} - \phi_{vr}) \cos\theta_r^{(n)} \cos\theta_{vr}\right] \\ & \times \exp\left(j2\pi t f_{r\max} \sin\theta_r^{(n)} \sin\theta_{vr}\right). \end{aligned} \quad (35)$$

The random variable $\phi_{ab}^{(m,n)}$ is the phase offset of the double-bounce path scattered by both the Tx scatterer $S_t^{(m)}$ and the Rx scatterer $S_r^{(n)}$ between the V or H component of the Tx antenna elements and the V or H component of the Rx antenna elements.

2.4. LOS Channel Impulse Response. The LOS components of channel impulse responses are

$$h_{ab}^{\text{LOS}}(t, \tau) = \sqrt{\frac{K}{K+1}} \xi_{a,b}^{\text{LOS}} g_{a,b}^{\text{LOS}}(t) \delta(\tau - \tau_{a,b}^{\text{LOS}}) \times \sqrt{G_a(\phi_t^{\text{LOS}}, \theta_t^{\text{LOS}}) G_b(\phi_r^{\text{LOS}}, \theta_r^{\text{LOS}})}, \quad (36)$$

where $\xi_{a,b}^{\text{LOS}}$ ($a \in \{p, \tilde{p}\}, b \in \{q, \tilde{q}\}$) denotes the amplitude and $\tau_{a,b}^{\text{LOS}}$ denotes the time delay of the LOS components between the antenna element $A_t^{(a)}$ at the Tx and the antenna element $A_r^{(b)}$ at the Rx. The time-varying function $g_{a,b}^{\text{LOS}}(t)$ is defined as

$$\begin{aligned} g_{p,q}^{\text{LOS}}(t) &= g_{p,\tilde{q}}^{\text{LOS}}(t) = g_{\tilde{p},q}^{\text{LOS}}(t) = g_{\tilde{p},\tilde{q}}^{\text{LOS}}(t) \\ &= \exp\left(-j \frac{2\pi}{\lambda_c} \epsilon_{p,q}\right) \\ &\quad \times \exp\left[j2\pi t f_{t,\max} \cos(\phi_t^{\text{LOS}} - \phi_{vt}) \cos \theta_t^{\text{LOS}} \cos \theta_{vt}\right] \\ &\quad \times \exp\left(j2\pi t f_{t,\max} \sin \theta_t^{\text{LOS}} \sin \theta_{vt}\right) \\ &\quad \times \exp\left[j2\pi t f_{r,\max} \cos(\phi_r^{\text{LOS}} - \phi_{vr}) \cos \theta_r^{\text{LOS}} \cos \theta_{vr}\right] \\ &\quad \times \exp\left(j2\pi t f_{r,\max} \sin \theta_r^{\text{LOS}} \sin \theta_{vr}\right). \end{aligned} \quad (37)$$

The amplitude of the LOS components $\xi_{a,b}^{\text{LOS}}$ is given by

$$\begin{aligned} \xi_{p,q}^{\text{LOS}} &= \xi_{p,\tilde{q}}^{\text{LOS}} \approx D \frac{\gamma}{2} = A_m, \\ \xi_{\tilde{p},q}^{\text{LOS}} &= \xi_{\tilde{p},\tilde{q}}^{\text{LOS}} \approx \sqrt{\frac{1}{\text{CPR}_{qp,\tilde{q}\tilde{p}}}} D \frac{\gamma}{2} = A_m \sqrt{\frac{1}{\text{CPR}_{qp,\tilde{q}\tilde{p}}}}. \end{aligned} \quad (38)$$

The time delay $\tau_{a,b}^{\text{LOS}}$ is the travel time of the signal from the Tx antenna element $A_t^{(a)}$ and the Rx antenna element $A_r^{(b)}$. Consider the following:

$$\tau_{p,q}^{\text{LOS}} = \tau_{p,\tilde{q}}^{\text{LOS}} = \tau_{\tilde{p},q}^{\text{LOS}} = \tau_{\tilde{p},\tilde{q}}^{\text{LOS}} = \frac{\epsilon_{p,q}}{c}. \quad (39)$$

It is assumed that the elevation angles ($\theta_t^{\text{LOS}}, \theta_r^{\text{LOS}}, \theta_t^{(m)}, \theta_t^{(n)}, \theta_r^{(m)},$ and $\theta_r^{(n)}$) and the azimuth angles ($\phi_t^{\text{LOS}}, \phi_r^{\text{LOS}}, \phi_t^{(m)}, \phi_t^{(n)}, \phi_r^{(m)}$ and $\phi_r^{(n)}$) are independent random variables. The

radii R_t of the Tx sphere and R_r of the Rx sphere are also independent. The phase offsets $\phi_{ab}^{(m)}, \phi_{ab}^{(n)},$ and $\phi_{ab}^{(m,n)}$ are assumed to be uniformly random variables on the interval $[-\pi, \pi)$ that are independent from the elevation angles, azimuth angles, and radii of the scattering spheres. Using the Central Limit Theorem [33, 34], we posit that the delay-spread functions $h_{ab}^{\text{SBT}}(t, \tau), h_{ab}^{\text{SBR}}(t, \tau), h_{ab}^{\text{LOS}}(t, \tau),$ and $h_{ab}^{\text{DB}}(t, \tau)$ are zero-mean complex Gaussian random processes.

2.5. Time-Variant Transfer Functions. The time-variant transfer function is the Fourier transform of the channel impulse response with respect to the delay τ . Consider the following:

$$\begin{aligned} \mathbf{T}_{ab}(t, f) &= F_\tau \{h_{ab}(t, \tau)\} = \mathbf{T}_{ab}^{\text{SBT}}(t, f) + \mathbf{T}_{ab}^{\text{SBR}}(t, f) \\ &\quad + \mathbf{T}_{ab}^{\text{DB}}(t, f) + \mathbf{T}_{ab}^{\text{LOS}}(t, f), \end{aligned} \quad (40)$$

where $\mathbf{T}_{ab}^{\text{SBT}}(t, f), \mathbf{T}_{ab}^{\text{SBR}}(t, f), \mathbf{T}_{ab}^{\text{DB}}(t, f),$ and $\mathbf{T}_{ab}^{\text{LOS}}(t, f)$ ($a \in \{p, \tilde{p}\}, b \in \{q, \tilde{q}\}$) are time-variant transfer functions for the SBT, SBR, DB and LOS components, respectively.

3. Polarization Matched Time-Frequency Correlation Functions

Wide-sense stationarity and uncorrelated scatterers are often assumed to be valid for mobile radio channels [18]. In this paper, time and frequency dispersion are modeled dependently over a wide sense stationary uncorrelated scattering channel for a 3D nonisotropic scattering environment. For such channels, the time-frequency correlation function is an effective way of characterizing the statistical dependencies in the temporal and frequency domains associated with the mobile-to-mobile channels. Since the polarization states of antennas at both the Tx and Rx are matched, we derive the matched polarization-basis time-frequency correlation function to show the relationship between the frequency and the time of the 3D statistical model for 2×2 DP antennas.

For a WSSUS channel, the TFCF of the time-varying transfer function \mathbf{T}_{ab} ($a \in \{p, \tilde{p}\}, b \in \{q, \tilde{q}\}$) is defined in terms of the time difference Δ_t and the frequency separation Δ_f

$$\rho_{ab}(\Delta_t, \Delta_f) = E[\mathbf{T}_{ab}(t, f)^* \mathbf{T}_{ab}(t + \Delta_t, f + \Delta_f)], \quad (41)$$

where $a \in \{p, \tilde{p}\}, b \in \{q, \tilde{q}\}$ and $p, \tilde{p}, q, \tilde{q}$ correspond to vertical and horizontal antenna polarizations. $E[\cdot]$ is the expectation operator, and $*$ denotes the complex conjugate operation. The TFCFs in (41) can be rewritten as the superposition of the TFCFs of the SBT, SBR, DB and LOS components. Consider

$$\begin{aligned} \rho_{ab}(\Delta_t, \Delta_f) &= \rho_{ab}^{\text{SBT}}(\Delta_t, \Delta_f) + \rho_{ab}^{\text{SBR}}(\Delta_t, \Delta_f) \\ &\quad + \rho_{ab}^{\text{DB}}(\Delta_t, \Delta_f) + \rho_{ab}^{\text{LOS}}(\Delta_t, \Delta_f). \end{aligned} \quad (42)$$

In order to estimate the time frequency correlations, we make the assumption that the number of scatterers in the 3D reference model is infinite so that the discrete azimuth angles ($\phi_t^{(m)}$, $\phi_r^{(m)}$, $\phi_t^{(n)}$ and $\phi_r^{(n)}$), the discrete elevation angles ($\theta_t^{(m)}$, $\theta_r^{(m)}$, $\theta_t^{(n)}$, and $\theta_r^{(n)}$) and the radii R_t , R_r can be represented as continuous random variables with probability density functions of $f(\phi_r^{(s)})$, $f(\phi_t^{(s)})$, $f(\theta_r^{(s)})$, $f(\theta_t^{(s)})$, $f(R_t)$, and $f(R_r)$, respectively. The form of these pdf's are as follows.

The Tx azimuth angles are characterized by the von Mises pdf in (2) as

$$f(\phi_t^{(s)}) = \frac{\exp[\kappa_t^{(s)} \cos(\phi_t^{(s)} - \mu_t^{(s)})]}{2\pi I_0(\kappa_t^{(s)})}, \quad (43)$$

where $\mu_t^{(s)} \in [-\pi, \pi)$ is the mean value of angle at which the Tx scatterers are distributed in the x - y plane and $\kappa_t^{(s)}$ controls the spread of Tx scatterers around the mean $\mu_t^{(s)}$. Similarly, the Rx azimuth angles are characterized by

$$f(\phi_r^{(s)}) = \frac{\exp[\kappa_r^{(s)} \cos(\phi_r^{(s)} - \mu_r^{(s)})]}{2\pi I_0(\kappa_r^{(s)})}, \quad (44)$$

where $\mu_r^{(s)} \in [-\pi, \pi)$ is the mean value of angle at which the Rx scatterers are distributed in the x - y plane and $\kappa_r^{(s)}$ controls the spread of Rx scatterers around the mean $\mu_r^{(s)}$.

The Tx and Rx elevation angles are characterized by the cosine pdf in (3) as

$$f(\theta_t^{(s)}) = \begin{cases} \frac{\pi}{4|\theta_{tm}|} \cos\left(\frac{\pi \theta_t^{(s)}}{2 \theta_{tm}}\right), & |\theta_t^{(s)}| \leq |\theta_{tm}| \leq \frac{\pi}{2}, \\ 0, & \text{otherwise,} \end{cases}$$

$$f(\theta_r^{(s)}) = \begin{cases} \frac{\pi}{4|\theta_{rm}|} \cos\left(\frac{\pi \theta_r^{(s)}}{2 \theta_{rm}}\right), & |\theta_r^{(s)}| \leq |\theta_{rm}| \leq \frac{\pi}{2}, \\ 0, & \text{otherwise,} \end{cases} \quad (45)$$

where θ_{tm} is the maximum elevation angle for the Tx scatterers and θ_{rm} is the maximum elevation angle for the Rx scatterers.

The pdfs used to characterize the radii R_t and R_r are given by

$$f(R_t) = \frac{3R_t^2}{R_{t2}^3 - R_{t1}^3} \quad R_{t1} \leq R_t \leq R_{t2},$$

$$f(R_r) = \frac{3R_r^2}{R_{r2}^3 - R_{r1}^3} \quad R_{r1} \leq R_r \leq R_{r2}. \quad (46)$$

The pdf of phase-offset random variables $\phi_m^{(pol)}$, $\phi_{ab}^{(m)}$, $\phi_{ab}^{(n)}$, and $\phi_{ab}^{(m,n)}$ ($a \in \{p, \tilde{p}\}$ and $b \in \{q, \tilde{q}\}$) is given

by a uniform distribution on the interval $[-\pi, \pi)$. Using these distributions, the TFCFs $\rho^{SBT}(\Delta t, \Delta f)$, $\rho^{SBR}(\Delta t, \Delta f)$, $\rho^{DB}(\Delta t, \Delta f)$, and $\rho^{LOS}(\Delta t, \Delta f)$ of the time-variant transfer functions for the corresponding SBT, SBR, DB and LOS components are derived below.

Using these pdfs it is possible to formulate the TFCFs for each of the bounce path components. The TFCFs along the SBT path are given by

$$\rho_{ab}^{SBT}(\Delta t, \Delta f) = \frac{\eta_{t,pq} A_m^2}{K+1} I_{ab}^{SBT}(\Delta t, \Delta f), \quad (47)$$

where $I_{ab}^{SBT}(\Delta t, \Delta f)$ is defined as

$$I_{ab}^{SBT}(\Delta t, \Delta f) = \frac{1}{8|\theta_{tm}| I_0(\kappa_t^{(s)})} \int_{R_{t1}}^{R_{t2}} \int_{-\theta_{tm}}^{\theta_{tm}} \int_{-\pi}^{\pi} \left(1 - \frac{\gamma R_t}{2D}\right)^2 \times \exp\left[-j \frac{2\pi}{c} \Delta f (\epsilon_{p,m} + \epsilon_{m,q})\right] \frac{3R_t^2}{R_{t2}^3 - R_{t1}^3} \times \cos\left(\frac{\pi \theta_t^{(s)}}{2 \theta_{tm}}\right) \exp[\kappa_t^{(s)} \cos(\phi_t^{(s)} - \mu_t^{(s)})] \times \exp[j2\pi \Delta_t f_{t \max} \cos(\phi_t^{(s)} - \phi_{vt}) \cos \theta_t^{(s)} \cos \theta_{vt}] \times \exp(j2\pi \Delta_t f_{t \max} \sin \theta_t^{(s)} \sin \theta_{vt}) \times \exp[j2\pi \Delta_t f_{r \max} \cos(\phi_r^{(s)} - \phi_{vr}) \cos(\theta_r^{(s)}) \cos \theta_{vr}] \times \exp(j2\pi \Delta_t f_{r \max} \sin \theta_r^{(s)} \sin \theta_{vr}) \times \exp\left[-8 \left(\frac{\pi \sigma_h \sin \theta_t^{(i)}}{\lambda_c}\right)^2\right] I_0 \left[8 \left(\frac{\pi \sigma_h \sin \theta_t^{(i)}}{\lambda_c}\right)^2\right] \times E\left[\sqrt{\frac{1}{\text{CPR}_{qp, \tilde{q}\tilde{p}}}}\right] \left[\sqrt{G_a^{(v)}(\phi_t^{(s)}, \theta_t^{(s)})} \sqrt{G_a^{(h)}(\phi_t^{(s)}, \theta_t^{(s)})}\right] \times \begin{bmatrix} 1 & E\left[\sqrt{r_{p\tilde{q}}^{(m)}}\right] \\ E\left[\sqrt{r_{\tilde{p}q}^{(m)}}\right] & 1 \end{bmatrix} \begin{bmatrix} \sqrt{G_b^{(v)}(\phi_r^{(s)}, \theta_r^{(s)})} \\ \sqrt{G_b^{(h)}(\phi_r^{(s)}, \theta_r^{(s)})} \end{bmatrix} \times d\phi_t^{(s)} d\theta_t^{(s)} dR_t. \quad (48)$$

$E[\sqrt{r_{p\tilde{q}}^{(m)}}]$ and $E[\sqrt{r_{\tilde{p}q}^{(m)}}]$ represent the expectations of the random variables $\sqrt{r_{p\tilde{q}}^{(m)}}$ and $\sqrt{r_{\tilde{p}q}^{(m)}}$, respectively, over the interval $[-20 \text{ dB}, 20 \text{ dB}]$. They are calculated using the pdf of the normal XPD model in (16). $E[\sqrt{\text{CPR}_{qp, \tilde{q}\tilde{p}}}]$ denotes the expectation of random variable of copolar ratio over the interval $[0, 6 \text{ dB}]$.

At the Rx, the azimuth angle $\phi_r^{(s)}$ and elevation angle $\theta_r^{(s)}$ induced by the scatterer $S_t^{(m)}$ are approximated as

$$\begin{aligned}\phi_r^{(s)} &\approx \frac{3\pi}{2} + \frac{R_t}{D} \sin \phi_t^{(s)}, \\ \theta_r^{(s)} &\approx \frac{R_t}{D} \theta_t^{(s)} + \frac{\Delta_z}{D}.\end{aligned}\quad (49)$$

The angle of incidence $\theta_t^{(i)}$ with the surface of Tx scatterer can be determined by using trigonometric identities in the triangle $O_t - S_t^{(m)} - O_r$ as follows:

$$\theta_t^{(i)} \approx \frac{1}{2} \arccos\left(\frac{R_t^2 + d_{m,r}^2 - D^2}{2R_t d_{m,r}}\right), \quad (50)$$

where $d_{m,r}$ is given by

$$\begin{aligned}d_{m,r}^2 &= (\Delta_x - R_t \cos \theta_t^{(s)} \cos \phi_t^{(s)})^2 \\ &+ (\Delta_y - R_t \cos \theta_t^{(s)} \sin \phi_t^{(s)})^2 \\ &+ (\Delta_z - R_t \sin \theta_t^{(s)})^2.\end{aligned}\quad (51)$$

The TFCFs along the SBR path are given by

$$\rho_{ab}^{\text{SBR}}(\Delta_t, \Delta_f) = \frac{\eta_{r,ab} A_m^2}{K+1} I_{ab}^{\text{SBR}}(\Delta_t, \Delta_f), \quad (52)$$

where $I_{ab}^{\text{SBR}}(\Delta_t, \Delta_f)$ is defined as

$$\begin{aligned}I_{ab}^{\text{SBR}}(\Delta_t, \Delta_f) &= \frac{1}{8|\theta_{rm}| I_0(\kappa_r^{(s)})} \int_{R_{r1}}^{R_{r2}} \int_{-\theta_{rm}}^{\theta_{rm}} \int_{-\pi}^{\pi} \left(1 - \frac{\gamma R_r}{2 D_2}\right)^2 \\ &\times \exp\left[-j \frac{2\pi}{c} \Delta_f (\epsilon_{p,n} + \epsilon_{n,q})\right] \frac{3R_r^2}{R_{r2}^3 - R_{r1}^3} \\ &\times \cos\left(\frac{\pi}{2} \frac{\theta_r^{(s)}}{\theta_{rm}}\right) \exp\left[\kappa_r^{(s)} \cos(\phi_r^{(s)} - \mu_r^{(s)})\right] \\ &\times \exp\left[j2\pi \Delta_t f_{t \max} \cos(\phi_t^{(s)} - \phi_{vt}) \cos \theta_t^{(s)} \cos \theta_{vt}\right] \\ &\times \exp\left(j2\pi \Delta_t f_{t \max} \sin \theta_t^{(s)} \sin \theta_{vt}\right) \\ &\times \exp\left[j2\pi \Delta_t f_{r \max} \cos(\phi_r^{(s)} - \phi_{vr}) \cos \theta_r^{(s)} \cos \theta_{vr}\right]\end{aligned}$$

$$\begin{aligned}&\times \exp\left(j2\pi \Delta_t f_{r \max} \sin \theta_r^{(s)} \sin \theta_{vr}\right) \\ &\times \exp\left[-8 \left(\frac{\pi \sigma_h \sin \theta_r^{(i)}}{\lambda_c}\right)^2\right] I_0\left[8 \left(\frac{\pi \sigma_h \sin \theta_r^{(i)}}{\lambda_c}\right)^2\right] \\ &\times E\left[\sqrt{\frac{1}{\text{CPR}_{qp, \tilde{q}\tilde{p}}}}\right] \left[\sqrt{G_a^{(v)}(\phi_t^{(s)}, \theta_t^{(s)})} \sqrt{G_a^{(h)}(\phi_t^{(s)}, \theta_t^{(s)})}\right] \\ &\times \begin{bmatrix} 1 & E\left[\sqrt{r_{p\tilde{q}}^{(n)}}\right] \\ E\left[\sqrt{r_{\tilde{p}q}^{(n)}}\right] & 1 \end{bmatrix} \begin{bmatrix} \sqrt{G_b^{(v)}(\phi_r^{(s)}, \theta_r^{(s)})} \\ \sqrt{G_b^{(h)}(\phi_r^{(s)}, \theta_r^{(s)})} \end{bmatrix} \\ &\times d\phi_r^{(s)} d\theta_r^{(s)} dR_r,\end{aligned}\quad (53)$$

where $E\left[\sqrt{r_{p\tilde{q}}^{(n)}}\right]$ and $E\left[\sqrt{r_{\tilde{p}q}^{(n)}}\right]$ represent the expectations of the random variables $\sqrt{r_{p\tilde{q}}^{(n)}}$ and $\sqrt{r_{\tilde{p}q}^{(n)}}$, respectively. They are calculated over the interval $[-20 \text{ dB}, 20 \text{ dB}]$ using the pdf of the normal XPD model in (16).

At the Tx, the azimuth angle $\phi_t^{(s)}$ and elevation angle $\theta_t^{(s)}$ induced by the scatterer $S_r^{(n)}$ are approximated as

$$\begin{aligned}\phi_t^{(s)} &\approx \frac{R_r}{D} \sin \phi_r^{(s)}, \\ \theta_t^{(s)} &\approx \frac{R_r}{D} \theta_r^{(s)} - \frac{\Delta_z}{D}.\end{aligned}\quad (54)$$

The angle of incidence $\theta_r^{(i)}$ with the surface of Rx scatterer can be determined by using trigonometric identities in the triangle $O_t - S_r^{(n)} - O_r$ as follows:

$$\theta_r^{(i)} \approx \frac{1}{2} \arccos\left(\frac{R_r^2 + d_{t,n}^2 - D^2}{2R_r d_{t,n}}\right), \quad (55)$$

where $d_{t,n}$ is given by

$$\begin{aligned}d_{t,n}^2 &= (\Delta_x + R_r \cos \theta_r^{(s)} \cos \phi_r^{(s)})^2 \\ &+ (\Delta_y + R_r \cos \theta_r^{(s)} \sin \phi_r^{(s)})^2 \\ &+ (\Delta_z + R_r \sin \theta_r^{(s)})^2.\end{aligned}\quad (56)$$

The TFCFs along the DB path are given by

$$\rho_{ab}^{\text{DB}}(\Delta_t, \Delta_f) = \frac{\eta_{tr,ab} A_m^2}{K+1} I_{ab}^{\text{DB}}(\Delta_t, \Delta_f), \quad (57)$$

where $I_{ab}^{\text{DB}}(\Delta_t, \Delta_f)$ is defined as

$$\begin{aligned}
I_{ab}^{\text{DB}}(\Delta_t, \Delta_f) &= \frac{1}{64|\theta_{tm}||\theta_{rm}|I_0(\kappa_t^{(s)})I_0(\kappa_r^{(s)})} \\
&\times \int_{R_{r1}}^{R_{r2}} \int_{R_{r1}}^{R_{r2}} \int_{-\theta_{tm}}^{\theta_{tm}} \int_{-\theta_{rm}}^{\theta_{rm}} \int_{-\pi}^{\pi} \int_{-\pi}^{\pi} \left(1 - \frac{\gamma}{2} \frac{R_r + R_t}{D}\right)^2 \\
&\times \exp\left[-j\frac{2\pi}{c}\Delta_f(\epsilon_{p,m} + \epsilon_{m,n} + \epsilon_{n,q})\right] \\
&\times \frac{3R_r^2}{R_{r2}^3 - R_{r1}^3} \frac{3R_t^2}{R_{t2}^3 - R_{t1}^3} \cos\left(\frac{\pi}{2} \frac{\theta_t^{(s)}}{\theta_{tm}}\right) \cos\left(\frac{\pi}{2} \frac{\theta_r^{(s)}}{\theta_{rm}}\right) \\
&\times \exp\left[\kappa_t^{(s)} \cos(\phi_t^{(s)} - \mu_t^{(s)})\right] \exp\left[\kappa_r^{(s)} \cos(\phi_r^{(s)} - \mu_r^{(s)})\right] \\
&\times \exp\left[j2\pi\Delta_t f_{t \max} \cos(\phi_t^{(s)} - \phi_{vt}) \cos\theta_t^{(s)} \cos\theta_{vt}\right] \\
&\times \exp\left(j2\pi\Delta_t f_{t \max} \sin\theta_t^{(s)} \sin\theta_{vt}\right) \\
&\times \exp\left[j2\pi\Delta_t f_{r \max} \cos(\phi_r^{(s)} - \phi_{vr}) \cos\theta_r^{(s)} \cos\theta_{vr}\right] \\
&\times \exp\left(j2\pi\Delta_t f_{r \max} \sin\theta_r^{(s)} \sin\theta_{vr}\right) \\
&\times \exp\left[-8\left(\frac{\pi\sigma_h \sin\theta_t^{(i)}}{\lambda_c}\right)^2\right] I_0\left[8\left(\frac{\pi\sigma_h \sin\theta_t^{(i)}}{\lambda_c}\right)^2\right] \\
&\times \exp\left[-8\left(\frac{\pi\sigma_h \sin\theta_r^{(i)}}{\lambda_c}\right)^2\right] I_0\left[8\left(\frac{\pi\sigma_h \sin\theta_r^{(i)}}{\lambda_c}\right)^2\right] \\
&\times E\left[\sqrt{\frac{1}{\text{CPR}_{q\tilde{p},\tilde{q}\tilde{p}}}}\right] \left[\sqrt{G_a^{(v)}(\phi_t^{(s)}, \theta_t^{(s)})} \sqrt{G_a^{(h)}(\phi_t^{(s)}, \theta_t^{(s)})}\right] \\
&\times \begin{bmatrix} 1 & E\left[\sqrt{r_{p\tilde{q}}^{(m)}}\right] \\ E\left[\sqrt{r_{\tilde{p}q}^{(m)}}\right] & 1 \end{bmatrix} \begin{bmatrix} 1 & E\left[\sqrt{r_{p\tilde{q}}^{(n)}}\right] \\ E\left[\sqrt{r_{\tilde{p}q}^{(n)}}\right] & 1 \end{bmatrix} \\
&\times \left[\sqrt{G_b^{(v)}(\phi_r^{(s)}, \theta_r^{(s)})} \sqrt{G_b^{(h)}(\phi_r^{(s)}, \theta_r^{(s)})}\right] d\phi_r^{(s)} d\phi_t^{(s)} d\theta_r^{(s)} d\theta_t^{(s)} dR_r dR_t.
\end{aligned} \tag{58}$$

The TFCFs along the LOS path are written in forms as

$$\rho_{pq}^{\text{LOS}}(\Delta_t, \Delta_f) = \frac{A_m^2}{K+1} I_{\text{LOS}}(\Delta_t, \Delta_f), \tag{59}$$

where $I_{\text{LOS}}(\Delta_t, \Delta_f)$ is defined as

$$\begin{aligned}
I_{\text{LOS}}(\Delta_t, \Delta_f) &= K \exp\left(-j\frac{2\pi}{c}\Delta_f \epsilon_{pq}\right) \\
&\times \exp\left[j2\pi\Delta_t f_{t \max} \cos(\pi - \phi_r^{(\text{LOS})} - \phi_{vt}) \sin\theta_{vt}\right] \\
&\times \exp\left[j2\pi\Delta_t f_{r \max} \cos(\phi_r^{(\text{LOS})} - \phi_{vr}) \sin\theta_{vr}\right].
\end{aligned} \tag{60}$$

TABLE 1: The list of parameters used in the simulation.

Parameter	K	γ	$f_{t \max}$ [Hz]	$f_{r \max}$ [Hz]	σ_h [mm]
Value	0	3	100	100	0.2
Parameter	Δ_x [m]	Δ_y [m]	Δ_z [m]	f_c [GHz]	η_t
Value	1500	0	0	1.0	0.2
Parameter	θ_{vt}	θ_{vr}	ϕ_{vt}	ϕ_{vr}	η_r
Value	pi/4	pi/4	$\pi/4$	$\pi/4$	0.2
Parameter	XPD- μ	XPD- σ	CPR- μ	CPR- σ	η_{tr}
Value	10 dB	6 dB	0 dB	3 dB	0.6
V-V/H-H link					
Parameter	R_{t1} [m]	R_{t2} [m]	R_{r1} [m]	R_{r2} [m]	$\kappa_t^{(s)}$
Value	10	100	10	100	3
Parameter	$\kappa_r^{(s)}$	$\mu_t^{(s)}$	$\mu_r^{(s)}$	θ_{tm} [deg]	θ_{rm} [deg]
Value	3	$\pi/4$	$7\pi/4$	20	20
V-H/H-V link					
Parameter	R_{t1} [m]	R_{t2} [m]	R_{r1} [m]	R_{r2} [m]	$\kappa_t^{(s)}$
Value	10	100	10	100	3
Parameter	$\kappa_r^{(s)}$	$\mu_t^{(s)}$	$\mu_r^{(s)}$	θ_{tm} [deg]	θ_{rm} [deg]
Value	3	$\pi/4$	$7\pi/4$	20	20

Numerical integration methods are used to evaluate these TFCFs in the simulation analysis section.

4. Numerical Results and Analysis

In this section, we present numerical results associated with the analysis of the 2×2 DP-MIMO system. The matched polarization-basis time-frequency correlation functions are evaluated using the models described in Section 3. In the analysis, the propagation paths include LOS, SBT, SBR, and DB bounce paths, where the DB paths predominate over the SBT and SBR paths. The temporal dispersion is on the order of 600 ns, and the Doppler spread is approximately 200 Hz. The mean CP power ratio $\text{CPR}_{q\tilde{p},\tilde{q}\tilde{p}}$ is set to 0 dB so that the average powers of the V-V link and the H-H link are approximately identical, a condition that we recognize will not always hold in operational channels. Further, we also assume that the von Mises distributions for the azimuth angles and the cosine distributions for the elevation angles are equivalent for both H scatterers (reflecting horizontally polarized waves) and V scatterers (reflecting vertical polarized waves), and that the XPD's probability distribution functions are identical for the H-V and V-H components. As before, these are assumed for expediency. The specific simulation parameters are listed in Table 1. The center frequency is assumed to be 1 GHz.

Figures 5, 6, 7, 8, and 9 provide examples of joint TFCFs that were computed for specific subchannels and bounce path components. $\rho_{pq}^{\text{SBT}}(\Delta_t, \Delta_f)$, $\rho_{pq}^{\text{DB}}(\Delta_t, \Delta_f)$, and $\rho_{pq}(\Delta_t, \Delta_f)$ are shown for the V-V CP components in Figures 5, 6, and 7, respectively. Similarly, $\rho_{pq}^{\text{SBT}}(\Delta_t, \Delta_f)$ and $\rho_{pq}^{\text{DB}}(\Delta_t, \Delta_f)$ are shown in Figures 8, and 9 for the H-V link. The correlations along the Δt axis are driven by the Doppler frequency spread [35] and correlations along the Δf axis are driven by

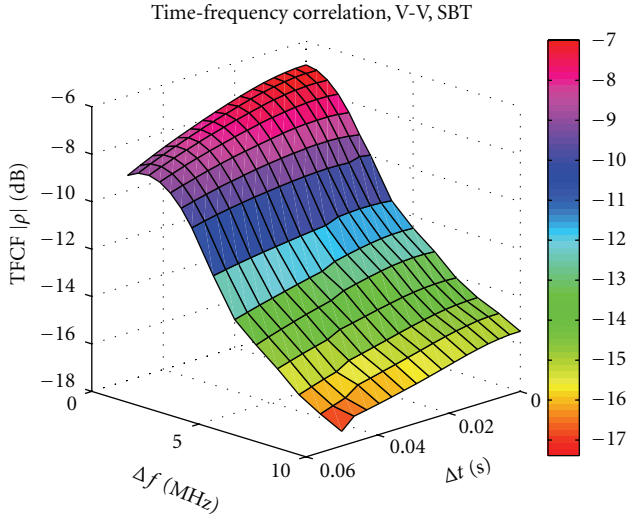


FIGURE 5: Normalized time-frequency correlation function of V-V link for SBT ray.

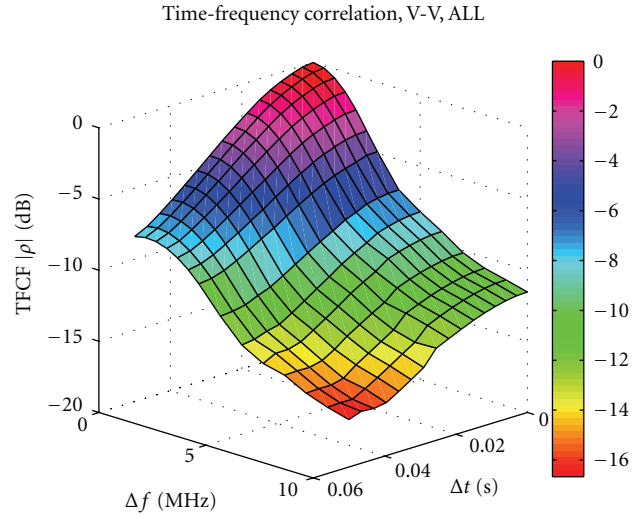


FIGURE 7: Normalized time frequency correlation function of V-V link for the superposition of SBT, SBR and DB rays.

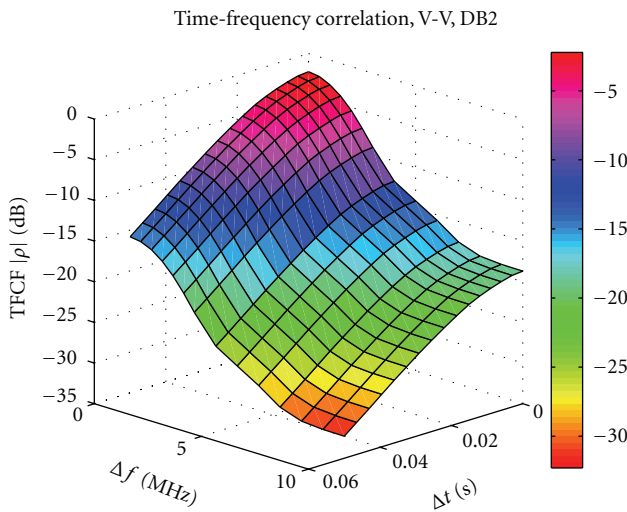


FIGURE 6: Normalized time frequency correlation function of V-V link for DB ray.

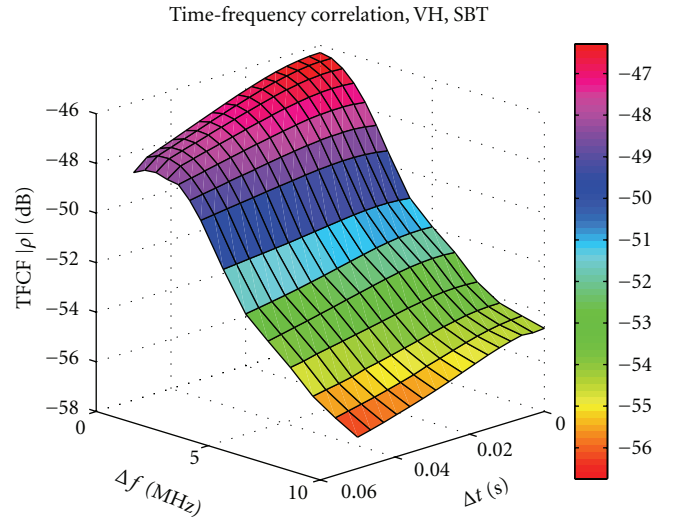


FIGURE 8: Normalized time-frequency correlation function of V-H link for SBT ray.

the delay spread associated with each component. The results indicate that the TFCFs are not separable into a product of a time correlation function and a frequency correlation function, a conclusion that we anticipated since the scatterer locations contribute to both the time dispersion and the Doppler spread. The peak correlation value at $\Delta t = \Delta f = 0$ in each plot is determined by the relative power of the paths being considered. The physical model parameters that play a role in generating temporal and Doppler spread include the radii R_{r1} , R_{r2} , R_{t1} , and R_{t2} associated with the Rx and Tx spheres of scatterers, the maximum elevation angles θ_{rm} and θ_{tm} , the mean value of the azimuth angles $\mu_r^{(s)}$ and $\mu_t^{(s)}$, the spread factor of scatterers $\kappa_r^{(s)}$ and $\kappa_t^{(s)}$, the angles defining the direction of the velocity, θ_{vr} , ϕ_{vr} , θ_{vt} , and ϕ_{vt} , and the maximum Doppler frequencies $f_{r\max}$ and $f_{t\max}$.

Frequency correlation functions (for a fixed Δt) are driven primarily by the delay profile of the channel. Small delay profiles yield frequency correlation functions that decorrelate at higher frequencies. The DB component will exhibit the lowest decorrelation frequency since this component has the most significant delay spread. In the concentric-sphere based scattering model shown in Figure 1, the maximum delay spread is determined by the maximum distance of signal traveling along the double-bounce path induced by the Tx scatterer or the Rx scatterer. It can be roughly calculated as $(2R_t + 2R_r)/c$, where c is the speed of light. The coherence bandwidth W_c in Hz is given approximately by the inverse proportion of the time delay spread τ_d . The minimum coherence bandwidths versus the radii of the Tx and Rx spheres used in the channel model are estimated and presented in Figures

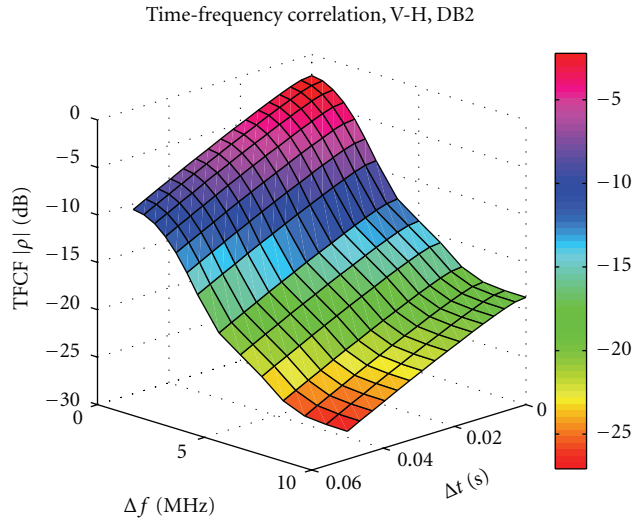


FIGURE 9: Normalized time-frequency correlation function of V-H link for DB ray.

11 and 12. The coherence bandwidth decreases when the radii of the Tx or Rx spheres increase. In Figure 7, if we approximate the coherence bandwidth as the frequency separation over which the magnitude of correlation coefficients is larger than a half of the its maximum at the zero frequency separation, the coherence bandwidth for the test profile used in our analysis is approximately 2.5 MHz.

The time correlation function dependencies on the maximum Doppler frequency are illustrated for the double-bounce ray with $\Delta f = 0$, in Figure 10. Large Doppler frequencies lead to small decorrelation times. We anticipate that the double-bounce components will decorrelate at least as quickly as the single-bounce components due to the fact that the Doppler spread of this component will be greater than or equal to the Doppler spread of the SBT component, a trend that is confirmed in Figures 8 and 9.

The use of non-zero XPD values leads to cross-polarized components (V-H and H-V) with power contributions lower than the CP components (V-V or H-H). Due to the similarity of parameters used to define the co- and crosspolarized channels, the cross-polarized response is approximately related to the CP ones by a scale factor. This result can be observed from cross-polarized parts of TFCFs in Section 3. The normalized correlation values for the SBT and DB components at $\Delta f = \Delta t = 0$ are plotted as a function of the mean XPD value μ for both matched polarization and cross polarization components in Figure 13. The normalized correlation values for the matched polarizations are constant since the correlations and powers are independent of μ . For the crosspolarization components, the normalized correlation is seen to decrease as μ increases, largely due to changes in relative power. At $\mu = 0$, when the scatterers yield the same average power at both matched and cross-polarized components, the normalized correlation is identical for both the matched and cross-polarization links.

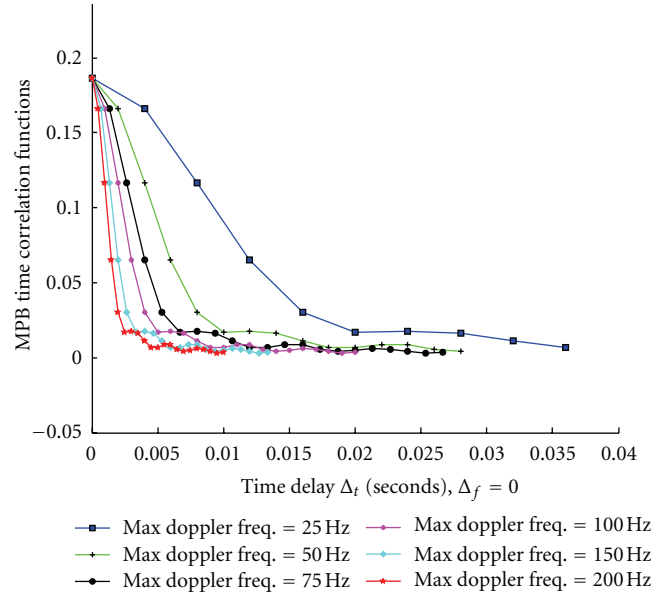


FIGURE 10: Normalized time-correlation functions varying with the time delay and the maximum Doppler Tx/Rx frequencies for DB ray. The configuration is defined in Table 1 with $\eta_t = \eta_r = \eta_{tr} = 1/3$.

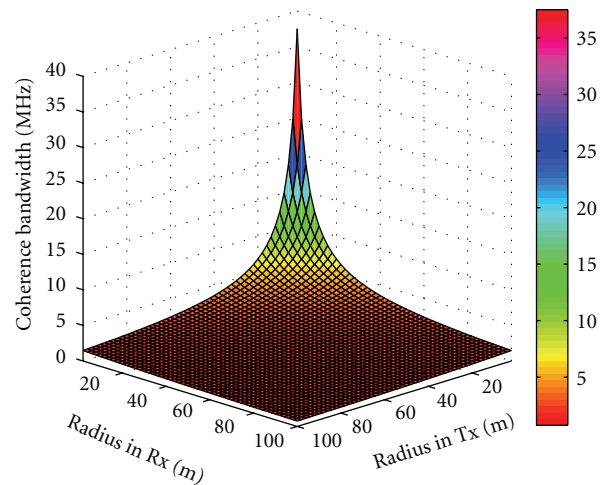


FIGURE 11: The minimum coherence bandwidth of 2×2 DP system varies with upper radii of spheres of Tx and Rx scatterers respectively.

5. Conclusion

In this paper, a 3D geometrical propagation model has been proposed for DP-MIMO mobile-to-mobile Rayleigh and Rician fading channels. The parametric channel model incorporates a number of physical parameters to characterize the channel, including antenna patterns, azimuth/elevation angles of arrival and departure, geometrical distribution of scatterers, K-factor, the maximum Doppler frequency, scattering loss factor, crosspolar discrimination, and copolarization power ratio. Using the key parameters of the model,

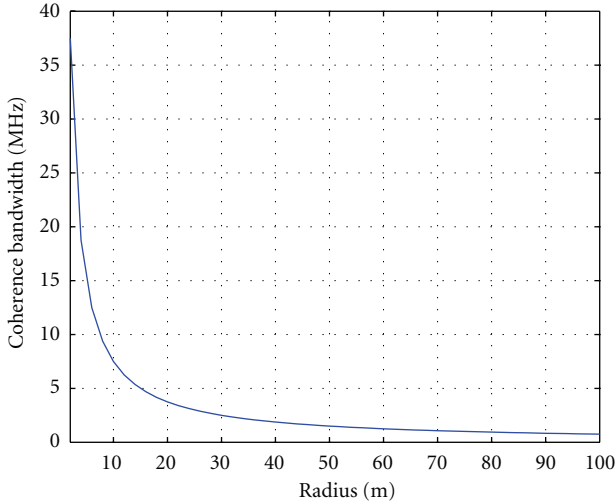


FIGURE 12: The minimum coherence bandwidth of 2×2 DP system varies with upper radii of spheres of scatterers in both Tx and Rx.

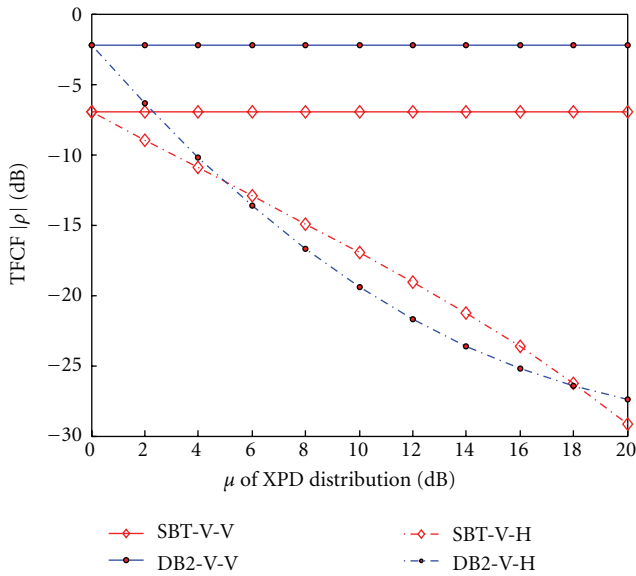


FIGURE 13: Normalized time-correlation functions of SBT and DB rays vary with the mean XPD μ and the configuration is set up in Table 1.

matched polarization-basis time-frequency correlation functions were formulated and numerically computed for WSSUS 3D non-isotropic scattering environments. The numerical results show that the joint TFCFs are not separable into independent time-correlation and frequency-correlation functions. The normalized TFCFs can be parsed into bounce path components for matched polarization and copolarization links, leading to power-normalized marginal TFCFs for the channel realization. The flexibility of the model enables control of channel parameters to achieve a variety of multipath fading environments to investigate 2×2 DP architectures.

Our intention in future research is to validate the proposed channel model using measurements. A series of experiments are planned to verify and justify our model.

Disclaimer

The views and conclusions contained in this paper are those of the authors and should not be interpreted as representing the official policies, either expressed or implied, of the Office of Naval Research or the U. S. Government.

Acknowledgment

This work was sponsored by the office of Naval Research under grant number N00014-11-1-0607.

References

- [1] A. J. Paulraj and T. Kailath, "Increasing capacity in wireless broadcast systems using distributed transmission/directional reception (dtdr)," US Patent 5, 345, 599, 1994.
- [2] G. J. Foschini and M. J. Gans, "On limits of wireless communications in a fading environment when using multiple antennas," *Wireless Personal Communications*, vol. 6, no. 3, pp. 311–335, 1998.
- [3] D. Tse and P. Viswanath, *Fundamentals of Wireless Communication*, Cambridge University Press, 2005.
- [4] C. Oestges, V. Erceg, and A. J. Paulraj, "Propagation modeling of MIMO multipolarized fixed wireless channels," *IEEE Transactions on Vehicular Technology*, vol. 53, no. 3, pp. 644–654, 2004.
- [5] N. W. Bikhazi, *MIMO communication capacity: antenna coupling and precoding for incoherent detection [Ph.D. thesis]*, CiteSeer, 2006.
- [6] P. Soma, D. S. Baum, V. Erceg, R. Krishnamoorthy, and A. J. Paulraj, "Analysis and modeling of Multiple-Input Multiple-Output (MIMO) radio channel based on outdoor measurements conducted at 2.5GHz for fixed BWA applications," in *Proceedings of the IEEE International Conference on Communications (ICC '02)*, vol. 1, pp. 272–276, May 2002.
- [7] M. Shafi, M. Zhang, A. L. Moustakas et al., "Polarized MIMO channels in 3-D: models, measurements and mutual information," *IEEE Journal on Selected Areas in Communications*, vol. 24, no. 3, pp. 514–526, 2006.
- [8] R. G. Vaughan, "Polarization diversity in mobile communications," *IEEE Transactions on Vehicular Technology*, vol. 39, no. 3, pp. 177–186, 1990.
- [9] P. Kyritsi, D. C. Cox, R. A. Valenzuela, and P. W. Wolniansky, "Effect of antenna polarization on the capacity of a multiple element system in an indoor environment," *IEEE Journal on Selected Areas in Communications*, vol. 20, no. 6, pp. 1227–1239, 2002.
- [10] T. B. Sorensen, A. O. Nielsen, P. E. Mogensen, M. Tolstrup, and K. Steffensen, "Performance of two-branch polarization antenna diversity in an operational GSM network," in *Proceedings of the 48th IEEE Vehicular Technology Conference (VTC '98)*, vol. 3, pp. 741–746, May 1998.
- [11] T. Neubauer and P. C. F. Eggers, "Simultaneous characterization of polarization matrix components in pico cells," in *Proceedings of the IEEE VTS 50th Vehicular Technology Conference (VTC '99)*, vol. 3, pp. 1361–1365, September 1999.

- [12] T. G. Pratt, H. Tapse, B. Walkenhorst, and G. Acosta-Marum, "A modified XPC characterization for polarimetric channels," *IEEE Transactions on Vehicular Technology*, vol. 60, no. 7, Article ID 5871726, pp. 2904–2913, 2011.
- [13] P. Hoeher, "Statistical discrete-time model for the WSSUS multipath channel," *IEEE Transactions on Vehicular Technology*, vol. 41, no. 4, pp. 461–468, 1992.
- [14] E. Chiavaccini and G. M. Vitetta, "GQR models for multipath rayleigh fading channels," *IEEE Journal on Selected Areas in Communications*, vol. 19, no. 6, pp. 1009–1018, 2001.
- [15] C. Oestges, B. Clerckx, M. Guillaud, and M. Debbah, "Dual-polarized wireless communications: from propagation models to system performance evaluation," *IEEE Transactions on Wireless Communications*, vol. 7, no. 10, pp. 4019–4031, 2008.
- [16] M. Shafiq, M. Zhang, P. J. Smith, A. L. Moustakas, and A. F. Molisch, "The impact of elevation angle on MIMO capacity," in *Proceedings of the IEEE International Conference on Communications (ICC '06)*, vol. 9, pp. 4155–4160, July 2006.
- [17] T. R. ETSI, "125 996 v. 6.1. 0, universal mobile telecommunications system (umts); spatial channel model for multiple input multiple output (mimo) simulations (3gpp tr 25.996 version 6.1. 0 release 6)," Further study is required to design an adaptive or hybrid MCN structure to improve both the handover efficiency and the throughput of cell-edge and cell-boundary users and to resolve the network issues, 2003.
- [18] A. G. Zajić and G. L. Stüber, "Three-dimensional modeling and simulation of wideband MIMO mobile-to-mobile channels," *IEEE Transactions on Wireless Communications*, vol. 8, no. 3, pp. 1260–1275, 2009.
- [19] M. T. Dao, V. A. Nguyen, Y. T. Im, S. O. Park, and G. Yoon, "3D polarized channel modeling and performance comparison of MIMO antenna configurations with different polarizations," *IEEE Transactions on Antennas and Propagation*, vol. 59, no. 7, pp. 2672–2682, 2011.
- [20] R. Wang and D. Cox, "Channel modeling for Ad Hoc mobile wireless networks," in *Proceedings of the 55th Vehicular Technology Conference (VTC '02)*, vol. 1, pp. 21–25, May 2002.
- [21] C. S. Patel, G. L. Stüber, and T. G. Pratt, "Simulation of Rayleigh-faded mobile-to-mobile communication channels," *IEEE Transactions on Communications*, vol. 53, no. 11, pp. 1876–1884, 2005.
- [22] J. Maurer, T. Fügen, and W. Wiesbeck, "Narrow-band measurement and analysis of the inter-vehicle transmission channel at 5.2 GHz," in *Proceedings of the 55th Vehicular Technology Conference (VTC '02)*, vol. 3, pp. 1274–1278, May 2002.
- [23] Y. I. Wu and K. T. Wong, "Polarisation-sensitive geometric modelling of the distribution of direction-of-arrival for uplink multipaths," *IET Microwaves, Antennas and Propagation*, vol. 5, no. 1, pp. 95–101, 2011.
- [24] J. D. Kraus and R. J. Marhefka, *Antennas for All Applications*, vol. 1, McGraw-Hill, New York, NY, USA, 2002.
- [25] H. L. Van Trees, *Detection, Estimation, and Modulation Theory: Detection, Estimation, and Linear Modulation Theory*, Wiley, 1968.
- [26] J. D. Parsons and P. J. D. Parsons, *The Mobile Radio Propagation Channel*, vol. 81, Wiley, 2000.
- [27] K. Mammassis, R. W. Stewart, and J. S. Thompson, "Spatial Fading Correlation model using mixtures of von Mises Fisher distributions," *IEEE Transactions on Wireless Communications*, vol. 8, no. 4, pp. 2046–2055, 2009.
- [28] E. J. Gumbel, "Applications of the circular normal distribution," *JAMA*, vol. 49, no. 266, pp. 267–297, 1954.
- [29] J. D. Parsons and A. M. D. Turkmani, "Characterisation of mobile radio signals. Model description," *IEE Proceedings, Part I*, vol. 138, no. 6, pp. 549–556, 1991.
- [30] T. Taga, "Analysis for mean effective gain of mobile antennas in land mobile radio environments," *IEEE Transactions on Vehicular Technology*, vol. 39, no. 2, pp. 117–131, 1990.
- [31] P. Kyritsis and D. C. Cox, "Propagation characteristics of horizontally and vertically polarized electric fields in an indoor environment: simple model and results," in *Proceedings of the IEEE 54th Vehicular Technology Conference (VTC '01)*, vol. 3, pp. 1422–1426, October 2001.
- [32] L. Boithias and L. J. Libols, *Radio Wave Propagation*, North Oxfordshire Academy, London, UK, 1987.
- [33] J. G. Proakis, *Digital Communications*, McGraw-Hill, New York, NY, USA, 2001.
- [34] J. M. Wozencraft and I. M. Jacobs, *Principles of Communication Engineering*, vol. 32, Wiley, New York, NY, USA, 1965.
- [35] T. S. Rappaport et al., *Wireless Communications: Principles and Practice*, Prentice Hall, Upper Saddle River, NJ, USA, 1996.

Research Article

An Accurate Hardware Sum-of-Cisoids Fading Channel Simulator for Isotropic and Non-Isotropic Mobile Radio Environments

L. Vela-Garcia,¹ J. Vázquez Castillo,¹ R. Parra-Michel,¹ and Matthias Pätzold²

¹Department of Telecommunications, CINVESTAV I.P.N., 45019 Zapopan, JAL, Mexico

²Faculty of Engineering and Science, University of Agder, P.O. Box 509, 4898 Grimstad, Norway

Correspondence should be addressed to J. Vázquez Castillo, jvazquezc@gdl.cinvestav.mx

Received 27 April 2012; Revised 13 July 2012; Accepted 27 July 2012

Academic Editor: Carlos A. Gutierrez

Copyright © 2012 L. Vela-Garcia et al. This is an open access article distributed under the Creative Commons Attribution License, which permits unrestricted use, distribution, and reproduction in any medium, provided the original work is properly cited.

The rapid technological development in the field of wireless communications calls for devices capable of reproducing and simulating the behavior of the channel under realistic propagation conditions. This paper presents a hardware fading channel simulator that is able to generate stochastic processes characterized by symmetrical and asymmetrical Doppler power spectral densities (PSDs) depending on the assumption of isotropic or non-isotropic scattering. The concept of the proposed hardware simulator is based on an implementation of the sum-of-cisoids (SOC) method. The hardware simulator is capable of handling any configuration of the cisoid's amplitudes, frequencies, and phases. Each of the cisoids that constitutes the SOC model is implemented using a piecewise polynomial approximation technique. The investigation of the higher-order statistics of the generated fading processes, like the level-crossing rate (LCR) and the average duration of fades (ADF), shows that our design is able to reproduce accurately the key features of realistic channel models that are considered as candidates for the latest wireless communication standards.

1. Introduction

The increasing demand for high data rate wireless communication systems makes it mandatory to develop devices enabling the test and the performance evaluation of such systems with a high level of accuracy. A channel simulator offers the possibility of reproducing the most important channel characteristics without the necessity of conducting field tests in specific environments, which reduces significantly the system development time and the costs of the system design and the verification process.

Flat-fading wireless channels are modeled in the complex baseband as complex stochastic processes characterized by a specific autocorrelation function (ACF) or, alternatively, by the corresponding power spectral density (PSD). Considering a base station to mobile link, these functions are related to the angle-of-arrival (AOA) distribution of the incoming plane waves (in the mobile to base station link, the angle-of-departure (AOD) distribution determines the ACF and PSD) in a multipath propagation environment

[1]. The uniform distribution of the AOA (i.e., the uniform AOA probability density function (PDF) over $[-\pi, \pi)$) is related to environments characterized by isotropic scattering conditions, where the ACF is determined by the zeroth-order Bessel function corresponding to the Jakes PSD [2]. This model was originally proposed by Clarke [3]. However, realistic propagation environments do not fulfill the isotropic scattering conditions, which result in a nonuniform distribution of the AOA, leading to an asymmetrical PSD that can exhibit a variety of shapes (see [4–8] for more details).

For the reproduction of the statistical properties of real mobile radio channels on hardware platforms, several channel emulators have been proposed in the literature (see [9–11]), where the fading samples have been generated by one of the following two methods: the filter method or the sum-of-sinusoids (SOS) method. In most cases, the generation of the fading waveforms has been accomplished under the assumption of isotropic scattering. In [11], a hardware channel simulator based on the filter method

assuming non-isotropic scattering conditions is presented. However, the level of computational complexity in filter-based emulators is greater than in SOS-based emulators, as SOS techniques do not require the realization of white Gaussian random number generators (see [12]). Therefore, SOS-based simulators provide an attractive alternative because of their computational efficiency and comfortable reconfiguration capabilities.

In this paper, a novel architecture for generating stochastic processes using the SOS principle is presented. The challenge of this study is to develop a simulator, which is able to handle both symmetrical and asymmetrical PSDs in a parametric architecture, allowing the emulation of more realistic channels, which are required in modern wireless communication standards. In order to achieve this, the sum-of-cisoids (SOC) method rather than the SOS approach will be used as proposed in [1]. The resulting hardware architecture allows the implementation of any SOC or SOS simulation model, permitting the configuration of the gains, frequencies, and phases of each complex sinusoid for any chosen deterministic or stochastic parameter computation method. In addition, this provides the methodological flexibility for adding specular and non-specular components. The sinusoid evaluation is performed using a piecewise polynomial approximation, to enable the generation of sinusoid samples at high rates with a high frequency resolution of less than 1 Hz, which is desired for the development of modern emulators based on the SOS/SOC principle. From this perspective, the polynomial approximation technique is employed here as a high-performance alternative to the direct sinusoid computation method, which is essential for traditional architectures using look-up tables (LUT) that are described in [9, 10].

The rest of this article is organized as follows. In Section 2, a brief description of the SOC method is given. The hardware architecture of a flat-fading simulator is described in Section 3. In Section 4, the study of two methods for computing the SOC parameters is provided. In Section 5, the statistical properties of the fading samples generated by the proposed hardware architecture are discussed. This is followed by the performance analysis in Section 6, which elaborates on the hardware resource costs of the proposed architecture in comparison to other existing SOS-based simulators. Finally, the conclusions are drawn in Section 7.

2. Review of the SOC Model

In this section, a brief description of the SOC model for the generation of stochastic processes is presented. Additionally, mathematical expressions for the first and second order statistics of the SOC model are reviewed, which provides a reference for comparing several given PSD functions with the corresponding approximation results obtained for the proposed flat-fading channel simulator.

2.1. Basic Description of SOC Models. In the complex equivalent baseband, a multipath flat-fading channel can be

modeled by an SOC process $\hat{\mu}(t)$, which is a superposition of N cisoids of the form:

$$\hat{\mu}(t) = \sum_{n=1}^N c_n e^{j(2\pi f_n t + \theta_n)}, \quad (1)$$

where c_n , f_n , and θ_n are the gains, the Doppler frequencies, and the phases of the n th propagation path, respectively. Considering that c_n and f_n are constants, and only θ_n are independent, identically distributed (i.i.d.) random variables with a uniform distribution over $[0, 2\pi)$, then $\hat{\mu}(t)$ is a zero-mean complex stochastic process with variance $\sigma_{\hat{\mu}}^2 = \sum_{n=1}^N c_n^2$ [1]. Under certain conditions, it can be shown [13] that the SOC process $\hat{\mu}(t)$ tends to a complex Gaussian process $\mu(t)$ with variance $2\sigma_0^2$ if $N \rightarrow \infty$.

Let the line-of-sight (LOS) component be given by [1]

$$s = \rho e^{j\theta_\rho}, \quad (2)$$

where the amplitude $\rho \geq 0$ and the phase θ_ρ are constant quantities, then the sum of the scattered components $\hat{\mu}(t)$ and the LOS component s results in the following nonzero-mean complex random process:

$$\hat{\mu}_\rho(t) = \hat{\mu}(t) + s. \quad (3)$$

The envelope of $\hat{\mu}_\rho(t)$, which is denoted by

$$\hat{\xi}(t) = \left| \hat{\mu}_\rho(t) \right|, \quad (4)$$

provides an accurate and efficient simulation model for Rice processes.

2.2. Statistical Properties of SOC Models. In [13], it has been shown that the PDF $p_{\hat{\xi}}(r)$ of $\hat{\xi}(t)$ is given by

$$p_{\hat{\xi}}(r) = r(2\pi)^2 \int_0^\infty \left[\prod_{n=1}^N J_0(2\pi|c_n|x) \right] J_0(2\pi r x) J_0(2\pi \rho x) x dx, \quad r \geq 0, \quad (5)$$

where $J_0(\cdot)$ denotes the 0th order Bessel function of the first kind. If the gains c_n are given by $c_n = \sigma_0 \sqrt{2/N}$, then the PDF in (5) tends to the Rice density

$$p_{\hat{\xi}}(r) = \frac{r}{\sigma_0^2} e^{-(r^2 + \rho^2)/2\sigma_0^2} I_0\left(\frac{r\rho}{\sigma_0^2}\right), \quad r \geq 0 \quad (6)$$

as $N \rightarrow \infty$, where $I_0(\cdot)$ is the 0th order-modified Bessel function of the first kind.

Likewise, the cumulative distribution function (CDF) $P_{\hat{\xi}}(r)$ of $\hat{\xi}(t)$ has been derived in [14], where the following result can be found:

$$P_{\hat{\xi}}(r) = 2\pi r \int_0^\infty \left[\prod_{n=1}^N J_0(2\pi|c_n|x) \right] J_1(2\pi r x) J_0(2\pi \rho x) dx, \quad r \geq 0. \quad (7)$$

In a similar fashion, the CDF $P_{\hat{\xi}}(r)$ of $\hat{\xi}(t)$ converges to the Rice CDF as $N \rightarrow \infty$ [1, 14]. The Rice CDF $P_{\xi}(r)$ can be expressed as

$$P_{\xi}(r) = 1 - M_Q\left(\frac{\rho}{\sigma_0}, \frac{r}{\sigma_0}\right), \quad r \geq 0, \quad (8)$$

where $M_Q(\cdot, \cdot)$ represents the Marcum Q-function [1].

Owing to the fact that the PDF and the CDF do not reveal any information about how fast the channel changes with time, it is necessary to consider the second-order statistics of the envelope $\hat{\xi}(t)$. In this respect, the level-crossing rate (LCR) and average duration of fades (ADF) are of special interest. The LCR $N_{\hat{\xi}}(r)$ describes how often the envelope $\hat{\xi}(t)$ crosses on average a specified signal level r within one second, and the ADF $T_{\hat{\xi}}(r)$ describes how long on average the envelope $\hat{\xi}(t)$ remains below a specified signal level r . These statistical quantities depend on the propagation environment and the Doppler shifts caused by the movement of the mobile station. The LCR $N_{\hat{\xi}}(r)$ of $\hat{\xi}(t)$ can be obtained by using Rice's formula [15, 16]:

$$N_{\hat{\xi}}(r) = \int_0^{\infty} \dot{z} p_{\hat{\xi}\dot{\hat{\xi}}}(r, \dot{z}) d\dot{z}, \quad r \geq 0. \quad (9)$$

Equation (9) requires the knowledge of the joint PDF $p_{\hat{\xi}\dot{\hat{\xi}}}(z, \dot{z})$ of the envelope $\hat{\xi}(t)$ and its time derivative $\dot{\hat{\xi}}(t)$. It should be mentioned that the relation in (9) holds for any stationary random process characterized by the joint PDF $p_{\hat{\xi}\dot{\hat{\xi}}}(z, \dot{z})$.

In [17], an exact solution has been presented for the LCR $N_{\hat{\xi}}(r)$ of the envelope $\hat{\xi}(t)$. This exact-solution factors in that the inphase and quadrature components of the SOC process $\hat{\mu}(t)$ as well as their time derivatives are mutually correlated. The LCR $N_{\hat{\xi}}(r)$ of $\hat{\xi}(t)$ in (4) is given as

$$\begin{aligned} N_{\hat{\xi}}(r) &= 4\pi r \int_0^{\dot{z}_{\max}} \dot{z} \int_0^{\infty} \int_0^{\infty} \int_0^{2\pi} J_0(2\pi\rho\nu_1) \\ &\times \left[\prod_{n=1}^N J_0\left(2\pi c_n \sqrt{\nu_1^2 + (2\pi f_n \nu_2)^2} - 4\pi f_n \nu_1 \nu_2 \sin \theta\right) \right] \\ &\times e^{-j2\pi r \nu_1 \cos(\theta)} e^{-j2\pi \dot{z} \nu_2} \nu_1 d\theta d\nu_1 d\nu_2 d\dot{z}, \quad r \geq 0, \end{aligned} \quad (10)$$

where \dot{z}_{\max} denotes the maximum of $\dot{\hat{\xi}}(t)$, which is given by $\dot{z}_{\max} = \max\{\dot{\hat{\xi}}(t)\} = 2\pi \sum_{n=1}^N |f_n c_n|$. The LCR $N_{\hat{\xi}}(r)$ of SOC processes $\hat{\xi}(t)$ approaches the LCR $N_{\xi}(r)$ of Rice processes $\xi(t)$ as $N \rightarrow \infty$, that is,

$$\lim_{N \rightarrow \infty} N_{\hat{\xi}}(r) = N_{\xi}(r) = \sqrt{\frac{\beta}{2\pi}} p_{\xi}(r), \quad r \geq 0, \quad (11)$$

where $p_{\xi}(r)$ is the Rice PDF presented in (6). The symbol β represents the negative curvature of the ACF $r_{\mu_i \mu_i}(\tau)$ of the underlying real-valued Gaussian process $\mu_i(t)$ ($i = 1, 2$) at

the origin $\tau = 0$. In case of isotropic scattering, the quantity β is given by $\beta = 2(\pi f_{\max} \sigma_0)^2$ [1].

The corresponding ADF $T_{\hat{\xi}}(r)$ of $\hat{\xi}(t)$ can be obtained after substituting (7) and (10) in

$$T_{\hat{\xi}}(r) = \frac{P_{\hat{\xi}}(r)}{N_{\hat{\xi}}(r)}. \quad (12)$$

From the discussion above, it is obvious that the ADF $T_{\hat{\xi}}(r)$ of $\hat{\xi}(t)$ converges to the ADF $T_{\xi}(r)$ of Rice processes $\xi(t)$ as $N \rightarrow \infty$.

In addition to the symmetrical Jakes PSD:

$$S_{\hat{\mu}}^{\text{Jakes}}(f) = \begin{cases} \frac{\sigma_0^2}{\pi f_{\max} \sqrt{1 - (f/f_{\max})^2}}, & |f| \leq f_{\max} \\ 0, & |f| > f_{\max} \end{cases} \quad (13)$$

which characterizes isotropic scattering environments, it is desirable to have a fading channel simulator that is able to generate fading process characterized by both symmetrical and asymmetrical PSDs.

In this sense, the proposed fading channel simulator shall also incorporate the characteristics of non-isotropic scattering environments. The utility of the von Mises PDF as a parametric model for the distribution of the AOA has been supported by different studies focussing non-isotropic propagation scenarios [18]. The resulting PSD includes the symmetrical Jakes PSD as a special case. In our study, the Doppler PSD obtained by using the von Mises AOA distribution will be used as a *reference model* for the PSD of non-isotropic scattering environments.

When using the von Mises AOA distribution, then the Doppler PSD can be written as follows [19]

$$\begin{aligned} S_{\mu}^{\text{VM}}(f) &= \frac{\exp(\kappa \cos(\alpha_0)(f/f_{\max})) \cosh\left(\kappa \sin(\alpha_0) \sqrt{1 - (f/f_{\max})^2}\right)}{\pi f_{\max} I_0(\kappa) \sqrt{1 - (f/f_{\max})^2}}, \\ &|f| \leq f_{\max}, \end{aligned} \quad (14)$$

where $\kappa \geq 0$ is a concentration parameter, which controls the angular spread of the AOA, and α_0 denotes the mean AOA of the incoming plane waves. Equation (14) assumes that the PDF of the AOA follows the von Mises distribution defined by

$$p_{\alpha}^{\text{VM}}(\alpha) = \frac{\exp[\kappa \cos(\alpha - \alpha_0)]}{2\pi I_0(\kappa)}, \quad \alpha \in [-\pi, \pi]. \quad (15)$$

According to [19], the LCR of Rayleigh processes $\xi(t)$ assuming the von Mises AOA distribution can be written as

$$\begin{aligned} N_{\xi}^{\text{VM}}(r) &= \frac{\sqrt{I_0^2(\kappa) - I_1^2(\kappa) + \cos(2\alpha_0)[I_0(\kappa)I_2(\kappa) - I_1^2(\kappa)]}}{I_0(\kappa)} \\ &\times \sqrt{2\pi} f_{\max} r \exp(-r^2), \end{aligned} \quad (16)$$

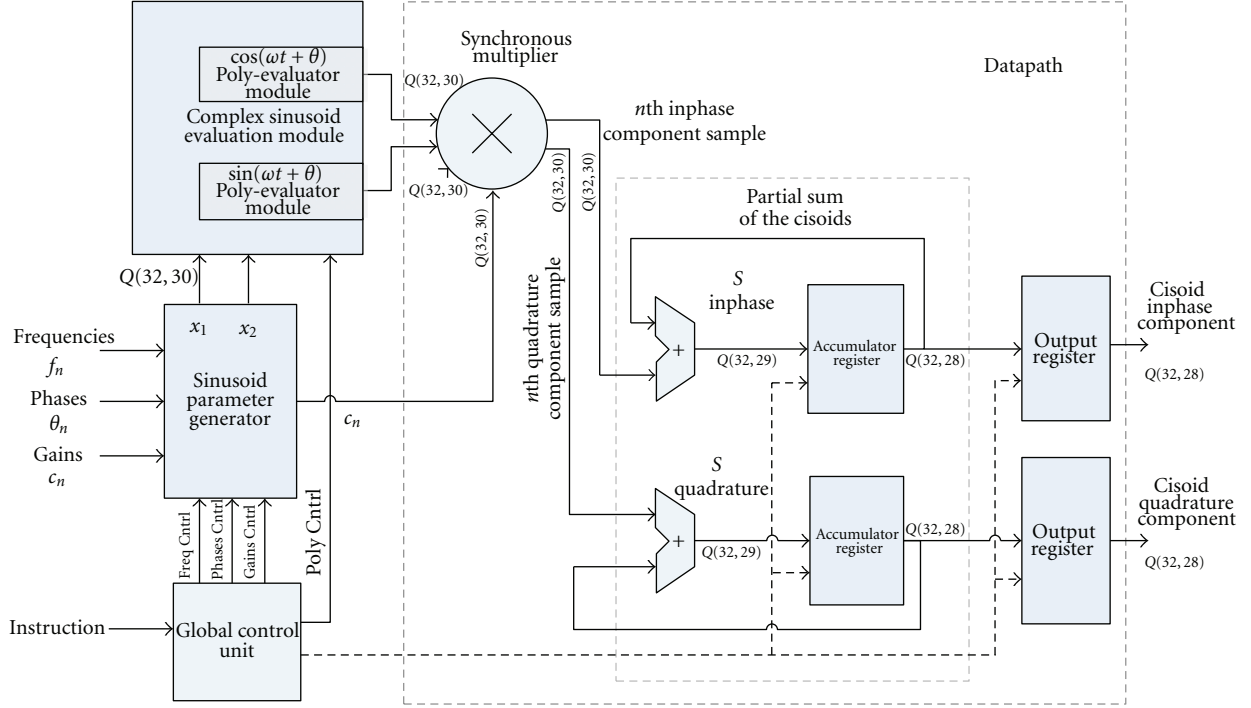


FIGURE 1: General architecture of the SOC fading channel simulator.

and the corresponding ADF is given by

$$T_{\xi}^{VM}(r) = \frac{I_0(\kappa)}{\sqrt{I_0^2(\kappa) - I_1^2(\kappa) + \cos(2\alpha_0)[I_0(\kappa)I_2(\kappa) - I_1^2(\kappa)]}} \times \frac{\exp(r^2) - 1}{\sqrt{2\pi} f_{\max} r}. \quad (17)$$

For the case of isotropic scattering ($\kappa = 0$), the expression in (16) reduces to the LCR $N_{\xi}(r) = \sqrt{2\pi} f_{\max} r \exp(-r^2)$, and the ADF in (17) simplifies to $T_{\xi}(r) = (\exp(r^2) - 1)/(\sqrt{2\pi} f_{\max} r)$.

3. Hardware Architecture

In this section, the hardware channel simulator based on the SOC method is presented for both isotropic and non-isotropic scattering environments. The general architecture of the proposed SOC fading channel simulator is illustrated in Figure 1. The datapath of the architecture is drawn by using the notation $Q(WL, WF)$, where WL represents the datapath wordlength, and WF denotes the fractional part of the wordlength. The SOC fading channel simulator design is composed of four main modules: the complex sinusoid evaluation module, the sinusoid parameter generator, the global control unit, and the datapath.

In order to compute the SOC according to (1), the proposed fading channel simulator requires the initialization of the SOC parameters (c_n, f_n, θ_n), as well as the number of cisoids N , which are stored in the sinusoid parameter generator. Once the simulator has been configured, the complex sinusoid evaluation module computes the n th cisoid

by $\exp(jx_1)$ if a positive Doppler frequency is provided. Otherwise, $\exp(jx_2)$ is computed for the case of a negative Doppler frequency, where $x_1 = 2\pi f_n t + \theta_n$ and $x_2 = -(2\pi f_n t) + \theta_n$. This fact is obvious due to the following relation:

$$\exp(\pm j\omega t) = \cos(\omega t) \pm j \sin(\omega t). \quad (18)$$

Once the corresponding n th cisoid has been determined, it is multiplied by the gain c_n before accumulating the resultant value in the accumulator register blocks, as shown in Figure 1.

The summation of the cisoids as well as the initialization of the SOC parameters of the simulator are handled by the global control unit. It is important to point out that the proposed architecture is parametric in the sense that it is independent of the number of cisoids N and the choice of the model parameters (f_n, c_n , and θ_n).

3.1. Piecewise Polynomial Approximation Technique. In case of the SOS method, the most common hardware implementation technique described in the literature for the evaluation of cosine and sine functions is the one that utilizes LUT. The main characteristic of this technique is that it uses memory blocks for storing the sinusoids. However, the use of LUT limits the evaluation of the SOS process when covering a wide range of Doppler frequencies at high data rates (i.e., Doppler frequencies in the range from mHz up to kHz at megasamples per second (MSPS)). This limitation is due to the limited number of samples that can be stored in block memories for generating the sinusoids with the lower Doppler frequencies. For example, for the generation of

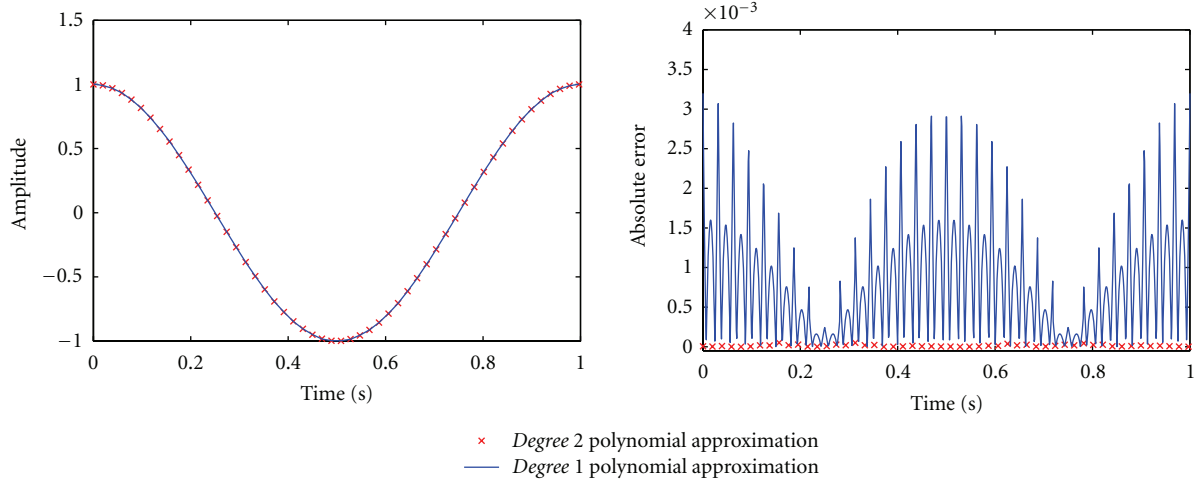


FIGURE 2: Approximation of a cosine function with *degree 1* and *degree 2* polynomials.

a sinusoid with a Doppler frequency of 1 kHz at 1 MSPS, it is necessary to store 1000 samples in a memory table. On the other hand, in order to generate a sinusoid with a Doppler frequency of 0.1 Hz at 1 MSPS, it is required to store 10 megasamples in the LUT. Techniques for saving memory resources are described in the literature (see [20] for more details). It is important to remark that the waveform with the lowest Doppler frequency generated by the sinusoid generator determines the frequency resolution that can be achieved by using LUT. This implies that huge memories are required in order to obtain a high frequency resolution. As a consequence, the ACF of the generated SOC process depends directly on the accuracy of the Doppler frequencies of the generated complex sinusoids. Likewise, higher-order statistics, such as the LCR and ADF, can be affected as a result of the level of accuracy in the generated waveforms [21].

An alternative solution that avoids the limitations imposed by LUT is provided by using a piecewise polynomial approximation technique for the sinusoid generation. This technique rests upon the approximation of a function $f(x)$, which is in our case a sine or cosine function, by means of the evaluation of polynomials $p^*(x)$, which are defined by the polynomial degree d and the type of segmentation. The type of segmentation defines the number of intervals j and the bounds of such intervals $[a_j, b_j]$. Each polynomial is defined as follows:

$$p^*(x) = p_d^*x^d + p_{d-1}^*x^{d-1} + \dots + p_1^*x + p_0^*. \quad (19)$$

An efficient procedure to evaluate the polynomials $p^*(x)$ is by employing Horner's rule as follows:

$$p^*(x) = ((p_d^*x + p_{d-1}^*)x + \dots)x + p_0^*, \quad (20)$$

where x is the polynomial input, and p_k^* ($k = 0, 1, \dots, d$) are the polynomial coefficients.

In order to obtain the coefficients p_k^* ($k = 0, 1, \dots, d$), two kinds of approximation techniques can be employed, namely, the approximation technique that minimizes the least square

error between $f(x)$ and $p^*(x)$, called the *least square approximation*, and the approximation technique that minimizes the worst-case error between $f(x)$ and $p^*(x)$, called the *least maximum approximation* or *minimax approximation*. In [22], several methods are described for approximating a continuous function $f(x)$ with a prespecified precision.

The piecewise polynomial approximation technique has been utilized for generating random variables in channel simulators designed by using the Monte Carlo method, where its implementation in hardware platforms makes it possible to approximate different functions efficiently [23]. The scalability provided by a polynomial approximation architecture allows the efficient use of multiple modules in a channel simulator [23], which represents a good design strategy for the development of real-world channel simulators. In this work, the polynomial coefficients are computed by using the least square approximation as the error metric.

For the evaluation of the sinusoidal functions, the use of a uniform segmentation is feasible. Figure 2(a) shows two approximations of the function $\cos(2\pi x)$, where x is within the range $[0, 1)$. In the first approximation, 16 piecewise polynomials of *degree 1* are considered, whereas the second approximation uses 16 piecewise polynomials of *degree 2*. It can be seen in Figure 2(b) that the approximation using polynomials of *degree 2* results in a much lower absolute error compared with the one using polynomials of *degree 1*. Hence, a sinusoid generator that uses a polynomial approximation of *degree 2* is preferred for the generation of cisoids. It should be noted that for the hardware implementation of a polynomial of degree d , d multipliers and d adders are required if a pipeline structure is applied, otherwise only one multiplier and one adder are required when using an iterative scheme.

3.2. Direct Digital Synthesizer Based on a Piecewise Polynomial Approximation. After analyzing the piecewise polynomial approximation, it is indispensable to visualize this technique for the generation of cisoids with different Doppler

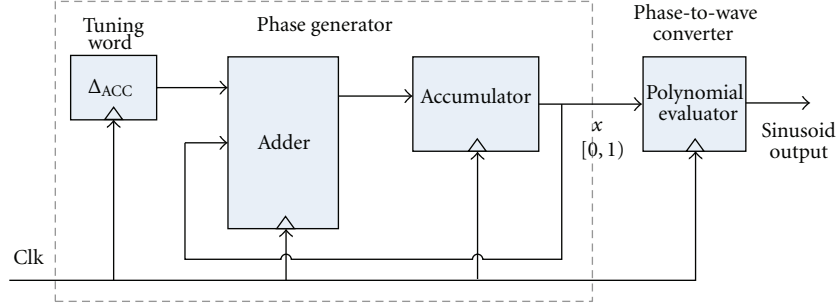


FIGURE 3: Architecture for the complex sinusoid generation module.

frequencies. Therefore, the structure of a *direct digital synthesizer* (DDS) employing the polynomial approximation technique is shown in Figure 3.

Besides the difference in the sinusoid generator concept (sinusoid storing versus sinusoid approximation), there is also a difference between the phase generator of the DDSs. While the phase generator of the LUT-based oscillator directly generates the memory addresses, the phase generator of the polynomial approximation method computes values in the interval $[0, 1)$ for the case of the approximated function $\cos(2\pi x)$. This feature makes it possible to generate sinusoids for a wide range of frequencies. For the application of the SOS method, it is important that a high Doppler frequency resolution can be achieved for lower as well as for higher Doppler frequencies.

The frequency resolution of the DDS based on the polynomial approximation is determined by the sampling frequency F_c and the quantization factor Q_{bits} , which determines the precision of the input x after its quantization with Q_{bits} . The minimum frequency achievable by the DDS as well as the output frequency F_0 are determined by the following expressions:

$$F_{0_{\min}} = \frac{F_c}{2^{Q_{\text{bits}}}}, \quad (21a)$$

$$F_0 = F_0(\Delta_{Q_{\text{bits}}}) = \frac{F_c}{2^{Q_{\text{bits}}}} \Delta_{Q_{\text{bits}}}, \quad (21b)$$

where $\Delta_{Q_{\text{bits}}}$ is the tuning word that specifies the output frequency F_0 . With regard to the configuration of the waveform's phase, the polynomial-based DDS has the same advantages as the LUT-based DDS. However, the phase for the polynomial approximation approach is defined in the interval $[0, 1)$. For the case of a datapath with a bit-width of 32 bits, the parameter Q_{bits} is equal to 31 bits, and the remaining bit is used as a sign bit. Hence, the minimum frequency achievable by the DDS at an output data rate of 1 MSPS is equal to $F_{0_{\min}} = 0.4$ mHz. In the case of an output rate of 4096 samples per second, the frequency resolution will be $F_{0_{\min}} = 1.9$ μ Hz. In comparison with a LUT-based DDS, the same frequency resolutions can be achieved by using a LUT memory of 2^{31} samples if a complete sinusoid is stored, or $2^{31}/4$ samples if a quarter of a sinusoid is stored. It can be inferred from the discussion above that the usage of a LUT-based DDS for achieving a high frequency resolution $F_{0_{\min}}$ of less than 1 Hz is not a practical option.

The SOC method requires the evaluation of both cosine and sine waveforms (see (18)). This results in the use of either one or two polynomial-based DDS modules. Figure 4 illustrates the architecture of the poly-evaluator module, which consists of three blocks: the *address generator unit* (AGU), the *datapath of the evaluation*, which applies Horner's rule, and the *piecewise polynomial coefficients* used for storing the polynomial coefficients. When the value x is generated, this value is passed through the AGU module to compute the address of the corresponding polynomial coefficients. Once the address is obtained, the evaluation is performed while the argument x and the three coefficients are being passed across the datapath, as it can be seen at the bottom of Figure 4. The cisoid evaluation requires two clock cycles when employing a single poly-evaluator module. However, when two modules are used, the cisoid evaluation is achieved within a single clock cycle. In addition to the cisoid evaluation, the poly-evaluator module has been applied for the generation of Gaussian random variables [24], which demonstrates the usefulness of the piecewise polynomial approximation technique.

4. Parameter Computation Methods

In order to demonstrate the performance of the proposed hardware fading channel simulator under different propagation scenarios, two methods were chosen to compute the parameters of the SOC model: the extended method of exact Doppler spread (EMEDS) for the case of isotropic scattering and the modified method of equal areas (MMEA) for non-isotropic scattering.

4.1. The EMEDS. The EMEDS was proposed in [25] as an extension of the method of exact Doppler spread (MEDS) [26]. The MEDS was originally proposed for computing the model parameters of SOS Rayleigh fading channel simulators, while the EMEDS has been developed for the parametrization of SOC Rayleigh fading channel simulators. Currently, the EMEDS is one of the principal methods for computing the model parameters of SOC channel models. This method has been highly recognized in the case of isotropic scattering.

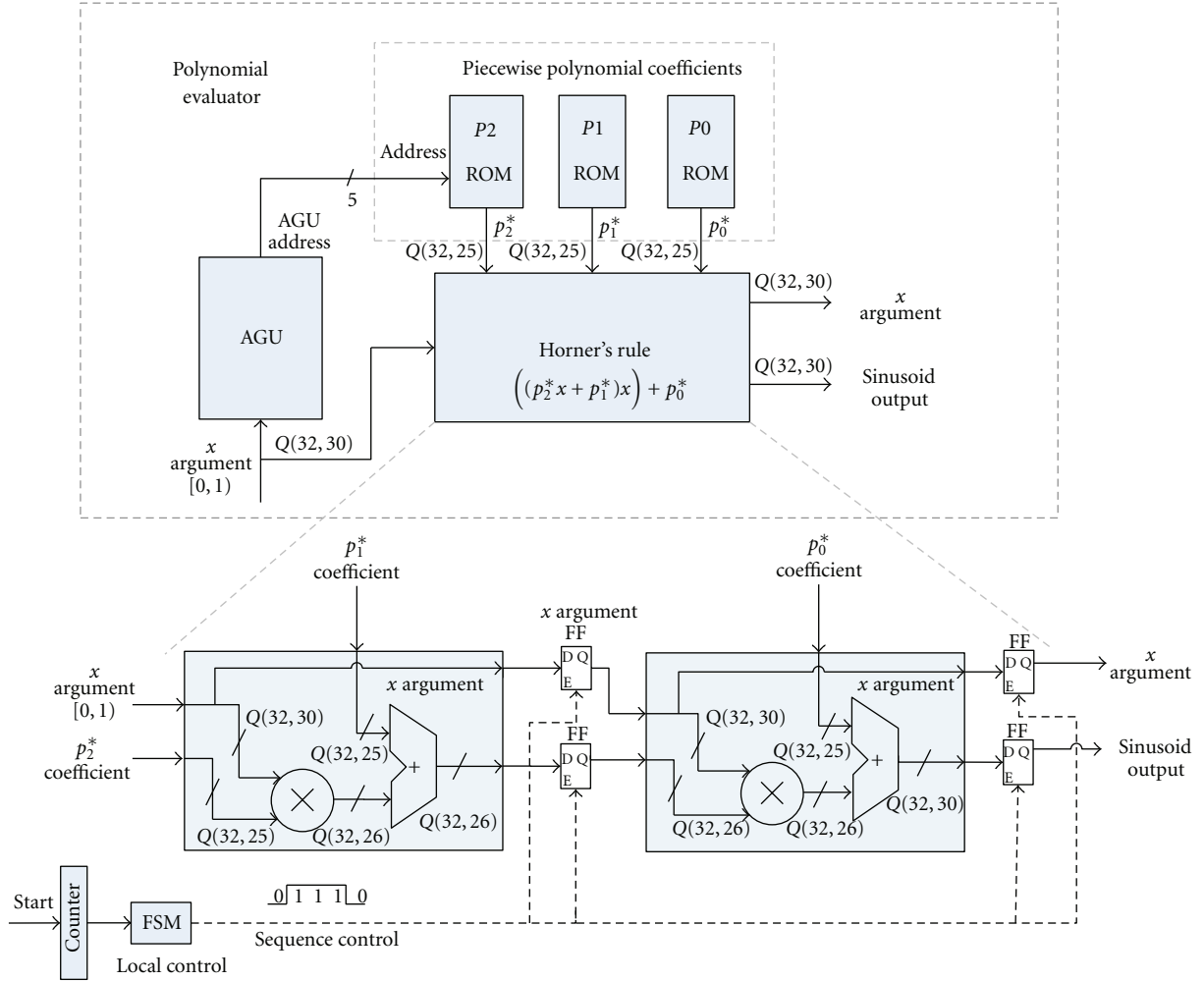


FIGURE 4: Architecture of the poly-evaluator module.

For the Jakes PSD, the EMEDS proposes to compute the path gains c_n and Doppler frequencies f_n as follows [1, 25]:

$$c_n = \sigma_0 \sqrt{\frac{2}{N}}, \quad (22)$$

$$f_n = f_{\max} \cos \left[\frac{2\pi}{N} \left(n - \frac{1}{4} \right) \right] \quad (23)$$

for $n = 1, 2, \dots, N$.

4.2. The MMEA. Currently, there are only some few methods available for computing the model parameters of SOC models under non-isotropic scattering conditions [1]. The MMEA provides a reasonably good solution for this kind of problems. The MMEA [27, 28] is a modification of the method of equal areas (MEA) reported in [29]. The MMEA methodology requires the computation of an inverse function for obtaining a set of Doppler frequencies. When using the MMEA, it is necessary to compute first the cumulative power function (CPF) of a given asymmetrical PSD, and then one has to find the inverse CPF (ICPF). An algorithm was developed using MATLAB in order to obtain the

ICPF function. This algorithm uses a piecewise polynomial approximation technique. It is completely parameterizable, allowing the configuration of the polynomial degree, the number of segments at which the ICPF is approximated, the segmentation technique (uniform or non-uniform segmentation), and the method for obtaining the polynomial coefficients (least square or minimax approximation).

Once the ICPF is obtained, the Doppler frequencies are computed according to the following expression:

$$f_n = F_f^{-1} \left[\frac{\sigma^2}{N} \left(n - \frac{1}{2} \right) \right], \quad (24)$$

where $F_f^{-1}(\cdot)$ represents the ICPF. The path gains c_n are computed by using (22).

5. Test Results

Using the parameter computation methods described in Section 4, the accuracy of the proposed architecture will be evaluated in the present section. For this reason, the hardware

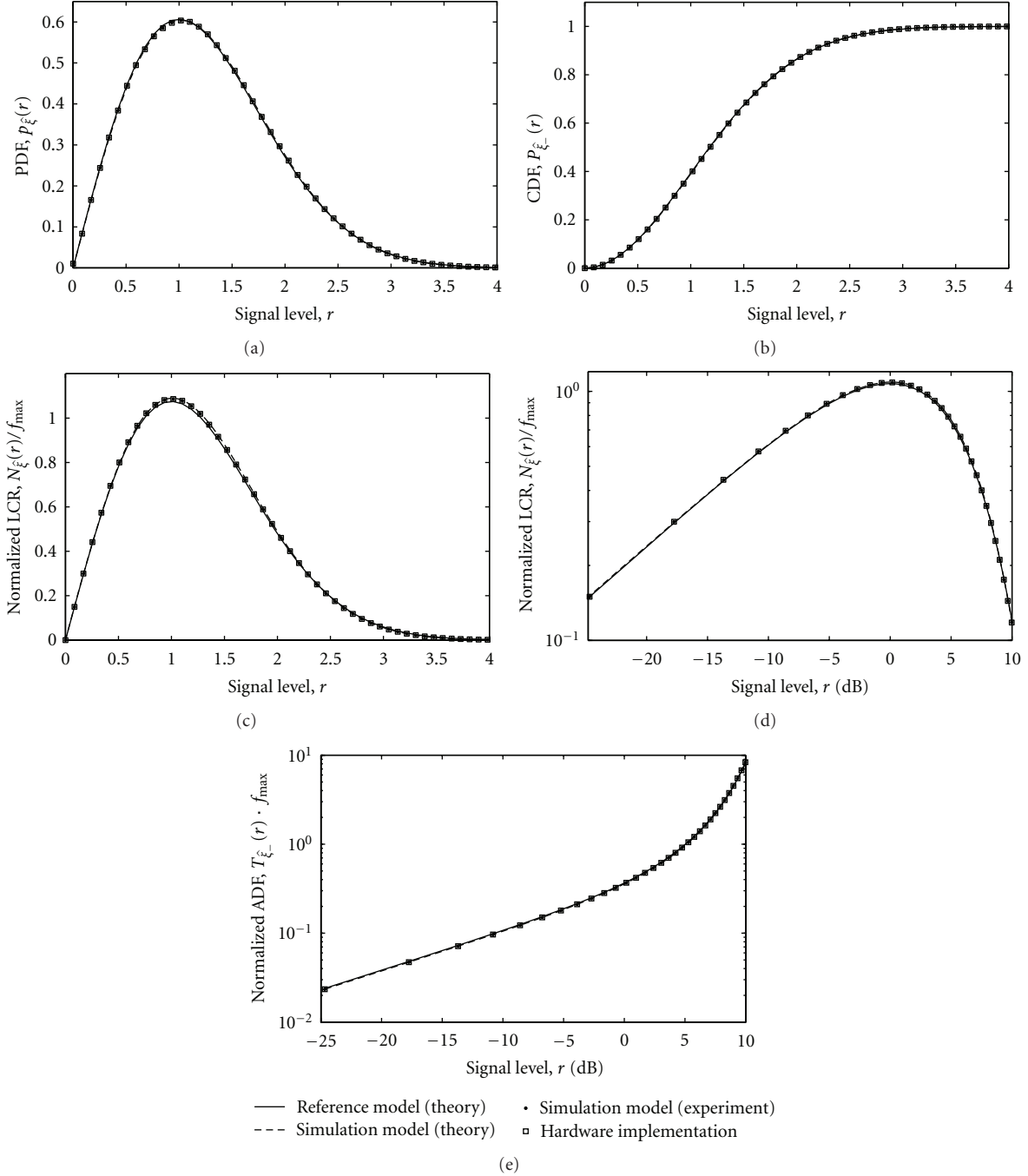


FIGURE 5: PDF, CDF, LCR, and ADF comparison results of the generated envelope process under isotropic scattering (Jakes PSD) using $\sigma_0^2 = 1$, $N = 32$, and $f_{\max} = 91$ Hz.

channel simulator has been configured and tested according to the criteria described in the following subsection.

5.1. Test Configuration. In addition to the path gains c_n and Doppler frequencies f_n , the phases θ_n have been computed using a uniform random number generator, as reported in [30]. For the generation of Rayleigh processes, the LOS component in (2) has been set to zero, that is, $m = 0$. The number of cisoids N was set to 32, the segment number

for the *sine* and *cosine* function generation was 32, and the datapath in the general architecture was equal to $WL = 32$ bits. This configuration has been chosen for comparison purposes with other available architectures (see Section 6). The maximum Doppler frequency f_{\max} was fixed to 91 Hz. The variance σ_0^2 was equal to unity in case of isotropic scattering (Jakes PSD). For non-isotropic scattering (von Mises PSD), the parameter σ_0^2 was set to 0.5. Finally, the statistical properties were obtained by averaging the results over 10 trials, and updating only the phases for each trial.

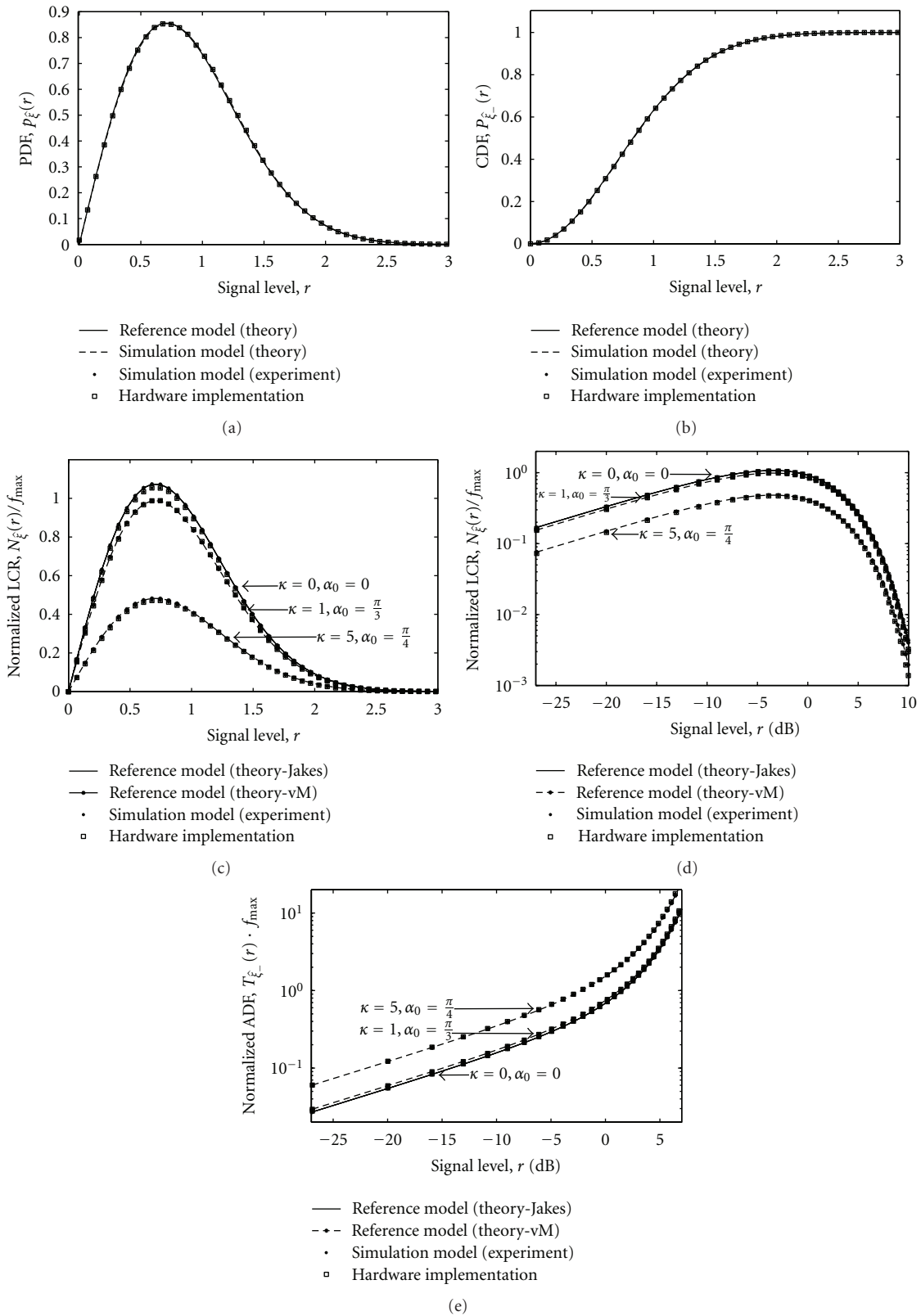


FIGURE 6: PDF, CDF, LCR, and ADF comparison results of the process generated envelope under non-isotropic scattering (von Mises PSD) using $\sigma_0^2 = 0.5$, $N = 32$, $f_{\max} = 91$ Hz, and a parameter configuration pair of $(\kappa = 0, \alpha_0 = 0)$, $(\kappa = 1, \alpha_0 = \pi/3)$, and $(\kappa = 5, \alpha_0 = \pi/4)$.

5.2. *Hardware Test Results.* The comparison results of the proposed hardware fading channel simulator and the reference model for isotropic scattering (Jakes PSD) are presented in Figure 5. The PDF, CDF, and LCR of the reference model are described by (6), (8), and (11), respectively. The results obtained for the reference model are shown in form of continuous lines. The ADF of the reference model has been found by computing the quotient of the expressions in (8) and (11).

Equations (5), (7), (10), and (12) are plotted in Figure 5 as dashed lines, which represent the theoretical results of the simulation model. The experimental results of the implemented SOC simulation model in floating-point representation have been computed using MATLAB. This model has been implemented for reasons of comparison with the hardware implementation. The envelope generated by the SOC model can be identified in the plots by dot markers. Finally, the square markers are used for illustrating the behavior of the proposed hardware fading channel simulator.

Figure 5(a) shows the PDF plots of the generated envelope process for $N = 32$ cisoids. This PDF converges to the Rayleigh density as N increases. However, the resulting PDF obtained with the hardware output samples has a perfect match with the corresponding PDFs of the theoretical and experimental simulation models. The CDF comparison is presented in Figure 5(b). The normalized LCR is plotted in Figure 5(c) and its corresponding plot in decibels (dB) is shown in Figure 5(d). Finally, Figure 5(e) shows the comparison of the ADFs.

Figure 6 illustrates the results when the proposed architecture is configured for producing samples under non-isotropic scattering conditions using the von Mises AOA distribution. The parameters κ and α_0 were set according to the following configurations: ($\kappa = 0, \alpha_0 = 0$), ($\kappa = 1, \alpha_0 = \pi/3$), and ($\kappa = 5, \alpha_0 = \pi/4$). The PDF and CDF plots of the generated envelope process are shown in Figures 6(a) and 6(b), respectively. The resulting LCR for the different configurations of κ and α_0 is presented in Figure 6(c), and its corresponding plot in decibels (dB) is illustrated in Figure 6(d). Figure 6(e) shows the plot corresponding to the ADF. It can be observed that for $\kappa = 0$ and $\alpha_0 = 0$, the graphs of the reference model defined for the cases of isotropic and non-isotropic scattering perfectly overlap with the experimental results.

6. Performance Analysis

The performance of the proposed hardware channel simulator was analyzed using 32, 24, 18, and 16 bits for WL. The implementation was synthesized in a Xilinx Virtex5 FPGA (XC5VLX110T-3FF1136). The used hardware resources of the hardware architecture are summarized in Table 1. The four random-access memories (RAMs) are needed for storing the gains c_n (one RAM block), the Doppler frequencies f_n (one RAM block), and the cosine and sine phases (one RAM block each). It is important to mention that the RAM sizes are parameterizable in accordance to the number of cisoids

TABLE 1: Hardware resource analysis of the SOC fading channel simulator for an implementation in a virtex5 XC5VLX110T-3FF1136 using $N = 32$ cisoids.

Used elements	Datapath bit-width			
	16	18	24	32
Number of slice registers	609	675	873	1086
Number of slice LUT	708	768	975	978
Number of RAMs ($N \times$ WL)	4	4	4	4
Number of ROMs ($32 \times$ WL bits)	3×2	3×2	3×2	3×2
Number of multipliers	6	6	6	6
Number of adders	16	16	16	16

N . On the other hand, the read-only memories (ROMs) allocate the coefficients of the polynomial approximation. In this case, the number of segments has been configured to 32. Consequently, only three ROMs of 32 memory locations (for each quadrature component) are needed for a single poly-evaluator module. Likewise, the multipliers are distributed as follows: two multipliers for each poly-evaluator module and two multipliers for the multiplication between the gain c_n and the cisoid.

Table 2 shows the performance comparison of the proposed architecture with the hardware fading channel simulators. These simulators, which are also using the SOS principle, are the most representative and novel works described in [9, 10]. In [9], a MIMO channel simulator has been implemented using 32 stochastic processes. The inphase and quadrature phases of the channel model are updated for each realization using a random walk process. Moreover, in [10], a triply selective SOS fading channel simulator has been implemented, where the sinusoids are generated in parallel fashion. It should be noted that a detailed comparison of the hardware resources is difficult to achieve. This is due to the differences in hardware implementation, as well as due to the FPGA technologies utilized in the references [9, 10].

In order to ensure a fair comparison, the hardware resources of the fading channel simulators described in [9, 10] have been inferred from the architecture schematics described by the authors. Therefore, Table 2 only considers the hardware resources of a single SOS Rayleigh fading channel simulator module. From Table 2, it can be observed that the principal resource saved by using the proposed architecture lies in the ROMs, which are needed for implementing the sine/cosine functions of the SOS models for all compared methods. This saving is due to the fact that our architecture only stores the polynomial coefficients for the cosine/sine function generation, while the other architectures have to store a rather large number of sinusoid samples. Furthermore, the use of the polynomial approximation technique makes it possible to achieve a high frequency resolution with regard to the sinusoid generation, which greatly improves the statistics of the generated process. In this work, the frequency resolution achieved is $7.63 \mu\text{Hz}$. This value has been computed using (21a), where the fading generation rate is $F_c = 16,384$ samples per second.

TABLE 2: Performance comparison of fading channel simulators (Rayleigh fading).

Used elements	Implementation		
	[9]	[10]	[Proposed]
Number of sinusoids	32	16	32
Clock. freq. (MHz)	224	50	90
Number of multipliers	1	$2 \times 16 + 2$	6
Number of adders	9	$4 \times 16 + 2$	16
Number of RAMs	4 (32×16 bits)	Unknown	4 ($N \times$ WL bits)
Number of ROMs	2 (1024 and 4096×16 bits)	$D \times 2 \times 16 \times 16$ bits ¹	6 ($32 \times$ WL bits)
Frequency resolution	Unknown	Unknown	7.63 μ Hz
SOS-Based	SOS	SOS	SOC
Isotropic scattering	Yes	Yes	Yes
Non-isotropic and asymmetrical scattering	No	No	Yes

Note: The hardware resources have been deduced from [9, 10] by considering a single Rayleigh process.

¹The symbol D is the LUT size, which is not provided in [10].

It should be highlighted that [9] requires only a single multiplier in its architecture. However, this restricts the architecture to SOS models in which all sinusoids have the same amplitude. This is in contrast to the proposed architecture that can be used for any SOS/SOC model, even if the sinusoids do not have the same amplitude. Besides the hardware differences in previous works and the ones proposed here, the most important difference lies in the functionality: only the proposed simulator has the capability of generating waveforms characterized by both symmetrical and asymmetrical PSDs.

7. Conclusions

In this paper, an efficient hardware SOC fading simulator was presented. This flexible and parametric architecture is capable of generating stochastic processes with symmetrical and asymmetrical PSDs. The use of a piecewise polynomial approximation technique allows generating cisoids with a high frequency resolution, which results in highly accurate first- and second-order statistics of the generated envelope processes. This allows the reproduction of realistic channel scenarios, as required in the latest wireless communications standards. In addition, the architecture described in this paper is simple and easy to implement, considering that only small hardware resources are needed in comparison with other hardware SOS simulators. Therefore, the proposed architecture can be considered as a key module for development of more elaborated channel simulators, such as wideband and MIMO channel simulators.

References

- [1] M. Pätzold, *Mobile Radio Channels*, John Wiley & Sons, Chichester, UK, 2nd edition, 2011.
- [2] W. C. Jakes, Ed., *Microwave Mobile Communications*, IEEE Press, Piscataway, NJ, USA, 1994.
- [3] R. H. Clarke, "A statistical theory of mobile-radio reception," *Bell System Technical Journal*, vol. 47, pp. 957–1000, 1968.
- [4] M. Pätzold, Y. Li, and F. Laue, "A study of a land mobile satellite channel model with asymmetrical Doppler power spectrum and lognormally distributed line-of-sight component," *IEEE Transactions on Vehicular Technology*, vol. 47, no. 1, pp. 297–310, 1998.
- [5] W. R. Braun and U. Dersch, "A physical mobile radio channel model," *IEEE Transactions on Vehicular Technology*, vol. 40, no. 2, pp. 472–482, 1991.
- [6] J. P. Rossi, J. P. Barbot, and A. J. Levy, "Theory and measurement of the angle of arrival and time delay of UHF radiowaves using a ring array," *IEEE Transactions on Antennas and Propagation*, vol. 45, no. 5, pp. 876–884, 1997.
- [7] J. G. Wang, A. S. Mohan, and T. A. Aubrey, "Angles-of-arrival of multipath signals in indoor environments," in *Proceedings of the IEEE 46th Vehicular Technology Conference*, pp. 155–159, May 1996.
- [8] W. C. Y. Lee, "Finding the approximate angular probability density function of wave arrival by using a directional antenna," *IEEE Transactions on Antennas and Propagation*, vol. AP-21, no. 3, pp. 328–334, 1973.
- [9] S. F. Fard, A. Alimohammad, and B. F. Cockburn, "An FPGA-based simulator for high path count Rayleigh and Rician fading," *IEEE Transactions on Vehicular Technology*, vol. 59, no. 6, pp. 2725–2734, 2010.
- [10] F. Ren and Y. R. Zheng, "A novel emulator for discrete-time MIMO triply selective fading channels," *IEEE Transactions on Circuits and Systems*, vol. 57, no. 9, pp. 2542–2551, 2010.
- [11] S. F. Fard, A. Alimohammad, B. Cockburn, and C. Schlegel, "A single FPGA filter-based multipath fading emulator," in *Proceedings of the IEEE Global Telecommunications Conference (GLOBECOM '09)*, Honolulu, Hawaii, USA, December 2009.
- [12] R. Parra-Michel, V. Kontorovitch, A. Orozco-Lugo, and M. Lara, "Computational complexity of narrowband and wideband channel simulators," in *Proceedings of the IEEE 58th Vehicular Technology Conference (VTC'03)*, pp. 143–148, Orlando, Fla. USA, 2003.
- [13] M. Pätzold and B. Talha, "On the statistical properties of sum-of-cisoids-based mobile radio channel simulators," in *Proceedings of the 10th International Symposium on Wireless Personal Multimedia Communications (WPMC '07)*, pp. 394–400, Jaipur, India, 2007.
- [14] M. Pätzold and C. A. Gutiérrez, "Level-crossing rate and average duration of fades of the envelope of a sum-of-cisoids," in *Proceedings of the IEEE 67th Vehicular Technology Conference-Spring (VTC '08)*, pp. 488–494, Singapore, May 2008.

- [15] S. O. Rice, "Mathematical analysis of random noise," *Bell System Technical Journal*, vol. 23, pp. 282–332, 1944.
- [16] S. O. Rice, "Mathematical analysis of random noise," *Bell System Technical Journal*, vol. 24, pp. 46–156, 1945.
- [17] M. Pätzold, J. Vázquez, C. Gutiérrez, and R. Parra-Michel, "An exact solution for the level-crossing rate and the average duration of fades of the Envelope of sum-of-cisoids," in *Proceedings of the Conference on Electronics Engineering and Computer Science (CIIIECC '12)*, pp. 30–40, Guadalajara, Mexico, 2012.
- [18] A. Abdi, J. A. Barger, and M. Kaveh, "A parametric model for the distribution of the angle of arrival and the associated correlation function and power spectrum at the mobile station," *IEEE Transactions on Vehicular Technology*, vol. 51, no. 3, pp. 425–434, 2002.
- [19] A. Abdi, K. Wills, H. A. Barger, M. S. Alouini, and M. Kaveh, "Comparison of the level crossing rate and average fade duration of Rayleigh, Rice, and Nakagami fading models with mobile channel data," in *Proceedings of the 52nd Vehicular Technology Conference (VTC '00)*, pp. 1850–1857, September 2000.
- [20] L. Cordesses, "Direct digital synthesis: a tool for periodic wave generation," *IEEE Signal Processing Magazine*, vol. 21, no. 4, pp. 50–54, 2004.
- [21] M. Pätzold and D. Kim, "Test procedures and performance assessment of mobile fading channel simulators," in *Proceedings of the 59th IEEE Semiannual Vehicular Technology Conference (VTC '04)*, pp. 254–260, Milan, Italy, 2004.
- [22] J. M. Muller, *Elementary Functions, Algorithms and Implementation*, Birkhäuser, Boston, Mass, USA, 2th edition, 2002.
- [23] R. Zarate-Martinez, F. Pena-Campos, J. Vázquez Castillo, and R. Parra-Michel, "Arbitrary distribution random variable generator for channel emulators," in *Proceedings of the IEEE International Conference on Reconfigurable Computing and FPGAs (ReConFig '11)*, pp. 339–344, Cancun, Mexico, 2011.
- [24] J. Vázquez Castillo, A. Castillo Atoche, O. Longoria-Gandara, and R. Parra-Michel, "An efficient Gaussian random number architecture for MIMO channel emulators," in *Proceedings of the IEEE Workshop on Signal Processing System (SIPS '11)*, pp. 316–321, Beirut, Lebanon, October 2011.
- [25] B. O. Hogstad, M. Pätzold, N. Youssef, and D. Kim, "A MIMO mobile-to-mobile channel model: part II—the simulation model," in *Proceedings of the 16th International Symposium on Personal, Indoor and Mobile Radio Communications (PIMRC '05)*, pp. 562–567, Berlin, Germany, September 2005.
- [26] M. Pätzold, U. Killat, F. Laue, and Y. Li, "On the statistical properties of deterministic simulation models for mobile fading channels," *IEEE Transactions on Vehicular Technology*, vol. 47, no. 1, pp. 254–269, 1998.
- [27] C. A. Gutiérrez-Díaz-De-Leon and M. Pätzold, "Sum-of-sinusoids-based simulation of flat fading wireless propagation channels under non-isotropic scattering conditions," in *Proceedings of the 50th Annual IEEE Global Telecommunications Conference (GLOBECOM '07)*, pp. 3842–3846, Washington, DC, USA, November 2007.
- [28] C. A. Gutiérrez-Díaz-De-Leon and M. Pätzold, "Efficient sum-of-sinusoids-based simulation of mobile fading channels with asymmetrical Doppler power spectra," in *Proceedings of the 4th IEEE International Symposium on Wireless Communication Systems (ISWCS '07)*, pp. 246–251, Trondheim, Norway, October 2007.
- [29] M. Pätzold, U. Killat, and F. Laue, "A deterministic digital simulation model for suzuki processes with application to a shadowed Rayleigh land mobile radio channel," *IEEE Transactions on Vehicular Technology*, vol. 45, no. 2, pp. 318–331, 1996.
- [30] J. Vázquez Castillo, L. Vela-García, A. Castillo Atoche, J. López Estrada, and R. Parra-Michel, "High-speed low-power parallel random number generator for wireless channel emulators," in *Proceedings of the Symposium on Circuits and Systems (LASCAS '12)*, pp. 1–4, Playa del Carmen, Mexico, 2012.

Research Article

Filter-Based Fading Channel Modeling

Amirhossein Alimohammad,¹ Saeed Fouladi Fard,² and Bruce F. Cockburn³

¹ Department of Electrical and Computer Engineering, San Diego State University, San Diego, CA 92182, USA

² Ukalta Engineering, 4344 Enterprise Square, 10230 Jasper Avenue, Edmonton, AB, Canada T5J 4P6

³ Department of Electrical and Computer Engineering, University of Alberta, Edmonton, AB, Canada T6G 2V4

Correspondence should be addressed to Amirhossein Alimohammad, aalimohammad@mail.sdsu.edu

Received 28 April 2012; Accepted 6 August 2012

Academic Editor: Neji Youssef

Copyright © 2012 Amirhossein Alimohammad et al. This is an open access article distributed under the Creative Commons Attribution License, which permits unrestricted use, distribution, and reproduction in any medium, provided the original work is properly cited.

A channel simulator is an essential component in the development and accurate performance evaluation of wireless systems. A key technique for producing statistically accurate fading variates is to shape the flat spectrum of Gaussian variates using digital filters. This paper addresses various challenges when designing real and complex spectrum shaping filters with quantized coefficients for efficient realization of both isotropic and nonisotropic fading channels. An iterative algorithm for designing stable complex infinite impulse response (IIR) filters with fixed-point coefficients is presented. The performance of the proposed filter design algorithm is verified with 16-bit fixed-point simulations of two example fading filters.

1. Introduction

Wireless communication systems must be designed to operate over radio channels in a wide variety of expected environments. Testing wireless transceivers is challenging due to unrepeatable and uncontrollable channel conditions. The initial performance verification of communication systems at the early stages of the design cycle is performed based on the channel characteristics defined by the underlying wireless communication standard. Therefore, accurate emulation of fading channels is a key step in the design and verification of wireless communication systems.

In the multipath propagation scenario, the received signal contains different faded copies of the transmitted signal. The effect of the multipath fading channel on the baseband signal can be modeled with a time-variant linear system with the following impulse response [1]:

$$\alpha(\tau; t) = \sum_{n=0}^{N_p-1} \mu_n |c_n(t)| e^{j\angle c_n(t)} \delta(\tau - \tau_n(t)), \quad (1)$$

where N_p is the number of independent paths, μ_n is the average attenuation of the n th path, and $c_n(t)$ and $\tau_n(t)$ denote the complex gain and delay of the n th path. Each

path gain $c_n(t)$ is commonly modeled as a complex Gaussian wide-sense stationary (WSS) process [2].

To simulate a fading channel, we need to generate a suitable sequence of complex path gains $\{c_n(t)\}$ and then superimpose delayed replicas of the transmitted samples with the given delays $\{\tau_n(t)\}$ and path attenuations $\{\mu_n\}$. Two major techniques have been widely used for simulating fading channels. In the first approach, the so-called sum-of-sinusoids (SoS) model, the fading process is modeled as the superposition of a sufficiently large number of sinusoidal waves. This approach was originally proposed by Clarke [3] and later simplified by Jakes [4]. Over the past four decades several modified SoS-based models have been proposed (e.g., [5, 6]).

The second approach, which is used in this paper, is called the filter-based scheme. In this approach, to generate the in-phase $c_i(t)$ and quadrature components $c_q(t)$ of complex fading process $c_n(t) = c_{i,n}(t) + jc_{q,n}(t)$ with a particular correlation between variates, a complex zero-mean and unit-variance Gaussian random process $n(t) = n_i(t) + jn_q(t)$ with independent samples is passed through a spectrum shaping filter (SSF) [7] with an appropriate frequency response $H(f)$. A linear filtering operation on the complex Gaussian samples with flat power spectral density

(PSD) yields samples that also have a Gaussian distribution, with spectrum $S_y(f) = S_n(f) |H(f)|^2$, where $S_n(f)$ is the PSD of the input samples and $S_y(f)$ is the PSD of the output samples.

Compared to the SoS-based method, the filter-based fading simulation method is much trickier to design and implement. A filter-based simulator needs to be designed carefully because of possible instability and possible finite word-length effects when implemented with fixed-point arithmetic. On the other hand, filter-based fading simulation has several advantages over the SoS-based method. First, with the filter-based method, it is possible to simulate a wide range of power spectral densities. Second, the filters can be designed to provide a high level of statistical accuracy. Finally, the generated samples have very accurate Gaussian distribution.

In this paper, we present various considerations for designing stable fixed-point spectrum shaping filters for modeling both isotropic and nonisotropic fading channels. We propose an iterative filter design technique. The least-squares cost function is suggested in polar coordinates and augmented with a barrier function that keeps the poles (and potentially also the zeros) within the unit circle to enforce filter stability.

The rest of this paper is organized as follows. Section 2 discusses various considerations when designing isotropic fading channels. Section 3 presents filter design techniques for isotropic fading channels. Section 4 discusses the modeling of nonisotropic fading channels. In Section 5, we present our stable real and complex filter design techniques for stable fixed-point implementations. Finally, Section 6 makes some concluding remarks.

2. Isotropic Fading Channels

Isotropic scattering refers to the case in which the distribution of the incident directions of the received multipath signals, or angle of arrival (AoA), are equally distributed. Assuming an isotropic scattering Rayleigh fading channel with an omnidirectional antenna at the receiver, the path gains are modeled using a unit-variance zero-mean complex Gaussian process $c(t) = c_i(t) + jc_q(t)$ [2]. Both $c_i(t)$ and $c_q(t)$ are Gaussian-distributed independent stochastic processes that have the same autocorrelation function (ACF) $R_{c_i, c_i}(\tau) = R_{c_q, c_q}(\tau) = \mathcal{J}_0(2\pi f_D \tau)/2$, where f_D is the maximum Doppler frequency and $\mathcal{J}_0(\cdot)$ is the zeroth-order Bessel function of the first kind [4]. The PSD associated with either the in-phase or quadrature component of a complex fading signal has the well known Jakes' U-shaped band-limited form with independent in-phase and quadrature samples [8]:

$$S_c(f) = \begin{cases} \frac{1}{\pi\sqrt{f_D^2 - f^2}} & \text{if } |f| < f_D, \\ 0 & \text{otherwise.} \end{cases} \quad (2)$$

Fading samples can be generated by passing a stream of independent Gaussian samples through a SSF with the magnitude response equal to the square root of the magnitude of the PSD of the desired fading process (i.e., $|H(f)| = |S_c(f)|^{1/2}$).

The filtering process can be carried out in the time or frequency domains. In the frequency domain, the Gaussian samples are multiplied by $|S_c(f)|^{1/2}$. Then, an inverse fast Fourier transform (IFFT) can be applied to the resulting discrete spectrum to obtain time series fading samples [9]. The resulting series is still Gaussian by virtue of the linearity of the IFFT, and it has the desired Jakes' spectrum. One major disadvantage of the IFFT method is its block-oriented nature, which requires all fading coefficients to be generated and stored before the data is sent through the channel. This implies significant memory requirements and precludes unbounded continuous transmission, which is usually preferred in long running characterization applications such as hardware fading simulation.

In the time domain, the SSF can be implemented with either finite-impulse response (FIR) filters [10, 11] or infinite impulse response (IIR) filters [12, 13]. When implementing fading channel simulators using FIR and IIR filters, it is important to note that the degree of the FIR filter is related to the time span of the truncated signal held in the filter and inversely proportional to the Doppler frequency. Specifically, implementation of an extremely narrowband digital filter with a sharp cutoff and a very large attenuation in the stop-band requires a high-order FIR filter. Meeting the same specifications with an IIR filter typically requires fewer hardware resources than an FIR filter. In fact, utilizing both feedforward and feedback polynomials in an IIR filter permits steeper frequency roll-offs to be implemented for a given filter order than an FIR filter [14]. However, an FIR filter has no feedback and is thus inherently stable. As the coefficients are quantized in any fixed-point implementation, the resulting numerical error is fed back in the IIR filter, possibly causing instability. Moreover, such effects can cause significant deviations from the expected response. Thus we must ensure that the designed SSF is stable.

The autoregressive (AR) modeling approach has also been proposed for generating fading processes by passing the noise through an all-pole IIR filter [15]. To produce samples with accurate statistics, the AR model needs a large filter order, which greatly increases the number of required multiplications per output sample. Also, implementation of the AR fading simulator demands highly accurate floating-point variables, which makes it unappealing for compact fixed-point implementations.

3. Spectrum Shaping Filter Design for Isotropic Fading Channels

In the design of the SSF, IIR filters are widely preferred to FIR filters due to their reduced computational complexity and their higher stopband attenuation. Moreover, since no constraints are imposed on the phase response, we choose to use IIR filters. We approximate the desired magnitude response of the SSF with an IIR filter of order Γ . The magnitude response of the SSF is expressed as

$$H(e^{j\omega}) = \prod_{q=1}^{\Gamma/2} \left\{ g_q \times \frac{1 + b_{1,q} e^{-j\omega} + b_{2,q} e^{-j2\omega}}{1 + a_{1,q} e^{-j\omega} + a_{2,q} e^{-j2\omega}} \right\}, \quad (3)$$

which is equivalent to the magnitude response of $\Gamma/2$ cascaded canonic second-order sections (SOSs), also known as biquads. In (3), $b_{1,q}$, $b_{2,q}$, $a_{1,q}$, and $a_{2,q}$ denote the coefficients and g_q denotes the real-valued scaling factor of the q th biquad.

For a typical wireless communication scenario, the Doppler frequency f_D is significantly lower than the signal sample rate F_s . Thus, SSF would have an extremely narrow bandwidth and a very sharp cut-off. We can reduce the complexity of SSF by designing it at a much lower sampling frequency, $F_1 \ll F_s$, thereby reducing the required computations and also improving the accuracy of the designed filter. The resulting low-rate signal can then be interpolated to reach the target sampling frequency $F_s = F_1 \times \prod_{j=1}^{T_g} I_j = F_s$, where T_g denotes the number of interpolation stages and I_j is the interpolation factor at the j th interpolation stage. Given the desired frequency response $S_c^{1/2}(f) = (\pi^2(f_D^2 - f^2))^{-1/4}$, $|f| < f_D$, we can find the IIR filter coefficients using the MATLAB function `iir1pnorm`. This function uses double-precision floating-point variables and calculates the optimal values by minimizing the p -norm [16].

Due to the higher hardware cost and complexity of floating-point hardware, fixed-point arithmetic is often preferred in very-large-scale integration (VLSI) and field-programmable gate array (FPGA) implementations. After the initial filter design, the filter coefficients and scaling factors are then quantized for fixed-point implementation. For a compact hardware implementation, variables should be implemented with the minimum possible fixed-point word-length. However, reducing the word-length impacts the response, and potentially the stability, of the designed IIR filter. When the filter coefficients are quantized from floating-point to fixed-point, the poles and zeros of the system function typically shift to new positions in the z -plane. Unfortunately, this step can perturb the implemented frequency response from its intended response. If the designed IIR filter is extremely sensitive to coefficient changes, the filter response might not meet the target specifications or the filter might even become unstable [17]. At this step, the filter has to be tested with fixed-point variables, and scaling factors g_q are determined that sufficiently limit the magnitude of the generated samples to keep them within the representable range. To make sure that the filters are stable under quantization effects, we have designed the filters in fixed-point format using Filter Design Toolbox [18], which offers bit-true implementations of SOSs with section scaling and reordering to obtain maximum accuracy.

An important observation is that if the stopband attenuation of the shaping filter is not sufficiently high, then the out-of-band noise that passes through the filter will degrade the accuracy of the statistics of the generated fading variates. Specifically, since designing a narrowband filter with a sharp cutoff and large attenuation invariably leads to a high-order filter, to obtain the closest approximation to the desired frequency response with a relatively small filter order, we only minimized the approximation error in the passband of the SSF. The low-pass filters utilized downstream in the interpolator stages can then be designed with extra

attenuation over the transition region to ensure a sharp cut-off.

To generate the Rayleigh fading process, independent samples of a zero-mean complex Gaussian process, generated by the Gaussian noise generator (GNG) block in Figure 1, pass through an SSF with a magnitude response equal to the square root of the magnitude of (2). Samples generated by the shaping filter at a low sampling frequency need to be oversampled and passed through lowpass filters in order to obtain the target sample rate F_s . Let P denote the integer upsampling factor. Interpolation of the signal $\{x[n]\}$ is performed by inserting $P - 1$ zeros between each pair of successive samples of $\{x[n]\}$ and then passing the resulting stream through a low-pass filter with cut-off frequency π/P radian/sec. In order to reduce the computational complexity, we perform the interpolation in multiple stages. Since only the amplitude response affects the correlation properties and no restrictions are imposed on the phase response, we use an elliptic IIR low-pass filter (EILPF) in the first stage. The lowpass filter has a symmetric frequency response and hence its poles and zeros appear in complex conjugate pairs, therefore, this filter can be realized using cascaded biquads. The SSF output is upsampled I_1 times and passed to the EILPF generating $F_2 = I_1 \times F_1$ samples per second. The samples are further upsampled and interpolated using fading-specific interpolation low-pass filters (SILPFs) to obtain the desired output sample rate F_s . Since the maximum Doppler frequency is typically much smaller than the sampling frequency, we use a multiplication-free SILPF with frequency response:

$$D_P^{l_z}(e^{j\omega}) = \left(\frac{1 - e^{-j\omega P}}{P - P e^{-j\omega}} \right)^{l_z}, \quad l_z \geq 1, \quad (4)$$

where l_z is the number of cascaded stages.

We propose to design the SSF at a sampling frequency F_1 , where $4f_D < F_1 \leq 8f_D$. Choosing F_1 in this range satisfies the minimum Nyquist rate while keeping the computational complexity low. In addition, we have the opportunity to exploit power-of-2 interpolation factors to further reduce the hardware complexity and simplify the filter design. The generated samples from the SSF are upsampled $I_1 = 16$ times and passed through the EILPF. Note that since the SILPF stages are designed to operate on narrowband signals, the first interpolation stage is positioned prior to the SILPF stages. Then, the samples are passed through successive SILPFs. The i th SILPF interpolates the signal 2^{k_i} times. Based on the processing architecture, the relation between F_1 and the target output sampling rate is $F_s = 16 \times F_1 \times \prod_{i=1}^{T_g} 2^{k_i}$. From here we have $F_1 = 2^{-(4+S_g)} F_s$, where $S_g = \sum_{i=1}^{T_g} k_i$ is an integer value in the range $\log_2(F_s/f_D) - 7 \leq S_g < \log_2(F_s/f_D) - 6$. Based on the maximum interpolation factor $2^{K_{\max}}$, where $K_{\max} = 4 + \max\{S_g\}$, each SILPF is assigned a specific interpolation factor. The minimum Doppler frequency that can be simulated by this system is

$$f_D^{\min} = 2^{-(K_{\max}+3)} F_s. \quad (5)$$

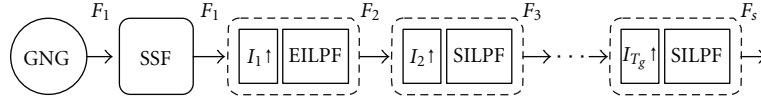
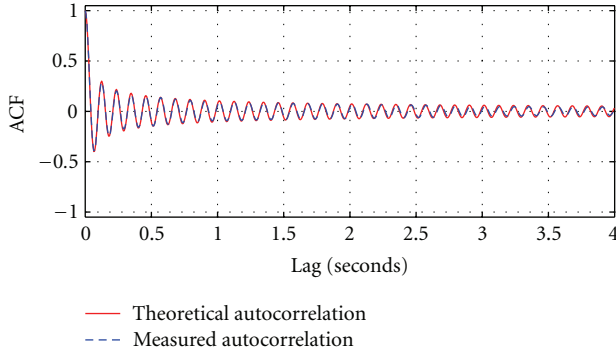
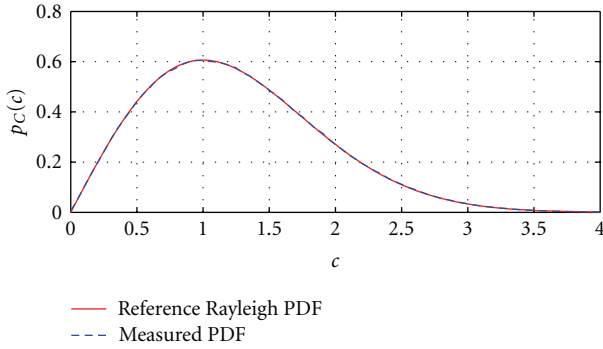


FIGURE 1: Block diagram of the fading simulator.

FIGURE 2: ACF of the generated fading samples with $f_D = 0.6$ Hz, $F_s = 2.5$ MHz over 60 seconds.FIGURE 3: PDF of the generated fading samples with $f_D = 200$ Hz, $F_s = 10$ MHz.

To ensure accuracy, we measured the ACF and the probability density function (PDF) of the generated fixed-point fading samples against the ideal functions. Figure 2 shows the autocorrelation of the real part of the generated fading process. The Doppler frequency is set to $f_D = 0.6$ Hz and the sample rate is $F_s = 2.5$ million samples per second. This figure confirms a close match between the desired response and the generated results over up to 60 seconds. In another example, we measured the PDF for the amplitude of the generated samples with $f_D = 200$ Hz and $F_s = 10$ MHz. The plots in Figure 3 show that the measured PDF accurately matches the ideal Rayleigh PDF.

4. Modeling Nonisotropic Fading Channels

Isotropic scattering assumption has been challenged [19] due to the blockage of some propagation directions and antenna directivity, resulting in a nonuniform PDF for AoA at the receiver. Several nonuniform PDFs have been proposed in the literature to represent the AoA including

the geometrically based PDFs [20], Gaussian PDF [21], quadratic PDF [22], Laplace PDF [23], cosine PDF [24], and von Mises PDF [25]. The von Mises PDF, which includes the uniform AoA distribution as a special case, is supported with empirical measurements of narrowband fading channels in [25]. Also it is argued that the von Mises PDF is attractive because it can approximate other nonuniform PDFs and can provide mathematical convenience for analysis [25].

When the scattering encountered in the propagation environment is nonisotropic [26, 27], the complex envelope of the fading process is

$$\begin{aligned} c(t) &= c_i(t) + jc_q(t) \\ &= \lim_{N \rightarrow \infty} \frac{1}{\sqrt{N}} \sum_{n=1}^N \alpha_n e^{j(2\pi f_D \cos(\Psi_n) + \varphi_n)}, \end{aligned} \quad (6)$$

where ψ_n , $n = 1, \dots, N$ are independent and identically distributed (i.i.d.) angles of arrival of the incoming wave at the receiver antenna with distribution $p_\Psi(\psi)$, φ_n , $n = 1, \dots, N$ are i.i.d. phases with uniform distribution over $[-\pi, \pi)$, and α_n , $n = 1, \dots, N$ are deterministic normalized complex constants that satisfy $\sum_{n=1}^N |\alpha_n|^2 = N$. The PSD function associated with $c(t)$ is given by [25]

$$S_c(f) = \frac{e^{\kappa \cos(\tilde{\psi})(f/f_D)} \cosh\left(\kappa \sin(\tilde{\psi}) \sqrt{1 - (f/f_D)^2}\right)}{\pi I_0(\kappa) \sqrt{1 - (f/f_D)^2}}, \quad (7)$$

where κ controls the beam width, $\tilde{\psi}$ denotes the average AoA of the scattered component, and $I_m(\cdot)$ is the m th order modified Bessel function of the first kind. To obtain (7), it is assumed that the AoA of the scattered component is distributed with the von Mises/Tikhonov distribution [28] as follows:

$$p_\Psi(\psi) = \frac{\exp[\kappa \cos(\psi - \tilde{\psi})]}{2\pi I_0(\kappa)}, \quad \psi \in [-\pi, \pi). \quad (8)$$

Note that when the beam-width parameter κ is zero, the AoA has a uniform distribution over $[-\pi, \pi)$, and (7) reduces to Jakes' "U-shaped" spectrum $S_c(f) = (\pi \sqrt{1 - (f/f_D)^2})^{-1}$.

One of the important steps for generating the fading samples is designing the SSF. While most of the previously proposed filter design techniques might be appropriate for simulations of isotropic fading, they are not the best candidates for nonisotropic scattering scenarios, where AoA is not uniformly distributed or when the antennas are not omnidirectional. In contrast to isotropic fading, the PSD of fading samples in nonisotropic scattering (7) is not symmetric in general, and hence the filter coefficients are potentially complex [29] (e.g., the TGn fading channel

models for simulating IEEE 802.11 radio propagation [30]). We will refer to filters with real coefficients as “real filters” and filters with complex coefficients “complex filters.”

Various methods such as nonlinear optimization [31], linear programming [32], and semidefinite programming [33] have been suggested for designing IIR digital filters in the complex Chebyshev sense. Least-squares methods have also been applied extensively to design IIR filters [34]. For filter stabilization, several approaches have also been proposed. One method, proposed in [35], is to start the optimization from a stable point and then control the step size so that the solution never leaves the stable region. However, this method is computationally expensive and not easy to implement with traditional optimization procedures. In a second method, explicit constraints are imposed on the coefficients of the denominator of the transfer function [36]. This technique, however, has some limitations that affect the filter quality [37]. Finally, in a third method, the least squares cost function is modified so that the minimum always falls in the stable region [37]. This is ensured by adding a barrier function to the original cost function to avoid filter instability. To design the barrier function, an all-pole proxy transfer function is formed consisting of all of the filter poles. The barrier function is basically the sum of the squared amplitude of a section of the impulse response of the proxy transfer function. If the filter is unstable, the trailing tail of the response will have (large) nonzero values.

For efficient filter implementation, the filter design method needs to produce filters that can be implemented with the minimum word-length while providing the required accuracy. The bit-precision selected for implementing the SSF plays an important role in the accuracy, stability, and efficiency of the filter implementation. Various methods have been proposed for designing IIR filters with fixed-point coefficients [38–41]. In [38], the optimal fixed-point real-valued filter is found by reformulating a cost function to include the hardware complexity. The cost function is then minimized using the simulated annealing method [42]. In this approach, no constraints are imposed on the precision of the intermediate signals, which can result in inefficient implementations. The filter design method proposed in [39] is based on FIR-to-IIR filter conversion. However, the resulting IIR filter has significantly higher complexity than its FIR prototype. In [40], IIR filter design is framed as a combinatorial optimization problem that is solved using a genetic algorithm. The design approach in [41] proposes bit-flipping and the downhill-simplex method for fixed-point IIR filter design.

5. Spectrum Shaping Filter Design for Nonisotropic Fading Channels

We represent the IIR filter as a product of first-order sections (FOSs) [43]:

$$H(e^{j\omega}) = A \prod_{k=1}^{\Gamma} \frac{1 - r_k e^{j(\theta_k - \omega)}}{1 - s_k e^{j(\phi_k - \omega)}}, \quad (9)$$

where A is a positive scaling factor, $r_k e^{j\theta_k}$ and $s_k e^{j\phi_k}$ are the k th complex zero and pole, respectively, and Γ is the number of FOSs, that is, the filter order. Here, we focus on designing IIR filters with a prescribed amplitude response. When the amplitude of the frequency response is symmetric, the poles and zeros of (9) appear as complex conjugate pairs and the IIR filter can be implemented using $\Gamma/2$ biquads.

We assume that the desired amplitude response is represented with $2 \times M$ samples y_i^d , where

$$y_i^d = \begin{cases} |G(e^{j2\pi u_i})| & \text{if } 2\pi u_i \text{ is in the passband} \\ \varepsilon, & \text{otherwise,} \end{cases} \quad (10)$$

and where $G(e^{j2\pi u_i})$ is the desired response, $u_i \in [-0.5, 0.5]$ is the normalized sampling frequency, and $\varepsilon > 0$ is the attenuation in the stopband. Similar to the work in [44], we express $H(e^{j\omega}) = AF(\mathbf{x}; e^{j\omega})$, where $F(\mathbf{x}; e^{j\omega})$ represents the product of FOSs in (9) and the column vector \mathbf{x} of length 4Γ contains r_k , s_k , θ_k , and ϕ_k for $k = 1, \dots, \Gamma$. Next, to find the filter parameters we define the cost function as follows:

$$q(A, \mathbf{x}) = \sum_{i=0}^{2M-1} v_i \left(\log \left(A |F(\mathbf{x}; e^{j\omega})| \right) - \log(y_i^d) \right)^2 + B(\vartheta; \varrho; \mathbf{x}), \quad (11)$$

where the weight vector $\mathbf{v} = [v_1, v_2, \dots, v_{2M}]^T$ allows us to emphasize the error minimization for certain frequency bands. Note that the sum of squared errors on a logarithmic scale is augmented by a parametric barrier function $B(\vartheta; \varrho; \mathbf{x})$. Function $B(\vartheta; \varrho; \mathbf{x})$ is included to keep the poles (and zeros, if necessary) within the unit circle to enforce filter stability and is defined as

$$B(\vartheta; \varrho; \mathbf{x}) = \sum_{k=k_0}^{2\Gamma} b(\vartheta; \varrho; x_k), \quad (12)$$

where

$$b(\vartheta; \varrho; \tau) = \begin{cases} 0 & \text{if } |\tau| \leq \varrho, \\ \vartheta \left(\frac{|\tau| - \varrho}{1 - \varrho} \right)^2 & \text{if } \varrho < |\tau| \leq 1, \\ \frac{2\vartheta}{1 - \varrho} |\tau| - \vartheta \left(\frac{1 + \varrho}{1 - \varrho} \right) & \text{if } |\tau| > 1. \end{cases} \quad (13)$$

In (12), ϑ determines how fast the barrier function grows outside of the unit circle and the parameter $\varrho \leq 1$ determines an outer boundary for the poles and zeros. When $k_0 = \Gamma + 1$, the barrier function tries to keep the poles within a circle of radius ϱ . Setting $k_0 = 1$, on the other hand, forces both the poles and zeros into the same boundary. The barrier function (12) is especially useful when designing filters for fixed-point implementation since it can be parameterized to keep the poles and zeros at any desired safe distance from the unit circle. Moreover, using this technique, the quantization noise can be reduced to acceptable levels. It can be shown that the

variance of the quantization noise that originates in the k th FOS when implemented in direct-form-I (DF-I) is

$$\sigma_f^2(k) = \frac{7 \times 2^{-2(\Omega_k-1)}}{6 \times (1 - s_k^2)}, \quad (14)$$

where Ω_k is the number of bits used to quantize the coefficients (and the intermediate variables) at the k th stage. To derive (14), it is assumed that the quantization noise after each multiplier is uniformly distributed, wide-sense stationary white noise that is uncorrelated with both the input signal and the quantization noise in other stages. We also assume that the samples are truncated and represented in 2's-complement. Controlling the maximum absolute value of the filter poles limits the quantization effects to an acceptable level.

The coefficients of the IIR filter are calculated using an iterative optimization algorithm. At each iteration, the optimum scaling factor A^o is calculated as

$$A^o = \prod_{i=0}^{2M-1} \left(\frac{\gamma_i^d}{|F(\mathbf{x}; e^{j2\pi u_i})|} \right)^{(v_i / \sum_{i=0}^{2M-1} v_i)}. \quad (15)$$

This expression for A^o is found by differentiating (11) with respect to A and setting the resulting expression to zero. To calculate the gradient vector

$$\mathbf{g}(A^o, \mathbf{x}) = \left[\frac{\partial q(A^o, \mathbf{x})}{\partial x_1}, \dots, \frac{\partial q(A^o, \mathbf{x})}{\partial x_{4\Gamma}} \right]^T, \quad (16)$$

the partial derivative of $q(A^o, \mathbf{x})$ with respect to the k th component x_k of \mathbf{x} can be calculated as

$$\begin{aligned} \frac{\partial q(A^o, \mathbf{x})}{\partial x_k} &= 2 \sum_{i=0}^{2M-1} \left[\frac{v_i \log(A^o |F(\mathbf{x}; e^{j\omega_i})| / \gamma_i^d)}{|F(\mathbf{x}; e^{j\omega_i})|} \right. \\ &\quad \left. \times \frac{\partial |F(\mathbf{x}; e^{j\omega_i})|}{\partial x_k} \right] + \frac{\partial B(\vartheta; \varrho; \mathbf{x})}{\partial x_k}, \end{aligned} \quad (17)$$

where $\omega_i = 2\pi u_i$,

$$\begin{aligned} \frac{\partial |F(\mathbf{x}; e^{j\omega})|}{\partial r_k} &= |F(\mathbf{x}; e^{j\omega})| \frac{r_k - \cos(\theta_k - \omega)}{|1 - r_k e^{j(\theta_k - \omega)}|^2}, \\ \frac{\partial |F(\mathbf{x}; e^{j\omega})|}{\partial \theta_k} &= |F(\mathbf{x}; e^{j\omega})| \frac{r_k \sin(\theta_k - \omega)}{|1 - r_k e^{j(\theta_k - \omega)}|^2}, \\ \frac{\partial |F(\mathbf{x}; e^{j\omega})|}{\partial s_k} &= |F(\mathbf{x}; e^{j\omega})| \frac{\cos(\phi_k - \omega) - s_k}{|1 - s_k e^{j(\phi_k - \omega)}|^2}, \\ \frac{\partial |F(\mathbf{x}; e^{j\omega})|}{\partial \phi_k} &= |F(\mathbf{x}; e^{j\omega})| \frac{-s_k \sin(\phi_k - \omega)}{|1 - s_k e^{j(\phi_k - \omega)}|^2}, \end{aligned} \quad (18)$$

```

Require:  $\varrho; \vartheta; \mathbf{\Omega}; \mathbf{v} = [v_i]$ , and  $\mathbf{y}^d = [y_i^d]$ 
for  $i = 0, \dots, 2M - 1$ 
  Initialize  $k = 0, \mathbf{x}_0, \mathbf{E}_0 = 20 \mathbf{I}_{4\Gamma \times 4\Gamma}$ 
  while  $|\mathbf{x}_{k+1} - \mathbf{x}_k| \geq \epsilon$  do
    find  $A_k^o$  from (15)
    find  $\mathbf{g}_k = \mathbf{g}(A_k^o; \mathbf{x}_k)$ 
     $\chi_k = \sqrt{\mathbf{g}_k^T \mathbf{E}_k \mathbf{g}_k}$ 
     $\tilde{\mathbf{g}}_k = \mathbf{g}_k / \chi_k$ 
     $\mathbf{x}_{k+1} = \mathcal{Q}[\mathbf{\Omega}, \mathbf{x}_k - (1/(4\Gamma + 1))\mathbf{E}_k \tilde{\mathbf{g}}_k]$ 
     $\mathbf{E}_{k+1} = ((4\Gamma)^2 / ((4\Gamma)^2 - 1))(\mathbf{E}_k - (2/(4\Gamma + 1))\mathbf{E}_k \tilde{\mathbf{g}}_k \tilde{\mathbf{g}}_k^T \mathbf{E}_k)$ 
     $k = k + 1$ 
  end while

```

ALGORITHM 1: Iterative calculation of the filter coefficients [43].

and each partial derivative of the barrier function is given by

$$\begin{aligned} &\frac{\partial B(\vartheta; \varrho; \mathbf{x})}{\partial x_k} \\ &= \begin{cases} 0 & \text{if } |x_k| \leq \varrho \text{ or } k < k_0 \text{ or } k > 2\Gamma, \\ \frac{2\vartheta(|x_k| - \varrho)}{(1 - \varrho)^2} \text{sign}(x_k) & \text{if } \varrho < |x_k| \leq 1, \\ \frac{2\vartheta}{1 - \varrho} \text{sign}(x_k) & \text{if } |x_k| \geq 1. \end{cases} \end{aligned} \quad (19)$$

Algorithm 1 summarizes the steps for our proposed iterative filter design. We utilized the ellipsoid algorithm [45] here for its simplicity; however, other optimization techniques could be used. This filter design algorithm can be parameterized to provide a close approximation of the desired response. The desired response $\mathbf{y}^d = [y_i^d]$, the fixed-point format $\mathbf{\Omega}$ used for the filter coefficients, a weight vector \mathbf{v} , and the outer boundary ϱ for zeros and poles are passed to Algorithm 1. The filter design procedure can start with a reasonable order Γ for the initial approximation. The filter order can be increased gradually if the desired filter characteristics are not met. The algorithm starts from an arbitrary point \mathbf{x}_0 contained within the unit sphere and a relatively large (20 times in this algorithm) initial ellipsoid matrix $\mathbf{E}_0 = 20 \mathbf{I}_{4\Gamma \times 4\Gamma}$, where \mathbf{I} denotes the identity matrix. The algorithm then searches for the optimal solution within the present ellipsoid of feasible points. This algorithm then converges on the optimal solution by successively reducing the size of the ellipsoid by χ_k until it is small enough (i.e., the algorithm has converged) or when $|\mathbf{x}_{k+1} - \mathbf{x}_k|$ is within a chosen accuracy ϵ . The function $\mathcal{Q}[\mathbf{\Omega}, \mathbf{x}]$ represents the quantization effects that affect each element of \mathbf{x} in the Cartesian coordinate system (coefficients are transferred to Cartesian coordinates, quantized, and then transferred back to the polar coordinates). Note that stable real IIR filters can be designed with the above algorithm as well. To design such filters, the sample update is only performed for half of

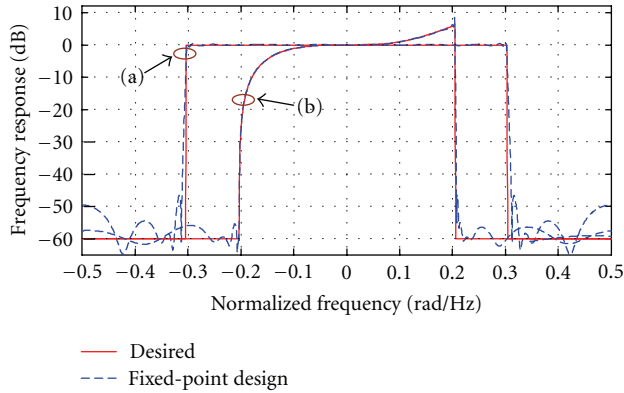


FIGURE 4: Frequency response of the designed fixed-point filters and the desired responses.

the poles and zeros, and the others are simply the complex conjugates of the updated samples.

An important point to note is that IIR filters are naturally susceptible to arithmetic overflow and instability due to the inherent feedback. Both the design and implementation of digital IIR filters must be carried out carefully to avoid such pitfalls. While scaling techniques are commonly used to keep the filter variables in range [46], a poor choice of scaling factor can result in a loss of signal precision and an increase in quantization noise. Another technique is to use more bits to represent intermediate signals. This method, however, is inefficient on DSPs with a fixed word-length. Moreover, simply adding extra bits increases resource utilization in FPGA and ASIC implementations. We suggest to use (i) pole-zero ordering and/or (ii) augmenting auxiliary poles and zeros techniques for minimizing the range of intermediate signals that can be effectively used for reducing the signal range, overflow probability, and resource utilization in hardware implementations [47].

Considering a small section of an IIR filter, overflows are mainly caused by oscillations around resonant frequencies. Assuming a limited input signal range, we can reduce the signal range by reducing the maximum oscillation magnitude. The oscillation frequency is mainly determined by filter poles. Consider a single FOS of an IIR filter with only one pole at frequency $e^{j2\pi f_{\text{pole}}}$. The output range of this section can be reduced significantly if the input signal to this section is attenuated around frequency $e^{j2\pi f_{\text{pole}}}$. In pole-zero ordering technique, we need to implement the IIR filter with the DF-I structure so that the input signal experiences a zero before it is affected by the pole. We thus sort the filter sections according to their pole magnitude in an ascending order and match the filter poles with the closest zeros. Further, signals are scaled in the different stages to assure filter stability.

The second method for reducing the signal range is to attenuate the input signal around the resonant frequencies of an IIR filter $e^{j2\pi f_{\text{Nat}}}$, that could potentially result in oscillation or overflow. This imposed distortion can be later compensated for with additional poles and/or zeros. This technique is applicable only if the input signal does not have a major frequency component around $e^{j2\pi f_{\text{Nat}}}$. One example is

the implementation of narrowband low-pass filters with an approximate resonance frequency around DC. If the input signal does not have a DC component, it can be first passed through a high-pass filter $D(e^{j\omega}) = 1 - e^{-j\omega}$ (difference) prior to being passed through the filter. The filter output can then be later compensated by passing the output signal through the integrator $I(e^{j\omega}) = (1 - \rho e^{-j\omega})^{-1}$. The coefficient $\rho \in [1 - \epsilon, 1)$ is intentionally added here since quantization noise and computational errors can render a perfect integrator (i.e., $\rho = 1$) unstable.

When employed along with pole-zero ordering, the augmented poles and zeros are not included in the ordering process, and instead they keep their position in the DF-I structure, that is, the augmented zero appears first and the pole appears last. This technique, when used in conjunction with pole-zero ordering and scaling, can provide efficient, accurate, and compact implementation of real and complex IIR filters.

To demonstrate the performance of our filter design procedure, we design two IIR filters with $\Gamma = 12$ FOSs. Here, the SSF is approximated with

$$H(e^{j\omega}) = \prod_{k=1}^{\Gamma} g_k \times \frac{1 - b_{1,k} e^{-j\omega}}{1 - a_{1,k} e^{-j\omega}}, \quad (20)$$

where g_k is the positive scaling factor, $b_{1,k}$ and $a_{1,k}$ are the k th complex zero and pole, respectively, and Γ is the filter order. This filter can be realized as a cascade of Γ FOSs. For isotropic scattering, however, poles and zeros of (20) appear in complex conjugate pairs and the shaping filter can be implemented using $\Gamma/2$ canonic second-order sections. We set the parameters $\vartheta = 5$ and $\varrho = 0.99$, that is, the poles and zeros are bounded within a circle of radius 0.99. For all of the FOSs, the number of bits for representing each coefficient is set to $\Omega = 12$. Figure 4 shows the frequency responses of the designed filters (with out-of-band attenuation $\epsilon = 0.001$) as well as the desired responses. In this figure, filter (a) is a lowpass filter with normalized pass frequency $f_p = 0.3$, and filter (b) is a complex filter with frequency response $H(f) = \alpha + \beta f^3$ for $|f| \leq 0.2$ and $H(f) = \epsilon$ for $|f| > 0.2$. As Figure 4 shows, the frequency responses of the designed fixed-point filters closely match the desired responses. Figure 5 shows the position of the poles and zeros for the designed filters. Note that all of the poles and zeros lie within a circle of radius $\varrho = 0.99$.

To illustrate the effectiveness of these range reduction techniques, we simulated an order $\Gamma = 6$ Elliptic low-pass filter with sample rate $F_s = 4800$ Hz, pass frequency $F_{\text{pass}} = 1200$ Hz, stop frequency $F_{\text{stop}} = 1500$ Hz, passband ripple $A_{\text{pass}} = 1$ dB, and stopband attenuation $A_{\text{stop}} = 50$ dB. We measured the maximum absolute range of variables by passing 10^8 uncorrelated zero-mean Gaussian samples through the designed filter. It is assumed that the input signal (white Gaussian noise) does not have a DC component. Table 1 shows the maximum absolute signal ranges for different filter implementations. The output of each FOS or SOS is scaled to lie within $[-1, +1]$. As this table shows, the direct-form-II (DF-II) implementation requires the most number of bits (at least nine bits for the integer part).

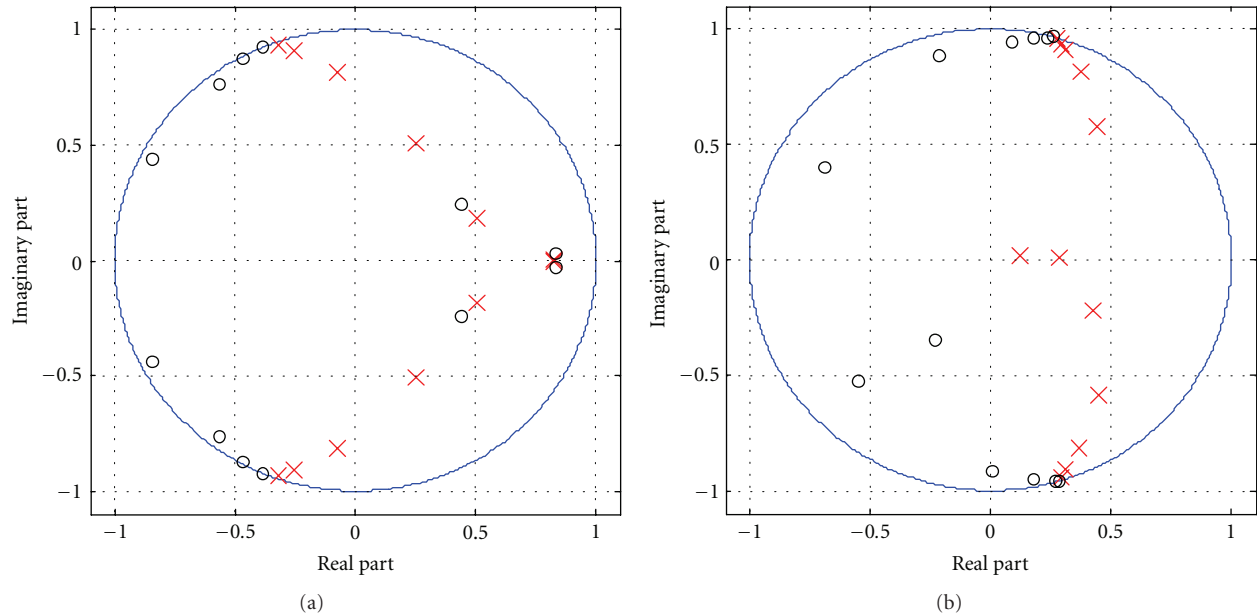


FIGURE 5: Positions of the poles and zeros in the unit circle for the designed filters.

TABLE 1: Maximum absolute signal range in different sections of a low-pass filter implemented with different techniques.

	1st section	2nd section	3rd section
DF-II	182.22	422.82	421.44
DF-I + ord.	35.43	20.93	9.79
DF-I + ord. + aug.	20.87	14.81	11.04

The DF-I implementation of this filter with the pole-zero ordering (DF-I + ord.) reduces the signal range significantly. Moreover, augmenting a zero at DC (DF-I + ord. + aug.) can further reduce the signal range such that the minimum number of integer bits is reduced to five. In this example, the range reduction technique saves four bits in word-length, which can significantly reduce the hardware complexity.

6. Conclusions

In this paper we discussed various considerations when designing accurate isotropic and nonisotropic fading channels. We investigated the filter-based approach, which can be customized to accurately provide the statistical properties required for simulating different fading scenarios. We proposed an iterative technique that can be used to design both complex and real IIR filters with fixed-point coefficients. We augmented the least-squares cost function with a specific barrier function to control the location of the poles (and potentially also the zeros) within the unit circle to ensure numerical stability. We also suggested two techniques for reducing the signal range. Signal range reduction is particularly important in hardware implementation since it can directly reduce hardware complexity. Simulation

results showed that the proposed filter design technique can significantly reduce the required word-length for fixed-point IIR filter implementations.

References

- [1] G. L. Stuber, *Principles of Mobile Communication*, Kluwer Academic Publishers, New York, NY, USA, 2001.
- [2] P. Bello, "Characterization of randomly time-variant linear channels," *IEEE Transactions on Communications*, vol. 11, no. 4, pp. 360–393, 1963.
- [3] R. H. Clarke, "A statistical theory of mobile-radio reception," *Bell System Technical Journal*, vol. 47, pp. 957–1000, 1968.
- [4] W. C. Jakes, *Microwave Mobile Communications*, Wiley-IEEE Press, Piscataway, NJ, USA, 1994.
- [5] Y. R. Zheng and C. Xiao, "Simulation models with correct statistical properties for Rayleigh fading channels," *IEEE Transactions on Communications*, vol. 51, no. 6, pp. 920–928, 2003.
- [6] A. Alimohammad, S. Fouladi Fard, B. F. Cockburn, and C. Schlegel, "An improved SOS-based fading channel emulator," in *Proceedings of the IEEE 66th Vehicular Technology Conference (VTC'07)*, pp. 931–935, Baltimore, Md, USA, October 2007.
- [7] J. I. Smith, "Computer generated multipath fading simulation for mobile radio," *IEEE Transactions on Vehicular Technology*, vol. 24, no. 3, pp. 39–40, 1975.
- [8] R. H. Clarke and W. L. Khoo, "3-D mobile radio channel statistics," *IEEE Transactions on Vehicular Technology*, vol. 46, no. 3, pp. 798–799, 1997.
- [9] D. J. Young and N. C. Beaulieu, "The generation of correlated Rayleigh random variates by inverse discrete fourier transform," *IEEE Transactions on Communications*, vol. 48, no. 7, pp. 1114–1127, 2000.
- [10] K. W. Yip and T. S. Ng, "Efficient simulation of digital transmission over WSSUS channels," *IEEE Transactions on Communications*, vol. 43, no. 12, pp. 2907–2913, 1995.

- [11] R. A. Goubran, H. M. Hafez, and A. U. H. Sheikh, "Implementation of a real-time mobile channel simulator using a DSP chip," *IEEE Transactions on Instrumentation and Measurement*, vol. 40, no. 4, pp. 709–714, 1991.
- [12] C. Kominakis, "A Fast and Accurate Rayleigh Fading Simulator," in *Proceedings of the IEEE Global Telecommunications Conference (GLOBECOM'03)*, pp. 3306–3310, December 2003.
- [13] A. Alimohammad, S. Fouladi Fard, B. F. Cockburn, and C. Schlegel, "A compact single-FPGA fading-channel simulator," *IEEE Transactions on Circuits and Systems II*, vol. 55, no. 1, pp. 84–88, 2008.
- [14] L. B. Jackson, *Digital Filters and Signal Processing*, Kluwer Academic Publishers, 1989.
- [15] K. E. Baddour and N. C. Beaulieu, "Autoregressive modeling for fading channel simulation," *IEEE Transactions on Wireless Communications*, vol. 4, no. 4, pp. 1650–1662, 2005.
- [16] A. Antoniou, *Digital Filters, Analysis, Design, and Applications*, McGraw-Hill, 1993.
- [17] J. Carletta, R. Veillette, F. Krach, and Z. Fang, "Determining appropriate precisions for signals in fixed-point IIR filters," in *Proceedings of the 40th Design Automation Conference*, pp. 656–661, June 2003.
- [18] "Filter design toolbox for use with Matlab," User's Guide, The Mathworks, 2005.
- [19] M. Pätzold, Y. Li, and F. Laue, "A study of a land mobile satellite channel model with asymmetrical Doppler power spectrum and lognormally distributed line-of-sight component," *IEEE Transactions on Vehicular Technology*, vol. 47, no. 1, pp. 297–310, 1998.
- [20] P. Petrus, J. H. Reed, and T. S. Rappaport, "Effects of directional antennas at the base station on the Doppler spectrum," *IEEE Communications Letters*, vol. 1, no. 2, pp. 40–42, 1997.
- [21] J. Salz and J. H. Winters, "Effect of fading correlation on adaptive arrays in digital mobile radio," *IEEE Transactions on Vehicular Technology*, vol. 43, no. 4, pp. 1049–1057, 1994.
- [22] K. Anim-Appiah, "Complex envelope correlations for non-isotropic scattering," *Electronics Letters*, vol. 34, no. 9, pp. 918–919, 1998.
- [23] Q. Spencer, M. Rice, B. Jeffs, and M. Jensen, "Statistical model for angle of arrival in indoor multipath propagation," in *Proceedings of the 1997 47th IEEE Vehicular Technology Conference*, pp. 1415–1419, Phoenix, Ariz, USA, May 1997.
- [24] M. D. Austin and G. L. Stuber, "Velocity adaptive handoff algorithms for microcellular systems," *IEEE Transactions on Vehicular Technology*, vol. 43, no. 3, pp. 549–561, 1994.
- [25] A. Abdi, J. A. Barger, and M. Kaveh, "A parametric model for the distribution of the angle of arrival and the associated correlation function and power spectrum at the mobile station," *IEEE Transactions on Vehicular Technology*, vol. 51, no. 3, pp. 425–434, 2002.
- [26] C. A. Gutiérrez and M. Pätzold, "The design of sum-of-cisoids Rayleigh fading channel simulators assuming non-isotropic scattering conditions," *IEEE Transactions on Wireless Communications*, vol. 9, no. 4, pp. 1308–1314, 2010.
- [27] C. A. Gutiérrez, M. Pätzold, A. Sandoval, and C. Delgado-Mata, "An ergodic sum-of-cisoids simulator for multiple uncorrelated Rayleigh fading channels under generalized scattering conditions," *IEEE Transactions on Wireless Communications*, vol. 61, no. 5, pp. 2375–2382, 2012.
- [28] K. V. Mardia, *Statistics of Directional Data*, Academic Press, New York, NY, USA, 1972.
- [29] A. V. Oppenheim, R. W. Schaffer, and J. R. Buck, *Discrete Time Signal Processing*, Prentice Hall, 1999.
- [30] V. Erceg, L. Schumacher, P. Kyritsi et al., "TGN channel models," Tech. Rep. IEEE 802.11-03/940r4, Garden Grove, Calif, USA, 2004.
- [31] H. G. Martinez, "Design of recursive digital filters with optimum magnitude and attenuation poles on the unit circle," *IEEE Transactions on Acoustics, Speech, and Signal Processing*, vol. 26, no. 2, pp. 150–156, 1978.
- [32] X. Chen and T. W. Parks, "Design of IIR filters in the complex domain," *IEEE Transactions on Acoustics, Speech, and Signal Processing*, vol. 38, no. 6, pp. 910–920, 1990.
- [33] W. S. Lu, "Design of stable minimax IIR digital filters using semidefinite programming," in *Proceedings of the IEEE International Symposium on Circuits and Systems*, pp. 355–358, Geneva, Switzerland, May 2000.
- [34] L. B. Jackson, "Frequency-domain Steiglitz-McBride method for least-squares IIR filter design, ARMA modeling, and periodogram smoothing," *IEEE Signal Processing Letters*, vol. 15, pp. 49–52, 2008.
- [35] A. G. Deczky, "Synthesis of recursive digital filters using the minimum p-error criterion," *IEEE Transactions on Audio and Electroacoustics*, vol. 20, no. 4, pp. 257–263, 1972.
- [36] A. Tarczyński and G. D. Cain, "New algorithm for designing near-optimal Chebyshev IIR and FIR filters," in *Proceedings of the 38th IEEE Midwest Symposium on Circuits and Systems*, pp. 584–587, Rio de Janeiro, Brazil, August 1995.
- [37] A. Tarczyński, G. D. Cain, E. Hermanowicz, and M. Rojewski, "A WISE method for designing IIR filters," *IEEE Transactions on Signal Processing*, vol. 49, no. 7, pp. 1421–1432, 2001.
- [38] T. W. Fox, "Fixed-point IIR digital filters with simultaneous hardware usage, group delay and magnitude frequency response specifications," in *Proceedings of the Canadian Conference on Electrical and Computer Engineering*, pp. 1704–1707, Saskatoon, Canada, May 2005.
- [39] L. B. Jackson, "A narrowband IIR digital filter with low sensitivity and roundoff noise," *IEEE Signal Processing Letters*, vol. 10, no. 6, pp. 164–167, 2003.
- [40] G. Vanuytsel, P. Boets, L. Van Biesen, and S. Temmerman, "Efficient hybrid optimization of fixed-point cascaded IIR filter coefficients," in *Proceedings of the 19th IEEE Instrumentation and Measurement Technology Conference*, pp. 793–797, May 2002.
- [41] A. Krukowski and I. Kale, "Two approaches for fixed-point filter design: 'bit-flipping' algorithm and constrained downhill simplex method," in *Proceedings of the Signal Processing and Its Applications Symposium*, vol. 2, pp. 965–968, 1999.
- [42] S. Kirkpatrick, C. D. Gelatt, and M. P. Vecchi, "Optimization by simulated annealing," *Science*, vol. 220, no. 4598, pp. 671–680, 1983.
- [43] A. Alimohammad, S. Fouladi Fard, and B. F. Cockburn, "Accurate simulation of nonisotropic fading channels with arbitrary temporal correlation," *IET Communications*, vol. 6, no. 5, pp. 557–564, 2012.
- [44] K. Steiglitz, "Computer-aided design of recursive digital filters," *IEEE Trans Audio Electroacoust*, vol. AU-18, no. 2, pp. 123–129, 1970.
- [45] R. G. Bland, D. Goldfarb, and M. J. Todd, "The ellipsoid method: a survey," *Operations Research*, vol. 29, no. 6, pp. 1039–1091, 1981.

- [46] A. K. Aboagye, "Overflow avoidance techniques in cascaded IIR filter implementations on the TMS320 DSPs," Texas Instruments Application Report, 1999.
- [47] L. B. Jackson, *Digital Filters and Signal Processing: with MATLAB Exercises*, Kluwer Academic Publishers, 1996.

Research Article

Wideband and Ultrawideband Channel Models in Working Machine Environment

Attaphongse Taparugssanagorn, Matti Hämäläinen, and Jari Linatti

Centre for Wireless Communications, University of Oulu, 90570 Oulu, Finland

Correspondence should be addressed to Attaphongse Taparugssanagorn, attaphongset@gmail.com

Received 23 April 2012; Revised 17 July 2012; Accepted 30 July 2012

Academic Editor: Matthias Pätzold

Copyright © 2012 Attaphongse Taparugssanagorn et al. This is an open access article distributed under the Creative Commons Attribution License, which permits unrestricted use, distribution, and reproduction in any medium, provided the original work is properly cited.

We present statistical models for wideband and ultrawideband (UWB) radio channels in a working machine cabin environment. Based on a set of measurements, it was found that such a small and confined space causes mostly diffuse multipath scattering rather than specular paths. The amplitude of the channel impulse responses in the wideband case is mostly Rayleigh distributed small-scale fading signal, with only a few paths exhibiting Ricean distributions, whereas the ones in the UWB case tend to be log-normally distributed. For the path amplitude, we suggest an exponential decay profile, which has a constant slope in dB scale, with the corresponding parameters for the UWB case. For the wideband case, a twofold exponential decay profile provides excellent fits to the measured data. It was also noted that the root-mean-square (RMS) delay spread is independent of the line-of-sight/obstructed line-of-sight situations of the channel. The multipath components contributing significant energy play a major role in such a small environment if compared to the direct path. In addition, the radio channel gains are attenuated with the presence of a driver inside the cabin.

1. Introduction

A wireless sensor network (WSN), which is a wireless network consisting of spatially distributed autonomous devices using sensors to cooperatively monitor physical or environmental conditions [1], today covers very widely in many industrial and civilian application areas, including industrial process monitoring and control, health monitoring, environment and habitat monitoring, home automation, and traffic control. Wireless intra-vehicle communications system has been proposed as a new type of communications system that can provide onboard passengers with bidirectional high-speed data exchange services for both communications and entertainment [2, 3]. For the purpose of safety, comfort and convenience, WSNs are being deployed in the new models of automotives to collect such information as temperature, speed, pressure, and so on. This idea of exploiting WSNs is not limited to applications in a working machine only. The information and communication system used in a working machine makes it easier for driver to control the operation, for example, in a wood processing guiding the trunk cutting according to orders input from the system. This can

guarantee quick processing during logging, and high productivity. This information system is expected to be wirelessly controlled by the driver. Using wireless communication links instead of wired link can save a big amount of installing costs. In addition, measuring vibrations acting on the human body, so-called “human vibration,” is the prevention of health risks and the evaluation of comfort, for example, in vehicles [4]. Wireless vibration sensing application embedded to wireless body area networks (WBANs) can also be included in the future system.

The design of information and communication systems requires a good understanding of the corresponding radio wave propagation channel. The characteristics of an indoor radio propagation is found to be its site-specific behavior. Many existing radio channel measurement campaigns and the corresponding channel models have been restricted to typical residential and office environments, which are highly limited by the attenuation of walls [5, 6]. Only few radio channel measurements were done inside a vehicle [7, 8]. To our knowledge, there is no work done in a working machine environment, which can have the different radio channel characteristics due to its small and confined space.

This paper discusses on experimental radio channel measurements that are carried out in a working machine environment within two different frequency bands, that is, the industrial, scientific, and medical (ISM) radio frequency band (2.4–2.4835 GHz) and the ultrawideband (UWB) frequency band (3.1 and 10 GHz). The statistical radio channel models based on the measurement results are then developed. The novelty of this paper comes from the new environment whose radio channel characteristics are modeled.

Section 2 of the paper is devoted to the description of the measurement setup including the scenarios. Section 3 addresses the characterization of the measured radio channels. The average channel impulse responses for each scenario are analyzed and discussed. The parameters of the statistical channel model are also presented in this section. Section 4 deals with the implementation of the channel model and its evaluation. The conclusions of this work are given in Section 5.

2. Measurement Campaigns

2.1. Measurement Setup. The measurements were carried out in a frequency domain using Agilent 8720ES S-parameter vector network analyzer (VNA) [9]. The network analyzer is operated in a transfer function measurement mode, where port 1 and port 2 are the transmitting and the receiving ports, respectively. Thus, the measurements result as a frequency response of the channel.

The measurements were carried out in the frequency band between 2.4–2.4835 GHz, which is in the ISM band, and is used, that is, by the standards IEEE 802.11 and 802.15.4 dedicated for wireless local area network (WLAN) communication. The measurements in an UWB frequency band between 3.1–10 GHz were also conducted. Therefore, the measured bandwidths B were 83.5 MHz and 6.9 GHz, respectively. Consequently, the corresponding delay resolutions are 11.97 ns and 0.14 ns. The maximum number of frequency points per sweep M is 1601, which can then be used to calculate the maximum detectable delay τ_{\max} of the channel as

$$\tau_{\max} = \frac{(M - 1)}{B}. \quad (1)$$

Using (1), the maximum detectable delay, τ_{\max} of the channels for two different bandwidths are 19.16 μs and 231.88 ns, which correspond to 5.75 km and 69.56 m, respectively, in a free-space distance. Maximum detectable delay is just a measurement system-based parameter. It is introduced to show that the measurement system is able to detect all propagation paths having significant contribution to the received power. However, the usable signal energy is in the shorter delays than the maximum detectable delay as can be seen later on.

The antennas for the measurements in WLAN band 2.4–2.4835 GHz were HGA7S 7 dBi high gain antennas [10]. The SkyCross SMT-3TO10 M-A antennas [11] were used for the measurements in UWB band. Both types of the antennas are linearly polarized. The SkyCross SMT-3TO10 M-A antennas

TABLE 1: Measurement system parameters.

Parameters	Value
Frequency band	ISM (2.4–2.4835 GHz), UWB (3.1–10 GHz)
Bandwidth	83.5 MHz, 6.9 GHz
Number of sample points within the band	1601
Maximum detectable delay	19.16 μs (5.75 km), 231.88 ns (69.56 m)
Sweep time	800 ms
Average noise floor	–108 dBm
Transmit power	5 dBm
Tx and Rx cables loss	7.96 dB

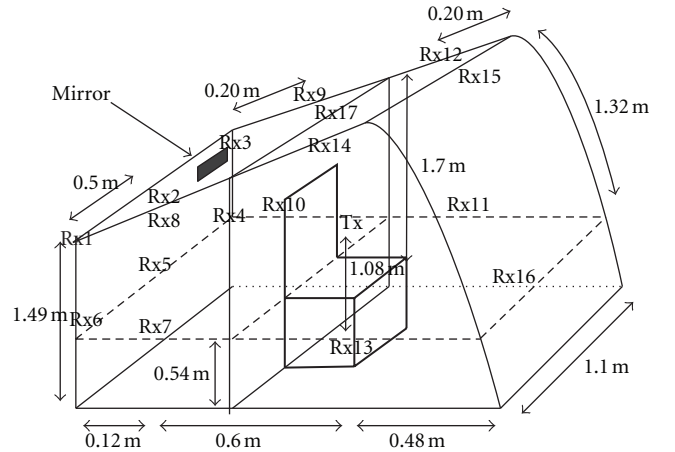


FIGURE 1: Arrangement of the antennas' positions for measurements inside a working machine cabin.

are azimuthally omnidirectional, whereas the HGA7S 7 dBi high gain antennas are designed for 360 degrees of coverage [10]. The sweep time of the VNA depends on the frequency points within the sweep band, being automatically adjusted by the network analyzer, that is, radio channels were measured in a frequency domain over the frequency band of interest. This corresponds to a conventional S_{21} parameter (S_{21} parameter refers to the signal exiting at Port 2 for the signal incident at Port 1 of VNA) measurement setup, where the radio channel is the device under test (DUT). The transmit power used in this study was 5 dBm (equivalent to 3.16 mW) as the VNA output port. Table 1 summarizes the measurement system parameters.

2.2. Channel Measurement Description. The measurements were conducted inside a cabin of a working machine with the dimensions as illustrated in Figure 1. The transmit (Tx) antenna and the receive (Rx) antenna are, in general, set to face each other, and the line-of-sight (LOS) path always exists except when the links are blocked by the seat. The arrangement of the antennas' positions is shown in Figure 1. The position of the Tx antenna is fixed at the

seat on 1.08 m above the cabin floor. The positions of the Rx antenna were moved to 17 different spots, namely, from the position Rx1 till the position Rx17. At each position, 100 consecutive measurements of the channel were taken to improve statistical reliability. This number of typically used in static cases. In order to study radio channels inside a cabin in a working machine for real situations, the following three scenarios are investigated:

- (i) scenario 1: without a driver, when the engine is off.
- (ii) scenario 2: with a driver sitting, when the engine is off.
- (iii) scenario 3: with a driver sitting, when the engine is on.

3. Channel Measurement Results and Data Analysis

Measured S_{21} -parameters, that is, channel transfer functions, are converted to the time domain, that is, to channel impulse responses $h(\tau)$, using an inverse fast Fourier transform (IFFT). A Hamming window is used to reduce sidelobes. The channel impulse response is generally given by a tapped delay line model [12] as

$$h(\tau) = \sum_{l=0}^{L-1} a_l \delta(\tau - \tau_l) \exp(j\phi_l), \quad (2)$$

where a_l is the amplitude of the l th path, τ_l is the arrival time of the l th path, ϕ_l is the phase for the l th path, and L is the number of paths. $\delta(t)$ stands for the Dirac function, which is the impulse symbol and is sometimes called as ‘‘Dirac’s delta function.’’ The phase ϕ_l is modeled by a uniform distribution $U\{0, 2\pi\}$. The statistical parameters defining the channel model are presented in the following paragraphs.

3.1. Average Channel Impulse Response. One hundred individual realizations of the channel impulse response were averaged for each position. The reason for using one hundred realizations is since this is typically used to guarantee statistical reliability. This number of sweeps is recorded for all the individual links measured, so the total number of sweeps carried out during the measurement campaign is much higher. When using frequency domain measurement technique, the environment needs to be static, which means that one hundred consecutive measurements per link is enough.

To proceed further analysis, all measured channel impulse responses are first truncated above the noise threshold, set to the noise level adding 10 dB (about -98 dBm). The only paths above the noise threshold are taken into account. Some examples are presented here in order to explain the analysis. The large-scale features (i.e., path loss) and also small-scale features (due to the change in pulse shape) of the channels are taken into account. The large-scale models are necessary for network planning and link budget design while small-scale models are necessary for efficient receiver design and performance analysis. This kind of models is not

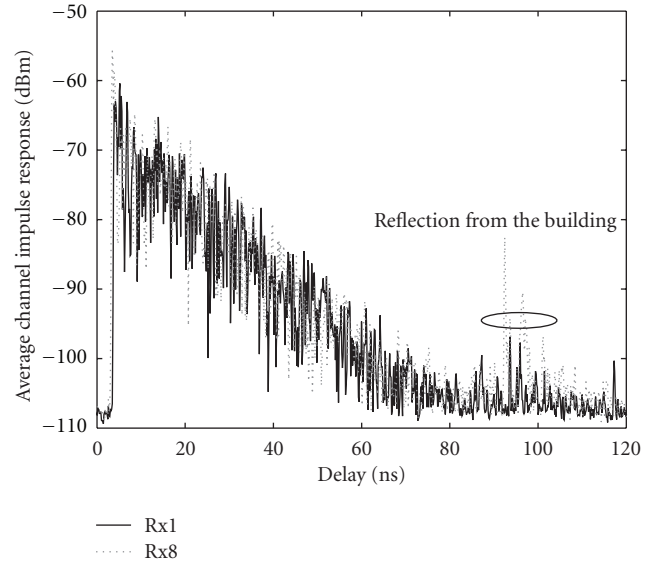


FIGURE 2: Average channel impulse responses for the UWB band in scenario 1: without a driver, when the engine is off. The positions of Rx antenna are Rx1 and Rx8.

publicly available at open literature for working machine’s cabin environment so far.

As preliminarily shown in [13], the measured channel impulse responses for the ISM band have two constant slopes in dB scale, which correspond to a typical exponential decay profile in a linear scale. This shows that there are many reflections rather than a significant specular path. This is excellently suited to characterize diffuse scattering [14].

The average channel impulse responses for the UWB band (6.9 GHz bandwidth) in scenario 1, without a driver, when the engine is off shown in Figure 2 were also represented in [13]. The UWB measurements allow us to check the presence of many paths arriving at the receiver within the delay resolution and the maximum delay. Firstly, the channel impulse responses have a constant slope in dB, which corresponds to a typical exponential decay profile in a linear scale. The other advantage of the UWB measurements is the high temporal resolution, which makes it possible to see the first path more precisely. The first path arrival time can approximately translate into the distance between Tx and Rx antennas. Therefore, the distances between Tx and Rx1, Rx3, Rx8 as well as Rx17 are 1.17 m, 1.35 m, 1.05 m, and 0.81 m, respectively (3.9 ns, 4.5 ns, 3.5 ns, and 2.7 ns, resp.). The Rx1 and Rx3 are in the obstructed line-of-sight (OLOS) case; thus the first path is not the strongest path. Depending on the position, the constructive multipaths can create a stronger path to the receiver. The Rx8 and Rx17 are LOS cases; therefore, the first path is also the strongest path. Figure 3 illustrates the average measured channel impulse responses for the ISM band, Rx5 (OLOS), in three different scenarios. When the driver is inside the cabin, the radio waves in all multipaths from the Tx close to the body of the driver (≈ 3 cm) are attenuated. In addition, the first path arrival time is longer than the one in the case of no driver inside the cabin.

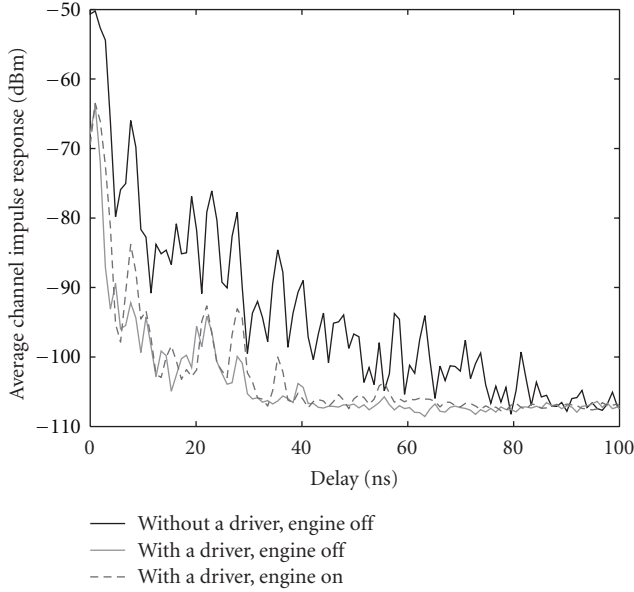


FIGURE 3: Average measured channel impulse responses for the ISM band, Rx5 (OLOS), in three different scenarios.

Note that in the following, the analysis has been carried out against several distributions, and the best fits have been selected. Moreover, all the parameters used in the models were extracted from the measured data during the postprocessing. From the extracted parameters, we develop measurements-based deterministic channel models for both ISM band and UWB band cases.

3.1.1. Exponential Decaying Factor (a_l). As explained above, the path amplitude a_l in (2) is approximately modeled by an exponential decay profile with a Ricean factor γ_0 and an exponential decaying factor Γ for UWB case as

$$10 \log_{10} |a_l| = \begin{cases} 0, & l = 0 \\ \gamma_0 + 10 \log_{10} \left(\exp\left(\frac{-t_l}{\Gamma}\right) \right), & 1 \leq l \leq L-1. \end{cases} \quad (3)$$

For ISM case, the channel impulse responses have two constant slopes in dB, and thus the path amplitude a_l in (2) is approximately modeled by twofold exponential decay profile with two Ricean factors γ_{01} and γ_{02} as well as two exponential decaying factors Γ_1 and Γ_2 as

$$10 \log_{10} |a_l| = \begin{cases} 0, & l = 0 \\ \gamma_{01} + 10 \log_{10} \left(\exp\left(\frac{-t_l}{\Gamma_1}\right) \right), & 1 \leq l \leq l_1 \\ \gamma_{02} + 10 \log_{10} \left(\exp\left(\frac{-t_l}{\Gamma_2}\right) \right), & l_1 + 1 \leq l \leq L-1, \end{cases} \quad (4)$$

where l_1 is the last path of the first part.

An example from each frequency band is presented in Figure 4 showing the average channel impulse response for the ISM band and for Rx17 (LOS) in the first scenario

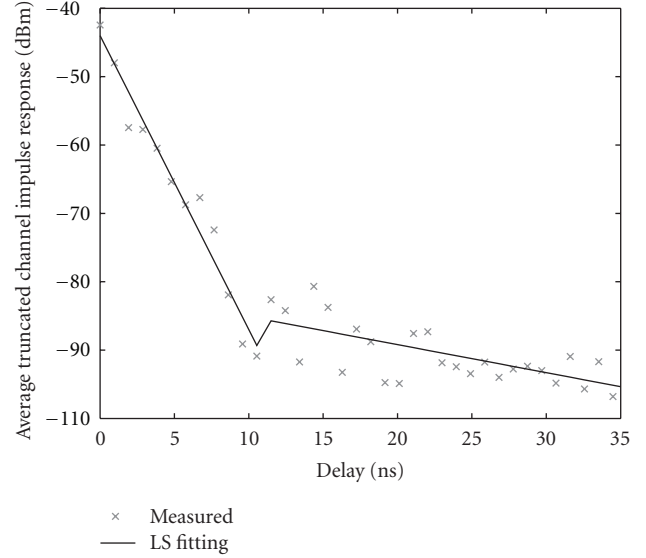


FIGURE 4: Average channel impulse responses for the ISM band for Rx17 (LOS) and the least square linear fitting curve in dB scale.

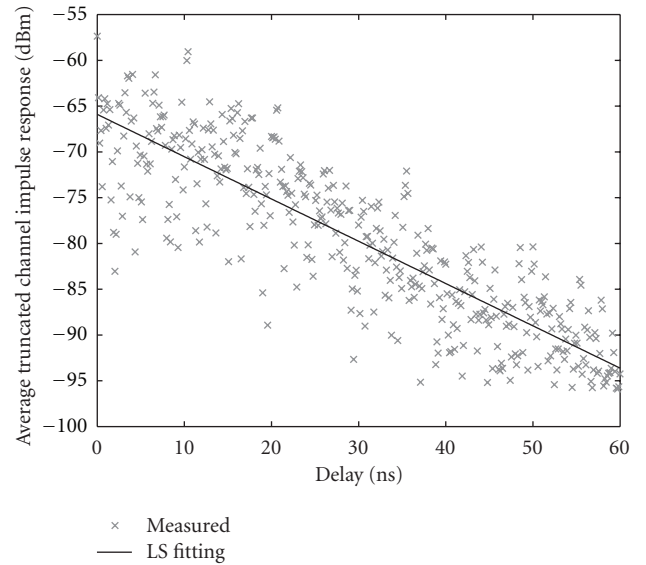


FIGURE 5: Average channel impulse responses for the UWB band for Rx17 (LOS) and the least square linear fitting curve in dB scale.

(without a driver, the engine is off) and the twofold least square (LS) linear fitting curve in dB scale. The corresponding factors γ_{01} and γ_{02} are -44 dB and -81 dB, respectively, as well as the exponential decaying factor Γ_1 and Γ_2 are 2.33 and 24.39, respectively. Figure 5 shows the average channel impulse response for the UWB band and for Rx17 (LOS) and the LS linear fitting in dB. The corresponding factor γ_0 and the exponential decaying factor Γ are -66 dB and 21.74.

3.1.2. Amplitude Variation (χ). This part represents the amplitude variation χ over the mean value of the path amplitude. The cumulative distribution functions (CDFs) in Figures 6 and 7 depict that the amplitude variations of the

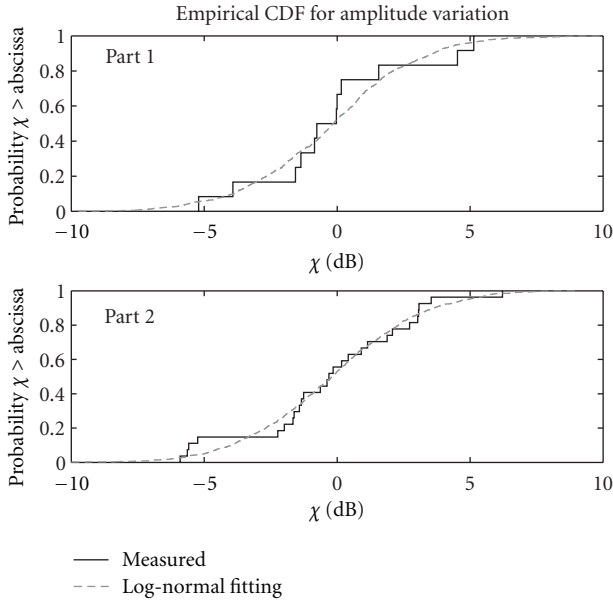


FIGURE 6: CDFs of the amplitude variation over the mean value of the path amplitude and the log-normal fitting curve for the ISM band and for Rx17 (LOS).

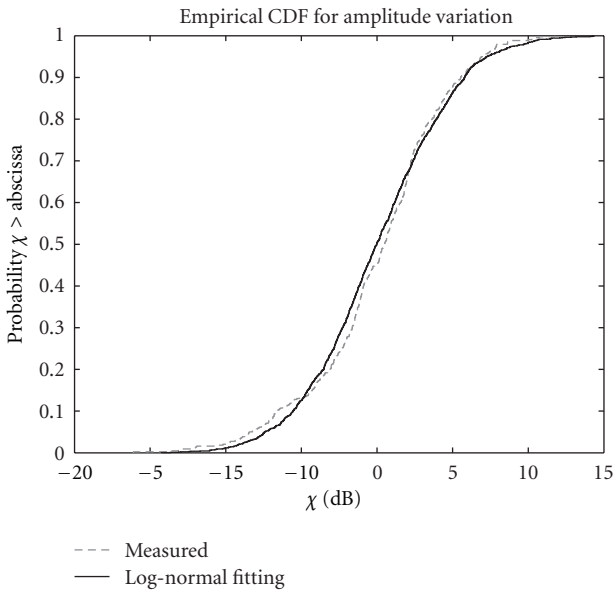


FIGURE 7: CDFs of the amplitude variation over the mean value of the path amplitude and the log-normal fitting curve for the UWB band and for Rx17 (LOS).

average channel impulse responses are well fitted by the log-normal distribution with zero mean and standard deviation σ_χ of 6.69 dB and 4.50 dB, respectively.

3.1.3. Number of Paths (L). The CDFs of the number of paths L (above the noise threshold) are excellently fitted by Poisson distribution with a certain mean μ_L . An example for Rx14 (LOS) in the UWB band shown in Figure 8, respectively. The number of paths decreases with the presence of the driver. In the case of the ISM band, the CDFs of the number of

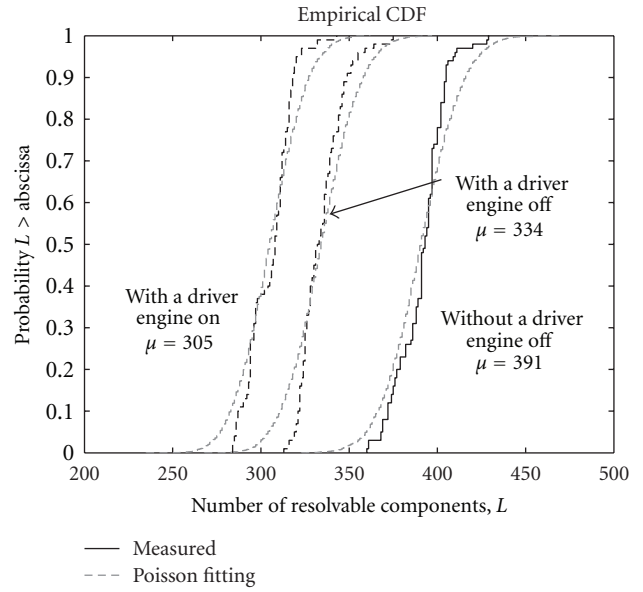


FIGURE 8: CDFs of the number of paths L for Rx14 (LOS) in the UWB band measurements.

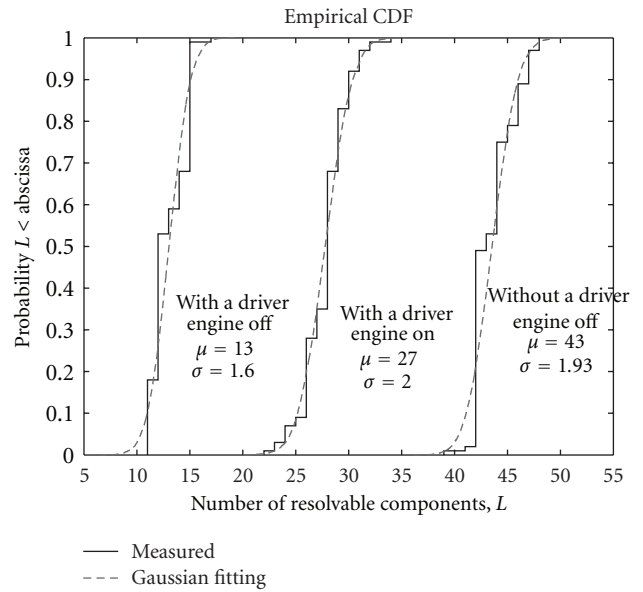


FIGURE 9: CDFs of the number of paths L for Rx14 (LOS) in the ISM band measurements.

paths L are fitted by Gaussian distribution with certain mean μ_L and standard deviation σ_L as an example in Figure 9 for Rx14 (LOS). The number of paths presented in the paper is for channel modeling purpose. Nonetheless, they are much more than the typical number of paths in system design, for example, the number of paths within 10 dB of the strongest path and the number of paths containing 85 percent of the energy, which give approximately 35–50 paths in the UWB band case. As can be seen, the impact of the vibration (of the engine) on the number of the paths is clear, especially, in the case of OLOS unlike the other channel characteristics.

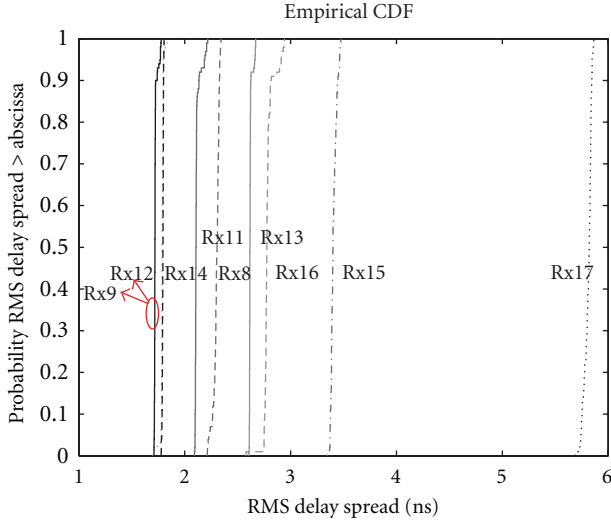


FIGURE 10: CDFs of the measured RMS delay spreads for LOS in the UWB band measurements.

3.2. Small-Scale Channel Characterization

3.2.1. Delay Dispersion. In order to compare different multipath channels and to develop general design guidelines, parameters which grossly quantify the multipath channel are used. The mean excess delay τ_m and root-mean-square (RMS) delay spread τ_{RMS} are commonly used to imply the time delay dispersive properties of a wideband multipath channel parameters that can be determined from a power delay profile. The received signal will suffer spreading in time if compared to the transmitted signal. This dispersion can also imply frequency selective fading and intersymbol interference (ISI). No serious ISI is likely to occur if the symbol duration is longer than, say, ten times the RMS delay spread [14]. The RMS delay spread is the standard deviation (or root-mean-square) value of the delay of reflections, weighted proportional to the energy in the reflected waves defined as [14]

$$\tau_{\text{RMS}} = \sqrt{\frac{\sum_{i=1}^L (\tau_i - \tau_m)^2 \cdot |h(\tau_i)|^2}{\sum_{i=1}^L |h(\tau_i)|^2}}, \quad (5)$$

where τ_m is expressed as

$$\tau_m = \sqrt{\frac{\sum_{i=1}^L \tau_i \cdot |h(\tau_i)|^2}{\sum_{i=1}^L |h(\tau_i)|^2}}. \quad (6)$$

Figures 10 and 11 depict the CDFs of the measured RMS delay spreads for LOS and OLOS situations, respectively, for the UWB band measurements. All values are in the range of 1.7–5.8 ns, which are very small if compared to typical indoor RMS delay spread varying between 14 and 18 ns [14]. We can see that the RMS delay spread is independent of the LOS/OLOS situations of the channel. Neither of the distance, this is because the cabin space is very small. The multipath components contributing significant energy play a major role in such a small environment if compared to the direct path. This is very important on the selection of the antenna position and also to the receiver structure.

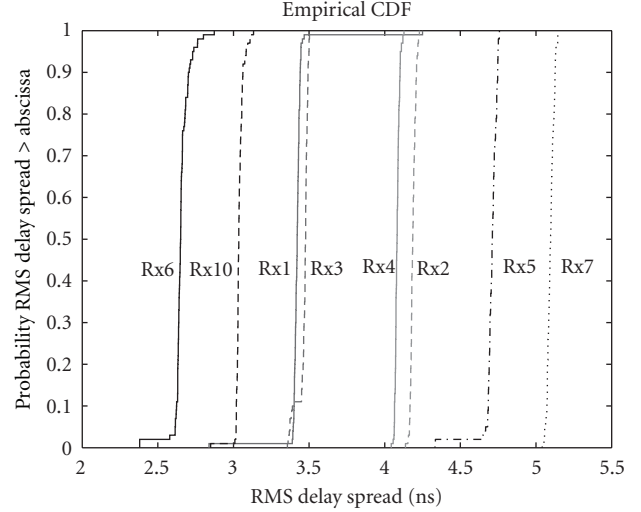


FIGURE 11: CDF of the measured RMS delay spreads for OLOS in the UWB band measurements.

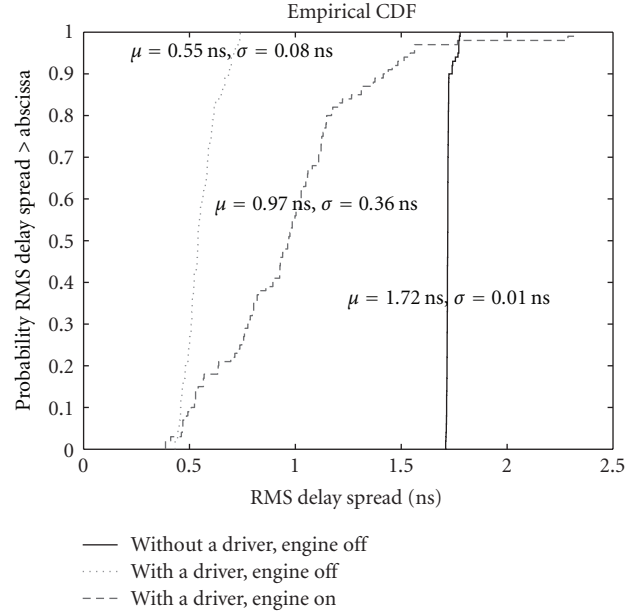


FIGURE 12: CDFs of the measured RMS delay spreads for Rx12 (LOS) in the UWB band measurements in all three scenarios.

An example for the case of the cabin with a driver, when the Rx antenna is at Rx12 (LOS), is shown in Figure 12. The RMS delay spread decreases by approximately 1.2 ns, since the presence of people in the cabin attenuates the path gains. Corresponding CDFs for OLOS case (Rx4) are shown in Figure 13. The standard deviations σ of the RMS delay spreads, when the engine is on (cabin vibration), are larger than the ones, when the engine is off. This shows that the radio channels differ considerably for the case with and without driver.

3.2.2. Amplitude Distribution. In the ISM band, the power received for each delay tap is the vectorial sum of many multipath components arriving in the corresponding delay

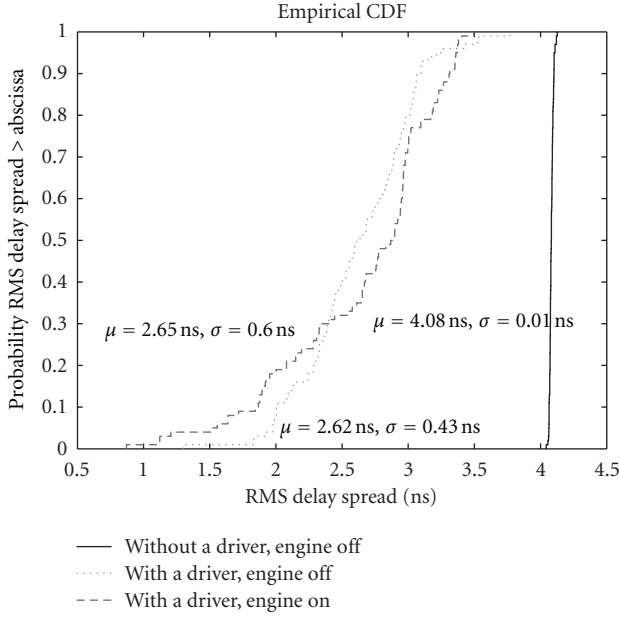


FIGURE 13: CDFs of the measured RMS delay spreads for Rx4 (OLOS) in the UWB band measurements in all three scenarios.

bin. The central limit theorem is therefore valid, and the amplitudes of the delay bins exhibit a Rayleigh (in nonLOS or OLOS case) or a Ricean (in LOS case) distribution [15]. On the contrary, only few multipath components (MPCs) fall into each resolvable delay in the UWB band. Therefore, the central limit theorem is not applicable and the amplitudes of the delay bins consequently do not exhibit a Rayleigh or Rice distributions.

In the ISM band case, in all scenarios, the first delay bins tend to be Ricean distribution due to their high K factors [16], whereas the other delay bins can be assumed to be Rayleigh distributed due to their very small K factors.

For LOS case in the UWB band, as explained above, only few MPCs fall into each resolvable delay and the central limit theorem is therefore not applicable. The measured amplitudes are rather log-normally distributed [17].

3.3. Large-Scale Channel Characterization. Path loss (PL) is an important large-scale characteristic for link budget calculation and system design. In the conventional narrowband channel, Friis transmission formula is used to model the received signal power, P_r in free space given by [18]

$$P_r(d) = \frac{P_t G_t G_r \lambda^2}{(4\pi d)^2}, \quad (7)$$

where P_t is the transmitted power, and G_t and G_r are the Tx and the Rx antenna gains, respectively. λ is the wavelength, and d is the Tx-Rx separation distance. The Friis transmission formula shows that the received signal power falls off as the square of the Tx-Rx separation distance. From (7), the term PL is given by $(\lambda/4\pi d)^2$ which predicts that signal power will decrease with the square of increasing frequency and distance. These show the presence of both distance and frequency dependency in path loss.

TABLE 2: Average path loss (PL) within the measured band.

Measurement scenarios and cases	Mean path loss (dB)
UWB band	
Scenario 1, LOS	73.31 dB
Scenario 1, OLOS	77.32 dB
Scenario 2, LOS	75.86 dB
Scenario 2, OLOS	79.90 dB
Scenario 3, LOS	76.20 dB
Scenario 3, OLOS	80.16 dB
ISM band	
Scenario 1, LOS	66.74 dB
Scenario 1, OLOS	71.85 dB
Scenario 2, LOS	80.20 dB
Scenario 2, OLOS	90.24 dB
Scenario 3, LOS	80.82 dB
Scenario 3, OLOS	90.92 dB

Nevertheless, the frequency is constant within a bandwidth of interest and is thus negligible. However, for UWB systems, the frequency dependency in PL can be significant due to the large bandwidth (>500 MHz). The channel would distort the signal spectrum of the signal which is directly related to the signal distortions, that is, pulse shape distortion. PL can be obtained directly from the measured channel transfer function $H(f)$. The distance dependency of the path loss is calculated by time snapshot and frequency averaging over the total bandwidth at each Rx position as

$$PL(d) = \frac{1}{MN} \sum_{i=1}^N \sum_{j=1}^M |H(f_i, t_j; d)|^2, \quad (8)$$

where $H(f_i, t_j; d)$ denotes the j th channel transfer function time snapshot at frequency f_i in a distance d . N and M denote the number of sample points within the band and the number of snapshots, respectively.

The mean PLs for both LOS and OLOS cases are calculated from (8) and averaged over the results from all Rx positions in each case. The results for each case and each scenario are summarized in Table 2. As expected, the PL increases in the OLOS case and with the presence of a driver. Moreover, it is noted that the PL in the case when the engine is on is not very different than in the case when the engine is off. This follows the initial assumption.

4. Channel Modeling and Evaluation

In this section, we describe an experimental based deterministic channel model which are developed for both ISM band and UWB band cases. As shown in Figures 14 and 15 in Section 3.2.2, the amplitude of the first five delay bin in the ISM band case for the LOS case tends to be Ricean distributed. The remaining delay bins can be assumed to be Rayleigh distributed due to their small K -factors. For the OLOS case, only the first delay bin tends to be Ricean distributed, whereas the rest can be assumed to be Rayleigh distributed. In the UWB case, the amplitudes of all delay

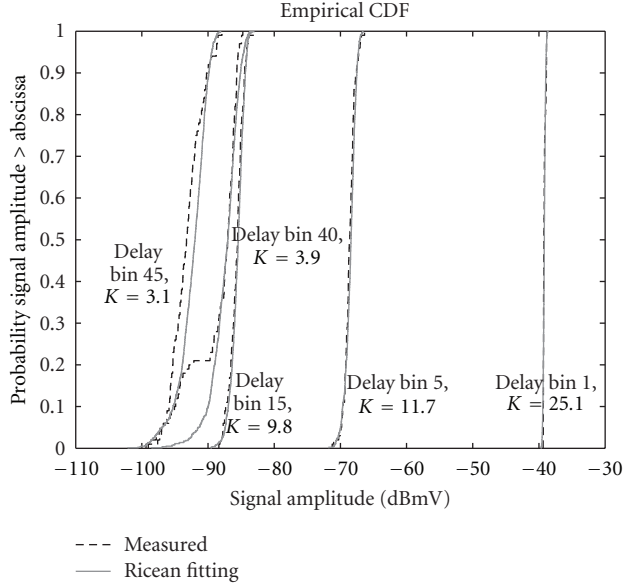


FIGURE 14: CDFs of the amplitudes of five delay bins, 1, 5, 15, 40 and 45 with corresponding K factors for LOS case at Rx12.

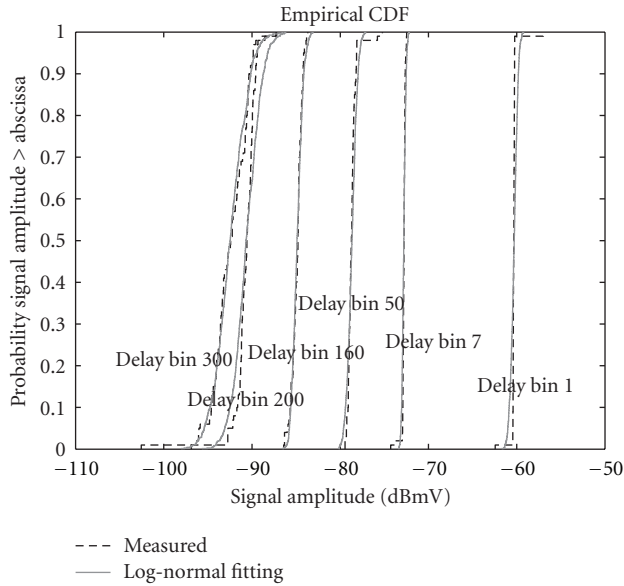


FIGURE 15: CDFs of the amplitudes of four delay bins, 1, 5, 15, and 40 with log-normal fitting for OLOS case at Rx1, without a driver and the engine off.

bins tend to be log normally distributed. To achieve that a random vector \mathbf{x} , where each component is the value of each delay bin with the corresponding distribution, either Ricean or Rayleigh or log normal up to the cases, with zero (dB) mean is generated. Subsequently, the amplitude vector of the channel $|\mathbf{h}|$ is obtained by scaling the random vector with an exponential decay profile with the corresponding Ricean factor γ_0 and exponential decaying factor Γ described in Section 3.1.1. Finally, the phase vector of the channel Φ is assumed to be uniformly distributed $U\{0, 2\pi\}$.

As an example, the channels for the case of Rx17 (LOS) in the ISM band and the case of Rx17 (LOS) in the UWB

TABLE 3: Channel parameters for simulation for the case of Rx 17 (LOS).

Parameters	ISM band	UWB band
μ_L (paths)	53	441
γ_{01} (dB)	-44	—
γ_{02} (dB)	-81	—
γ_0 (dB)	—	-66
Γ_1	2.33	—
Γ_2	24.39	—
Γ	—	21.74
Amplitude distribution	Ricean with K -factor = 21.35, 16.70, 16.28, 14.40, and 13.89 dB for the delay bin 1–5, Rayleigh for the remaining delay bins	log normal for all delay bins
σ_χ (dB)	2.97 and 3.04	4.50

band (Figures 4 and 5) are simulated. For the former case, it is done by using (3) and the simulation parameters presented in Table 3. For the latter case, (4) is used with the simulation parameters in Table 3.

The average channel impulse response and the RMS delay spread τ_{RMS} are used for validating the simulated model as depicted in Figures 16 and 17. As we can see, the simulated channels have a good agreement with the measured channels.

5. Conclusions

In order to deploy wireless information and communication systems in such a confined environment like in a cabin of a working machine, a good understanding of the radio propagation channels, and a simple corresponding channel model are required. To our knowledge, there is no work done in a working machine environment, which have different radio channel characteristics due to its small and confined space. The measurement campaigns inside the working machine cabin were taken for two different frequency ranges, that is, in 2.4–2.4835 GHz ISM band used, for example, by the standards IEEE 802.11 and 802.15.4 dedicated for wireless local area network communication, as well as, in an ultra wideband frequency band 3.1–10 GHz. Three different scenarios for each frequency band, that is, (1) without a driver, the engine is off, (2) with a driver, the engine is off, and (3) with a driver, the engine is on, were carried out.

The characteristics of the propagation channels were quite different from a traditional indoor environment; namely, there are many reflections rather than a significant specular path. This is excellently suited to characterize diffuse scattering. The UWB measurements have the high temporal resolution advantage, which consequently makes us able to see the first path accurately. This is translated into the distance between Tx and Rx antennas. With the presence of the driver inside the cabin, the radio channel gains are attenuated. In addition, the first path arrival time comes later than the one in the case of no driver inside the cabin. There was no significant difference found between the cases when

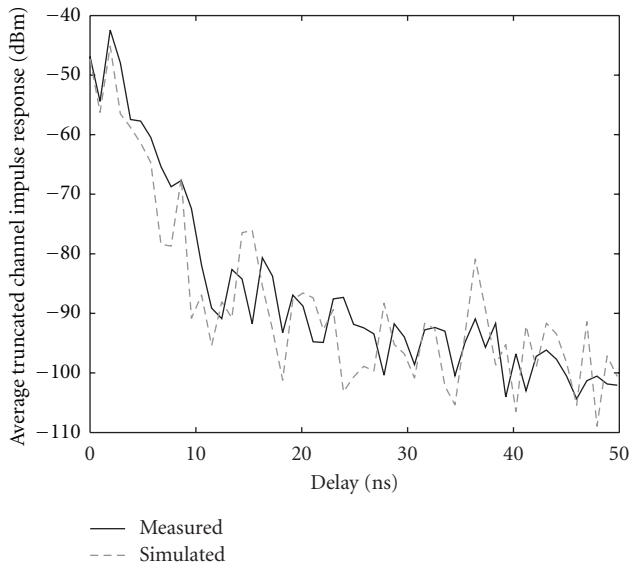


FIGURE 16: Average measured and simulated channel impulse responses for Rx17 (LOS) in the ISM band.

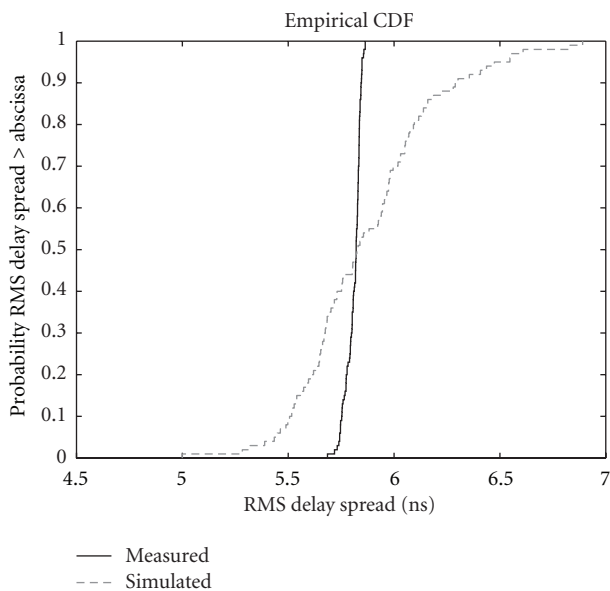


FIGURE 17: CDF of the RMS delay spreads of the measured and simulated channels for Rx17 (LOS) in the UWB band.

the engine is on and off, only the number of the paths are different, especially, in the case of OLOS; that is, the vibration (of the engine) has only the impact on the number of paths, whereas the impact on other channel properties is trivial.

In both frequency ranges, the exponential decay profile was modeled for the path with the corresponding parameters. For the amplitude distribution, many MPCs arrive in the corresponding delay bin in the ISM band, the central limit theorem is therefore valid, and the amplitudes of the delay bins exhibit a Rayleigh (in non-LOS or OLOS case) or Ricean (in LOS case) distributions. On the contrary, only few MPCs fall into each resolvable delay in the UWB band. Therefore, the central limit theorem is not applicable and

the amplitudes of the delay bins consequently do not exhibit a Rayleigh or Ricean distribution, but rather log-normal distribution. For the delay dispersion, the RMS delay spread was independent of the LOS/OLOS situations of the channel. Neither of the distance, this is because the cabin space is very small. The MPCs contributing significant energy play a major role in such a small environment if compared to the direct path. This is very important on the selection of the antenna position and the receiver design. For the path loss, the frequency dependency of the path loss in the UWB band was firstly observed. Secondly, the mean path loss increases in the OLOS case and with the presence of the driver. Moreover, it was noted that the mean path loss in the case, when the engine is on, is not very different than in the case, when the engine is off. The measurements obtained were used to estimate the corresponding channel parameters in order to build statistical simulated channel models.

The developed radio channel models give a great additional information to wireless communications designs in a working machine cabin environment.

Acknowledgment

The authors would like to thank Mr. Ari Isola for his contribution during the measurements. This work was funded by the Finnish Funding Agency for Technology and Innovation through the European Regional Development Fund.

References

- [1] K. Römer and F. Mattern, "The design space of wireless sensor networks," *IEEE Wireless Communications*, vol. 11, no. 6, pp. 54–61, 2004.
- [2] T. Elbatt, C. Saraydar, M. Ames, and T. Talty, "Potential for intra-vehicle wireless automotive sensor networks," in *2006 IEEE Sarnoff Symposium*, usa, March 2006.
- [3] G. Leen and D. Heffernan, "Vehicles without wires," *Computing and Control Engineering Journal*, vol. 12, no. 5, pp. 205–211, 2001.
- [4] AN21E Application Note Human Vibration Measurement EC Directive 2002/44/EC.
- [5] D. Cassioli, M. Z. Win, and A. F. Molisch, "The ultra-wide bandwidth indoor channel: from statistical model to simulations," *IEEE Journal on Selected Areas in Communications*, vol. 20, no. 6, pp. 1247–1257, 2002.
- [6] S. S. Ghassemzadeh, R. Jana, C. W. Rice, W. Turin, and V. Tarokh, "Measurement and modeling of an ultra-wide bandwidth indoor channel," *IEEE Transactions on Communications*, vol. 52, no. 10, pp. 1786–1796, 2004.
- [7] W. Niu, J. Li, and T. Talty, "Intra-Vehicle UWB channel measurements and statistical analysis," in *2008 IEEE Global Telecommunications Conference, GLOBECOM 2008*, pp. 3402–3406, usa, December 2008.
- [8] W. Xiang, "A vehicular ultra-wideband channel model for future wireless intra-vehicle communications (IVC) Systems," in *2007 IEEE 66th Vehicular Technology Conference, VTC 2007-Fall*, pp. 2159–2163, usa, October 2007.
- [9] <http://www.alliancetesteq.com/>.
- [10] <http://tinyurl.com/cyszob/>.
- [11] <http://skycross.com/Products/PDFs/SMT-3TO10M-A.pdf>.

- [12] I. Oppermann, M. Hämäläinen, and J. Iinatti, *UWB Theory and Applications*, John Wiley & Sons, New York, NY, USA, 2004.
- [13] A. Taparugssanagorn, M. Hämäläinen, and J. Iinatti, “UWB and wideband channel models for working machine environment,” in *Proceedings of the 73rd IEEE Vehicular Technology Conference Spring (VTC’12-Spring)*, Budapest, Hungary, 2011.
- [14] A. Richter, *Estimation of radio channel parameters: models and algorithms [Ph.D. thesis]*, Technische Universität Ilmenau, Ilmenau, Germany, 2005.
- [15] A. Muqaibel, A. Safaai-Jazi, A. Attiya, B. Woerner, and S. Riad, “Path-loss and time dispersion parameters for indoor UWB propagation,” *IEEE Transactions on Wireless Communications*, vol. 5, no. 2, pp. 550–558, 2006.
- [16] M. Abramowitz and I. A. Stegun, *Handbook of Mathematical Functions, National Bureau of Standards, 1964*, Dover Publications, New York, NY, USA, 1965.
- [17] C. Tepedelenlioğlu, A. Abdi, and G. B. Giannakis, “The Ricean K factor: estimation and performance analysis,” *IEEE Transactions on Wireless Communications*, vol. 2, no. 4, pp. 799–810, 2003.
- [18] E. Limpert, W. A. Stahel, and M. Abbt, “Log-normal distributions across the sciences: keys and clues,” *BioScience*, vol. 51, no. 5, pp. 341–352, 2001.